Investigation of the early time period of ultrafast magnetization dynamics

Xuan Liu

Sorbonne Université

Ecole doctorale

L'ECOLE DOCTORALE DE CHIMIE PHYSIQUE ET DE

CHIMIE ANALYTIQUE DE PARIS CENTRE (ED 388)

Investigation of the early time period of ultrafast magnetization dynamics

Par [LIU XUAN]

Thèse de doctorat de [Physique]

Dirigée par [Jan Luning]

Présentée et soutenue publiquement le [10/10/2018]

Devant un jury composé de :

M. Massimiliano Marangolo	Professeur	Sorbonne Université	(Président du jury)
M. Christian Gutt	Professeur	University of Siegen	(Rapporteur)
Mme. Christine Boeglin	Directrice de recherche	Université de Strasbourg	(Rapportrice)
M. Fausto Sirotti	Directeur de recherche	Ecole Polytechnique	(Examinateur)
M. Jan Lüning	Professeur	Sorbonne Université	(Directeur de thèse)

Acknowledgements

First of all, I would like to express my sincere gratitude to my advisor Prof. Jan Lüning supporting me during these past three years, for his patience, motivation, and immense knowledge. His guidance helped me in all the time of research and writing of this thesis. I could not have imagined having a better advisor and mentor for my Ph.D. study.

Besides, I would like to thank Dr. Boris Vodungbo, for their insightful comments and encouragement, but also for the hard question which incented me to widen my research from various perspectives. This work would not have been possible without his guidance. Under his guidance I successfully overcame many difficulties and learned a lot. He also reviewed my thesis progress, gave his valuable suggestions and the most importantly made corrections of my entire thesis.

This thesis has been written during my stay at the lab (LCPMR) of the University of Sorbonne. I would like to thank the lab (LCPMR) for providing excellent working and experimental conditions. Especially, it offered me financial support to participate three summer schools and several international conferences.

My sincere thanks also go to the Chinese Scholarship Council (CSC), for offering me an opportunity and for providing me three-year financial support.

I also would like to thank people who work at FLASH (DESY). They deserve my sincere expression of thanks for providing me experimental hands-on-training on different aspects of how to build experimental setup in a real beamline step by step. During the measurement they also provide us many technique supports to finish complex experiment.

Last but not the least; I would like to thank all my friends and colleagues in our lab: Aladine, Mehdi, Jiatai, Meiyi, Mostafa, Hang, Junwen, Carla, Roman, Emmanuelle, Renaud, Jiapin, Zailan, and Zhesheng, etc. During these three years, we shared our happiness, stress, and good memory. Although we are from different countries and speak different languages, we spent our happiest moment together in our life.

Special thanks are due to my wife, Dai Wenyu, for supporting me spiritually throughout writing this thesis and my life in general. I also thank for heart-warming kindness from my brother Wentao in China

Most importantly, I would like to thank my parents and my family; they support me all the way until finishing my Ph.D. I would like to say it is not easy for them these years; they always encourage me and love me. It is hard to express my best love to them in language.

Paris, August, 2018

Liu Xuan

Contents

I dedicate this thesis to

my parents, my wife, and all my family for their constant support and unconditional love.

Introduction and overview

In 1996, Beaurepaire *et al*. [1] published a very remarkable observation: a nickel thin film exposed to an intense 60 femtoseconds (fs) pulse from an IR laser demagnetizes in less than one picosecond. This ultrafast decrease is followed by a slower partial recovery. This observation was very surprising at that time and opened up and entirely new research field: "femtomagnetism". Moreover, this world-wide attention was also a consequence of the potential for applications of this phenomenon in the field of magnetic information storage and manipulation. Despite many experimental results, which have been obtained over the past 20 years, the physics of ultrafast optical manipulation of magnetism is still poorly understood. This is partly due to the fact that the excitation pushes the magnetic material into an extremely non-equilibrium state, where the description of magnetic phenomena in terms of thermodynamics is no longer valid. Over the past two decades, scientists have developed several models to describe and to explain the ultrafast demagnetization phenomenon. Of these, the most broadly discussed ones are based on Elliott-Yafet like spins-flip scattering [2] and super-diffusive spin-transport [3]. However, neither one of the two has convinced the entire community. Current experiments suggest that potentially both of them occur simultaneously.

The goal of my research is to investigate the early time period of the ultrafast demagnetization in various ferromagnetic materials (Co, Ni, and Fe…) by using different experimental methods, to obtain novel insight on the underlying physical mechanisms.

More precisely, the particular questions that motivated me were:

1. In Fe and Ni ferromagnetic alloys, both elements are strongly coupled by exchange interaction. Does this coupling influence the time of demagnetization after pumping with a femtosecond laser?
2. Could the super-diffusive spin-transport be observable to explain the weak spin transport between the layers and the similar demagnetization curve in Co and Pt system?
3. The last question is around the different pump wavelength will truly affect the demagnetization behavior. In this thesis, several different results are clearly presented to try to find the answer of the questions above.

My work focuses on developing novel experimental methods to study magnetization dynamics in thin films. In the first year, I developed the capabilities to fabricate magnetic thin film samples by magnetron sputter deposition and to characterize their magnetic properties using the MOKE (Magneto-optic Kerr effect) setup in our laboratory. I then participated in a

serious of experiments, which we realized at different X-ray free electron laser facilities. The experimental results, which I obtained as part of my doctoral thesis project, are from these four beam-times:

- Split and Delay experiment - realized at FLASH2 @ DESY (Germany)
- Terahertz pump experiment - realized at FLASH1 @ DESY (Germany)
- Co and Pt spin transport experiment @ DESY (Germany)

In the terahertz pump experiment we expected to realize an ultrafast coherent magnetization control by a coupling between the B-field of the terahertz pump and the thin film's magnetization. The goal was then to study the transition from such a coherent coupling to the non-coherently excited ultrafast demagnetization phenomenon by increasing gradually the terahertz pump frequency. Unfortunately, the B-field that could be obtained at the THz source of FLASH1 was too weak to manipulate significantly the film's magnetization. We could, however, detect at least the non-coherent excitation of the demagnetization process by the shorter wavelength components of the THz pulse.

Another task is the role of the transport of hot electrons between multilayers in ultrafast demagnetization, which can be realized on Co and Pt spin transport experiment. Despite many experimental evidences point out that there exists spin current transport in this process, it cannot completely explain the experimental observation in the Co/Pt multilayer. In this experiment, we probe with Co $M_{2,3}$ edge and Pt N_7 absorption edge to investigate the ultrafast demagnetization process of these two elements, while a good design of samples allows us to detect the spin current transport from Co layer to Pt layer.

Finally, the idea of the split-and-delay experiment is to exploit the recently developed short pulse mode of FLASH. Splitting such an incident X-ray pulse in two and using them as pump and probe pulse, the time resolution of the experiment is uniquely determined by the X-ray pulse length. This will enable us to study with sub 5 fs time resolution the onset of the magnetization dynamics to resolve fine details, which has not been possible so far. Our first goal is to understand whether there is a delay between the onsets of the demagnetization dynamics in transition metal compounds like Ni-Fe. And to compare the dynamic of these elements with that found in the pure materials. The underlying question is whether the strong ferromagnetic exchange interaction between Fe and Ni in these alloys will influence their respective demagnetization time. The analysis of the preliminary data obtained in our commissioning experiment is ongoing, but the first results are encouraging.

In this thesis, First, I would like to introduce the strong motivation of this work and a basic knowledge of magnetism in Chapter 1, I will give an overview over the theoretical

background of my work related to ultrafast demagnetization in Chapter 2, and Chapter 3. In Chapter 4, I will discuss the experiment of split and delay at FLASH2, which is the main work of my thesis. Then chapter 5 shows the experiment result obtained at FLASH1 by using XUV probe and THz pump. While, in chapter 6 I will present the experiment result on Co and Pt system at FLASH1. At last, in Chapter 7 I will give a conclusion for all the chapters.

1 Chapter 1: Introduction of Magnetism

1.1 History of Magnetism

Magnetism has been puzzling the human for more than thousands of years. It is one of the fundamental phenomena in the universe. It has fascinated and inspired the civilization of this world. The first recordings of using the power of magnetism as a compass for navigations were northern song dynasty (960 CE – 1126 CE). Nowadays, the application of magnetism appears in different corners of modern life: memory storage, communication technology, aerospace and many aspects. Theory of magnetism in the solid-state physics is developed, and following a dramatically fast development either on the application and theory. Nowadays Magnetism in materials became no longer a "plaything for philosophers," but of enormous and growing importance for the application. For instance: the giant magnetoresistance effect (GMR) discovered by Fert and Gräfenberg independently in 1988 [4][5], and finally this great contribution won the Nobel Prize in physics in 2007. Thanks to the development of quantum physics, it is found that magnetic moments of electrons in atoms mainly come from two contributions: their intrinsic spin and their orbital motion. Although nucleons of atoms also possess certain detectable magnetic moments, they become negligibly small in comparison. The spin and orbital components of each electron are quantized. The total angular momentum of the atom, **J**, is the vector addition of the angular moment of spin **S** and the angular moment of orbital **L**. For the angular moment of spin **S**, the projection on the Z axe is found is always a physical constant with $\pm\hbar$, even if one applies an external magnetic field, the spin angular momentum will not be affected. Here, **L** and **S** are conserved. The empirical Hund's rules can describe distribution of each state of electrons in one atom with fixed quantum number of L and S. Due to this collective effect from electrons of some magnetic metals or alloys, it reveals macroscopic magnetic behavior in bulk materials.

However, there are many research directions on magnetism. In this chapter I concentrate on the behavior and peculiarities of magnetism in the solid-state physics: mainly about ferromagnetic and paramagnetic materials and of corresponding microscopic theory.

1.2 Paramagnetism and Ferromagnetism

Generally speaking, paramagnetic materials have a small, positive susceptibility to magnetic fields. A magnetic field can slightly magnetize them, and the magnetic properties will disappear when the external field is removed (see figure 1.1 (a) and (b)). Physically speaking, paramagnetism is due to the presence of some unpaired electrons, and from the realignment of the electron paths caused by the external magnetic field [6].

However, compared to paramagnetic materials, ferromagnetic materials exhibit a large, positive susceptibility to an external magnetic field. When removing the external magnetic field, it keeps their magnetic properties (see figure 1.1 (c) and (d)). The physical picture of ferromagnetic materials is that some unpaired electrons on their atoms form a net magnetic moment. There is a long-distance coupling between their magnetic moments. Then it generates many regions with the same magnetic orientation, which is known as magnetic domains. Due to the presence of magnetic domains, the ferromagnetic materials can reveal strong magnetic properties [6] [7]. More details are presented in the following part.

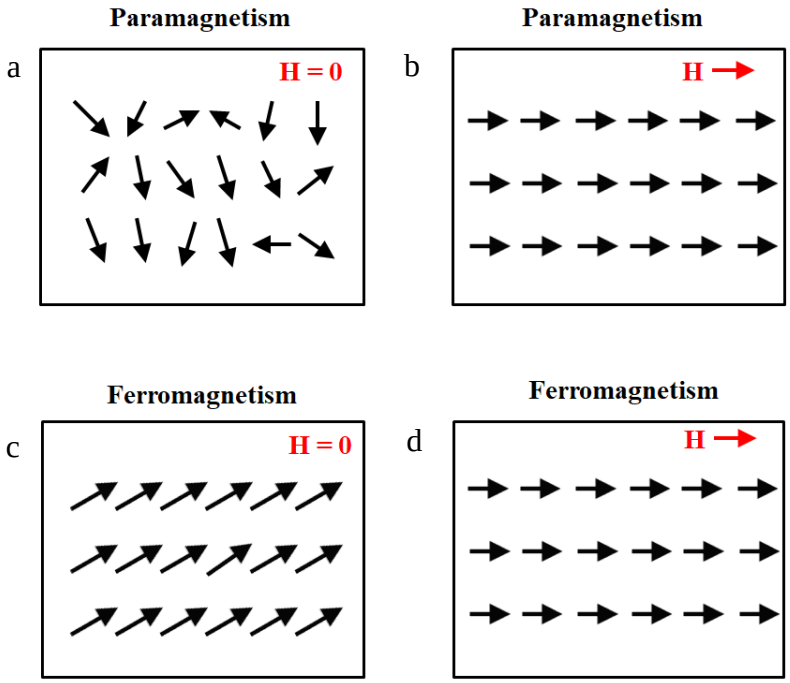

Figure 1.1: Paramagnetism and ferromagnetism. Atomic dipole configuration (black arrows) for a paramagnetic material (a) and (b); for a ferromagnetic material (c) and (d). The red arrows present the external magnetic field.

1.2.1 Langevin paramagnetism

Paramagnetism was at first investigated in 1845 by Michael Faraday [5][9]. Paramagnetic materials can obtain weak magnetic field after being touched by a strong magnet. The type is the Langevin paramagnetism which can be supported by the famous Curie's law. It demonstrates a very simple linear relationship between susceptibility (χ) and temperature (T).

$$\chi = \frac{C}{T} = \frac{M}{H} \tag{1}$$

The origin of Langevin paramagnetism can be explained by using a statistic physics model: all the atoms have their own magnetic moment. If we ignore the interaction between atoms and apply an external field B, we can calculate the free energy of this system. In the statistical physics, for N repetitive atoms the total free energy F becomes[10] [11] [12] :

$$F = -Nk_BTln(Z) \tag{2}$$

where Z is the partition function, which describes the statistical properties of a system in thermodynamic equilibrium:

$$\mathrm{Z} = \sum_{m_J=-J}^{m_J=J} e^{-m_J g\,\mu_B B / k_B T} \tag{3}$$

$$m_J = 0, \pm 1, \pm 2, \pm 3, \pm 4 \ldots \tag{3}$$

The magnetization of total system can be written [10] [11] [12]:

$$M = -\frac{\partial F}{\partial B} = Nk_BT\frac{\partial}{\partial B}\ln(Z) \tag{4}$$

$$\mathrm{M} = \mathrm{Ng}\,\mu_B J.\, B_J(\alpha) \tag{5}$$

$$\alpha = \frac{g\mu_B JB}{k_BT} \tag{6}$$

$$B_J(\alpha) = \frac{2J+1}{2J}\coth\left(\frac{2J+1}{2J}\alpha\right) - \frac{1}{2J}\coth\left(\frac{1}{2J}\alpha\right) \tag{7}$$

where N is the number of atoms per unit volume, g is the g-factor, μ_B is the Bohr magneton, k_B is the Boltzmann constant, and m_J is the projection of the magnetic moment in the Z axis. Now we can discuss the change by the temperature and the external field:

1. When α ~ ∞, and $B_J(\alpha) \sim 1$, thus the magnetization reaches to saturation M = Ng $\mu_B J$
2. When α ~ 0, and $B_J(\alpha) \sim \frac{J+1}{3J}\alpha$, thus $M = \frac{N\mu_B{}^2 g^2 J(J+1)B}{3k_B T}$

From the point 2, we can deduce the curie's law:

$$\chi = \frac{C}{T} = \frac{M}{H} \tag{8}$$

$$C = \frac{N\mu_B{}^2 g^2 J(J+1)}{3k_B} \tag{9}$$

Curie's law is very successful under the limited condition of low magnetization ($\mu BH \lesssim k_B T$), but does not apply in the high-field and low-temperature. The reason for this is due to the approximation of low α in the Brillouin function. [10]

1.2.2 Pauli paramagnetism

For some alkali metals and noble metals, there is other effect that has to be taken in to account: Pauli paramagnetism. Here, conduction electrons can be considered as Fermi gas, the weakly interaction can be replaced by giving an effective mass for electrons near the Fermi level. For these materials, one contribution to the magnetic response comes from the interaction with the electron spins and the magnetic field known as Pauli paramagnetism. As the description of the figure 1.2, at the low temperature, with the applied magnetic field, the unbalance of electrons generates the magnetic field from inside. This process is called Pauli paramagnetism which mainly comes from the electrons near the Fermi level that split into two the spin-up and spin-down bands.

Spin up and spin down electrons will shift after applying a magnetic field **H** along z axis:

$$\Delta = \mu_B H \tag{10}$$

$$\varepsilon_\uparrow = \varepsilon + \Delta, \varepsilon_\downarrow = \varepsilon - \Delta \tag{11}$$

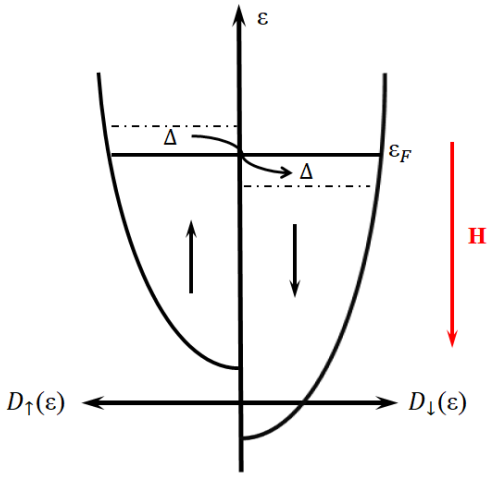

Figure 1.2: The electronic bands structure of Pauli paramagnetism, with an applied external magnetic field **H** (red arrow), the distribution of spin up and down electrons under the Fermi level.

Ideally, at zero temperature, the field-induced magnetization of the band electrons is

$$M = \mu_B(n_\uparrow - n_\downarrow) \cong \mu_B(D_\uparrow(\varepsilon_F)\Delta + D_\downarrow(\varepsilon_F)\Delta) \cong \mu_B{}^2 D(\varepsilon_F)H \qquad (12)$$

The following discussions are quite tentative as on theory of the magnetization from Pauli paramagnetism dependent of diffusive electrons. [7][13][14]

1.2.3 Ferromagnetism

Compare to paramagnetic materials, in which spins tend to align parallel to an external magnetic field, all spins of the ferromagnetic materials align parallel to one another. Ferromagnetism can be found in some metals, such as transition metals: Fe, Co, Ni and rare earth metals: Gd, Tb, Dy, Ho, Er, and Tm. There are also some alloys, which reflect ferromagnetic behavior, like FeNi, CoPd, and CoPt. All these materials exhibit a strong permanent magnetization up to a specific temperature after which they lose their magnetization. There was no explanation for ferromagnetism before 20th century: the Bohr–van Leeuwen theorem [15] shows that magnetism cannot occur in purely classical solids. With the development of quantum mechanics, the property of ferromagnetism is concluded in two quantum effects: a. the spin of an electron b. the exchange interaction [16]. Pierre-Ernest

Weiss [17] developed the Molecular or Mean field theory, which is also called Weiss-mean-field theory that leads to the discovery of the Curie-Weiss Law. The most evident magnetic property of ferromagnetic can be described by hysteresis loop, from the hysteresis loop, Curie-Weiss firstly proposed a phenomenological theory that it should exist a certain interaction inside the ferromagnetic materials, because of this interaction, there still exist magnetic field rested when the external field is zero. (See the hysteresis loop). However, at that time, Weiss could not explain this kind of inner interaction; and he called it as Molecular field. From the experimental observation, he found that:

$$\chi = \frac{C}{T-\theta} = \frac{M}{H} \tag{13}$$

Compared to Curie's law, there is another term θ, which is due to explain the inner interaction effect. After several steps calculation, we can obtain a relationship similar with curie's law:

$$\frac{C}{T} = \frac{M}{H + \frac{\theta}{C} \cdot M} = \frac{M}{H_{eff}} \tag{14}$$

H_{eff} is an effective field and it can be composed into two parts, one is from external field H, and the other is so called 'molecular field'. The physical origin this molecular field should use the theory from Heisenberg, which is the task of the paragraph of 1.2.5. Exchange Interaction.

The thermal effect, however, the outside environment will break this spontaneous magnetic ordering. The destroyed magnetic moments can even show random state when the temperature reach up to a certain degree, which is defined as the Curie's temperature of the material. The relation between magnetization of the magnetic materials and temperature is presented in the figure 1.3: magnetization of a Ni film goes down by increasing the temperature, until the Curie's temperature, its magnetization becomes zero. After above the Curie's temperature, the transition from ferromagnetism to paramagnetism will be occurred.

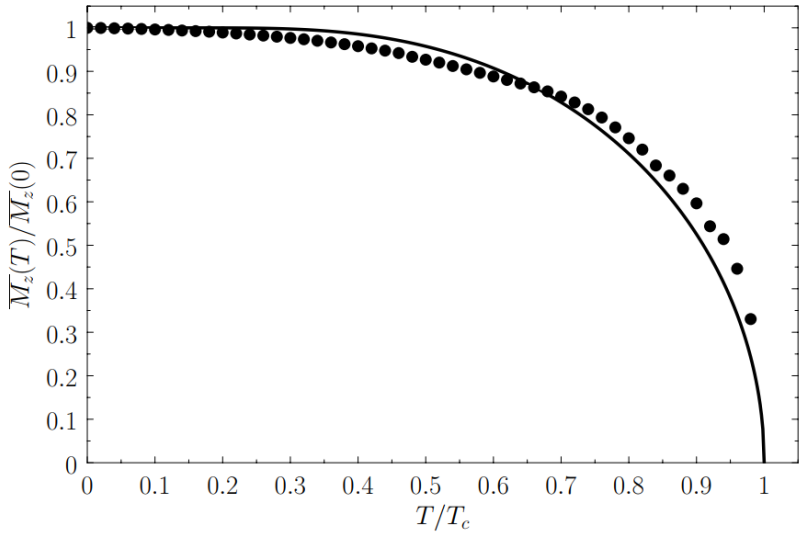

Figure 1.3: Magnetization vs. temperature. Spontaneous magnetization from a Ni film as a function of the temperature without external magnetic field. The black points are from experimental data for nickel and the solid line is theoretical calculation [18].

1.2.4 Magnetic domains

Ferromagnetic materials get their magnetic properties not only because their atoms carry a magnetic moment but also because the material is made up of small regions known as magnetic domains [19]. In the year of 1906, Pierre-Ernest Weiss [20] postulated a hypothetical model that in ferromagnetic materials there are several regions in which the magnetic moments point in the same direction: so called magnetic domain, and the region at the interface of two domains is called domain wall. Ideally, inside a defect-free, homogeneous, ferromagnetic single-crystal, the domain structure can be explained by an equilibrium state between energy of exchange, magneto-elastic, and anisotropy [21]. In a ferromagnetic crystal, although the direction of alignment varies from domain to domain in a more or less random behavior, it usually has an easy axis and hard axis, which is an intrinsic property of the material. Each crystal grain has an easy direction of magnetization and is broken up into domains which are spontaneously magnetized (usually) parallel to this direction.

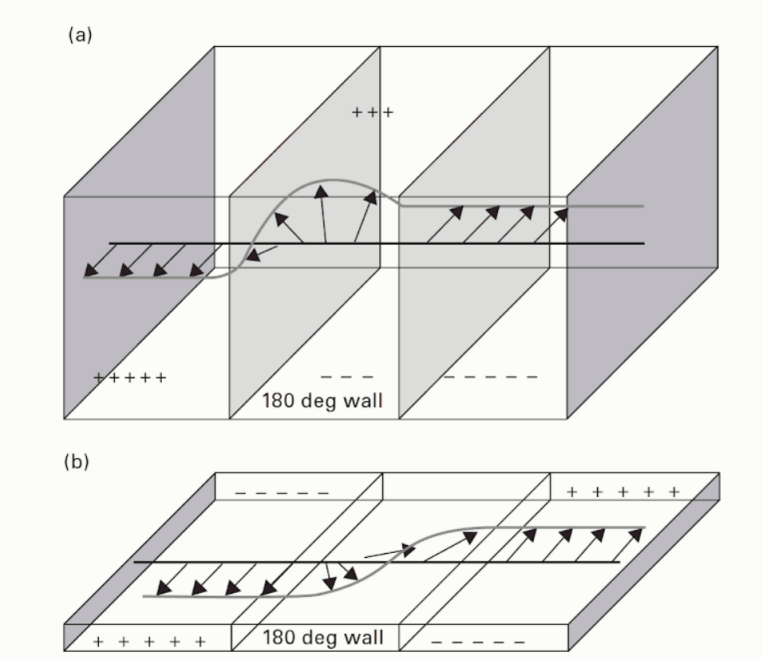

Figure 1.4: The properties of the domain walls. (a) Bloch wall in a thick film (b) Néel walls in a thin film. [22]

Domain Wall Structure can be divided into two types: Neél wall and Bloch wall. (See figure 1.4) In most bulk materials, we find the Bloch wall: the magnetization vector turns bit by bit like a screw out of the plane containing the magnetization to one side of the Bloch wall. In thin layers, however, Néel walls will dominate. In the Néel wall, the magnetization smoothly rotates from the direction of magnetization within the first domain to the direction of magnetization within the second. [22] Bloch walls would produce the demagnetizing field, also called the stray field, while Neél walls can contain the magnetic flux in the material.

1.2.5 Spin Hamiltonians and Exchange Interaction

W. Heisenberg [16] proposed the model of exchange interaction in 1928, which is the first model based on the quantum mechanics to explain the origin of the ferromagnetism. This indeed is an alternative way of formulating Pauli's exclusion principle, since it implies the probability to find two electrons with parallel spins in the same state to vanish.

At the beginning, exchange interaction only refers to the direct exchange. Without the requirement by an intermediary, the electrons on neighboring magnetic atoms interact directly with each other. In the ferromagnetic materials, they usually possess a special electronic

configuration where unoccupied state exist like iron, one Fe atom contains 6 electrons on 3d orbital and 2 electrons on 4s orbital. From the experimental measurement, the result shows the g-factor of Fe is close to two [23]. This demonstrates that the magnetic moment mainly comes from spin angular moment and the contribution from orbital moment is less significant. Thus, there should be interaction between each electron that forces all spins to have same orientation. Heisenberg then proposed a single model that predicts the existence of exchange interaction. A spin Hamiltonian can be written:

$$H = -\sum_{i\ j} J_{ij}\ S_i S_j \tag{15}$$

where J_{ij} is the exchange integral between i-th and j-th spins, when $J_{ij} > 0$, interaction leads to the parallel alignment of the spins. Ideally, in the ferromagnetic system, the exchange integral should be always positive [24] [25].

In metals, the exchange interaction between magnetic ions can be mediated by the conduction electrons. A localized magnetic moment spin-polarizes the conduction electrons and this polarization in turn couples to a neighboring localized magnetic moment that is away from the first magnetic moment. There is no direct coupling between magnetic moments and this is called Ruderman-Kittel-Kasuya-Yosida (RKKY) interaction [26]. RKKY theory has been successful to predict ferromagnetic/antiferromagnetic oscillation in Giant Magneto-resistance GMR [27].

1.2.6 Spin-Orbit Interaction

Electrons in the atom generally possess a spin magnetic moment and an orbital magnetic moment. These two contributions should be coupled for electrons, which can split the electronic states. In quantum physics, the essence of the spin-orbit coupling effect is that the motion of the electron in the electric field causes itself to be in the magnetic field generated by its own motion, and the two possible spin states will occupy two possible energy levels in this magnetic field.

The total angular momentum **J**= **L**+**S,** and in general, the equation 16 for the energy splitting E_{SO} due to spin-orbit interaction was first derived in 1926 by Llewellyn Thomas [28][29], using Bohr's model of the hydrogen atom, Schrödinger's quantum mechanics, and relativistic kinematics. The detail of formula derivation will not be discussed here.

$$E_{SO} \propto \boldsymbol{S}\cdot\boldsymbol{L} \tag{16}$$

1.3 What is the classical demagnetization?

Before we are going to discuss the ultrafast demagnetization, it is important to explain and discuss the classical demagnetization phenomena. The process to demagnetize a ferromagnet is basically a matter of randomizing the orientation of the magnetic dipole. Removal of a magnetic field from a ferromagnet may be accomplished in several ways: heating or hammering. Both thermal effect (heating) and applying pressure will generate the physical disruption and vibration that breaks the order out of the material, leading to a total demagnetization.

The change of magnetization can be described by the transfer of angular momentum of the electrons of the materials. Now if we consider the time scale of demagnetization, the situation becomes more interesting. If we consider a system without changing the external magnetic field, the demagnetization phenomena of ferromagnetic materials mainly come from the variance of temperature, as we discussed before. The boundary of the classical demagnetization to ultrafast demagnetization, however, concentrates on two main points: 1. the different timescale of the angular momentum transfer and 2. Different electron thermalization processes. Figure 1.5 demonstrates the timescale of response for different process of dynamics. For the classical demagnetization process, it usually accompanies the motion of macroscopic domain wall in nanoseconds range. While for the investigation of ultrafast demagnetization, it contains three processes: precession and relaxation, spin-orbit interaction and exchange interaction, which fall into picosecond and femtosecond range respectively.

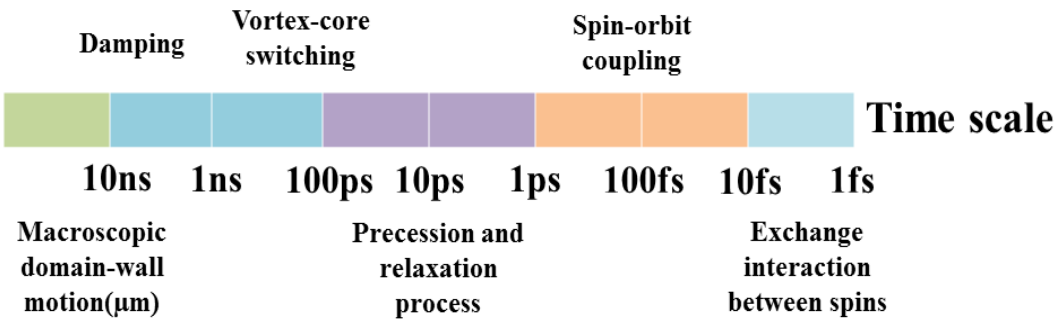

Figure 1.5: Time scales in magnetism dynamics from 1 fs to 10 ns. Exchange interaction falls into less than 10 fs and following by Spin-orbit coupling, precession and relaxation process is in picoseconds range. Then vortex-core switching, damping, and domain-wall motion usually are in nanoseconds range [30].

Compare to the classical demagnetization, thermalization process of ultrafast demagnetization is more complex because of the induced pump laser causing a non-equilibrium state and following by numerous excited electrons. Further discuss will be undertaken in the next paragraph.

2 Chapter 2: Ultrafast Demagnetization Dynamics

2.1 The Phenomenological Description and Challenge of Ultrafast Demagnetization

2.1.1 First discovery of Ultrafast Demagnetization

In 1996, Beaurepaire *et al*. published a very remarkable observation [1]: a Ni film exposed to an intense 60 fs pulse from an optical laser becomes demagnetized in less than a picosecond. Using the magneto-optical Kerr effect as probe, an ultrafast decrease is observed in the magnetization, followed by a slower recovery (see figure 2.1). This observation, together with later measurements using other methods of detection, raised the fundamental question, yet unanswered, of where the spin angular momentum of the electrons goes and how it can be transferred so quickly.

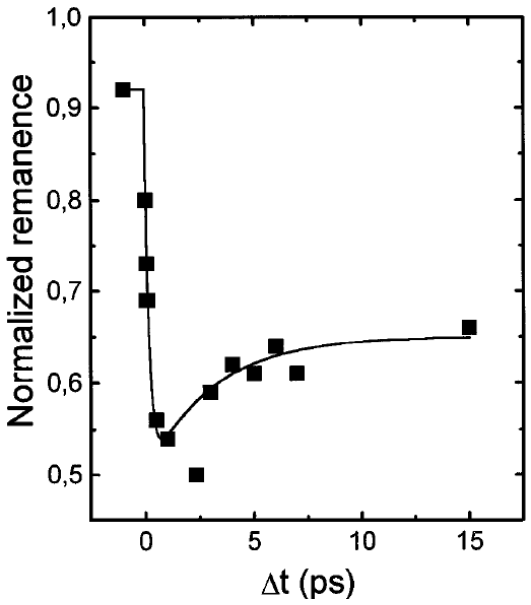

Figure 2.1: Ultrafast demagnetization of a Ni thin film. Sub-picosecond magneto-optical signal reductions after fs optical pump, the normalized remanence is proportional to the magnetization, from this figure, a sudden drop of magneto-optical change fall into less than 1 picosecond [1].

Indeed, there is equivalence between magnetism and angular momentum. As attended by the Einstein de Haas effect [31], then, according to the conservation of total angular momentum, demagnetization is only possible if there is a reservoir of angular momentum available. From all the data accumulated the past 20 years, there is a general consensus that demagnetization occurs within 100-300 fs. The reservoir of angular momentum must be absorbed from magnetization on the same time scale.

2.1.2 Phenomenological Description based on the Landau-Lifshitz Equation

Although obtaining a complete microscopic description of ultrafast magnetization dynamics is the goal of the femtomagnetism research field, phenomenological modeling of these ultrafast processes would be a very insightful first step. One way to do that is to derive an equation of motion for the magnetization in solid which is valid at very high temperature and on very short timescale.

Let's start with a uniformly magnetized solid with a total magnetization M; and the atomic volume is V, then it is easy to obtain the m = M/V which is the magnetic moment for one atom. Then we can describe the precessional motion with damping parameter γ, which is the gyromagnetic ratio and in an external magnetic field H.

$$\frac{\partial \vec{M}}{\partial t} = \gamma \vec{M} \times \vec{H} \tag{17}$$

$$\gamma = \frac{g\mu_B}{\hbar} \tag{18}$$

where g is Landé g-factor, ħ is the reduced Planck constant and μ_B is the Bohr magneton.

Here, the change in angular momentum with time is presented. Nevertheless, the equation 17 only considers the action of the external magnetic field. If one considers the actual situation, this expression is oversimplified, for the electron spins are also influenced by the magneto crystalline anisotropy, magnetostatic coupling and magnetic dipole interaction, etc. Although it is impossible to precisely calculate all these interactions, an approximation can be obtained by using an effective magnetic field H_{eff} [30]. Therefore, the motion of the magnetization vector can be described as the equation below, named after Landau and Lifshitz [32] in the year of 1935.

$$\frac{\partial \vec{M}}{\partial t} = \gamma \vec{M} \times \vec{H}_{eff} \tag{19}$$

In 1955, Gilbert [33] then improved this equation by adding a second term with a damping constant α. The Landau-Lifshitz-Gilbert (LLG) equation is written as following:

$$\frac{\partial \vec{M}}{\partial t} = \gamma \vec{M} \times H_{eff} + \frac{\alpha}{\left|\vec{M}\right|}\left(\vec{M} \times \frac{\partial \vec{M}}{\partial t}\right) \tag{20}$$

However, the validity of the LLG equation is limited to the low temperatures and it also ignores longitudinal relaxation, both of this points being necessary to described laser induced ultrafast magnetization dynamics [34]. The Landau-Lifshitz Bloch (LLB) approach takes into account was proposed by Bloch in try to overcome this limitation [35] .

$$\frac{\partial \vec{M}}{\partial t} = \gamma \vec{M} \times H_{eff} - \gamma \lambda_{\parallel} \frac{\left(\vec{M} H_{eff}\right)\vec{M}}{\left|\vec{M}\right|^2} + \gamma \lambda_{\perp} \frac{\vec{M} \times \left(\vec{M} \times H_{eff}\right)}{\left|\vec{M}\right|^2} \tag{21}$$

In the LLB equation, the longitudinal and transversal damping parameters $\lambda_{\parallel}$ and $\lambda_{\perp}$ are added into the equation. The LLB has been successfully applied by U. Atxitia *et al* [36] to model laser-induced ultrafast magnetization dynamics in Ni, Co and Gd [34][36]. Koopmans *et al* [37] is formally equivalent to the quantum LLB approach.

2.1.3 From Two temperature model to Three temperature model

Since the observation by Beaurepaire *et al*. [1] that a femtosecond laser pulse can quench the magnetization in the 3d-ferromagnets on sub-picosecond timescales. Scientists try to interpret the ultrafast demagnetization as “thermal” processes; the term of temperature is used to describe the transfer the energy flux from electrons to lattice. The thermal exchange from these two reservoirs can be written also in the following form [38]:

$$\mathrm{C_e}(T_e)\frac{dT_e}{dt} = -G_{el}(T_e - T_l) + P(t) \tag{22}$$

$$\mathrm{C_l}(T_l)\frac{dT_l}{dt} = -G_{el}(T_l - T_e) \tag{23}$$

The above equations are called Two-temperature Model that define the hot electron cooling process, in which G_{el} presents the electron-phonon interaction coefficient, and the term P(t) is the energy absorbed by the sample due to the laser field [38]. However, since the lattice is thermalized in few picoseconds that it is too slow to explain the observation in

ultrafast demagnetization. Hence it is necessary to add the spin bath its own temperature. This is the motivation of developing the three temperature model.

2.1.4 Three temperature model

The model for magnetization dynamics has been invoked to help to explain the sub-picosecond demagnetization. This model (see figure 2.2) assumes that the electron (el), the electron spins (sp) and the lattice phonons (lat) represent three mutually-interacting thermal reservoirs. The internal equilibration of the reservoirs occurs at the plasma frequency (el), the spin-wave frequency (sp) and the phonon scattering rate (lat). Furthermore, the reservoirs interact with one another via the electron-phonon interaction (el-lat), the spin lattice relaxation rate (sp-lat) and the spin-orbit interaction (el-sp).

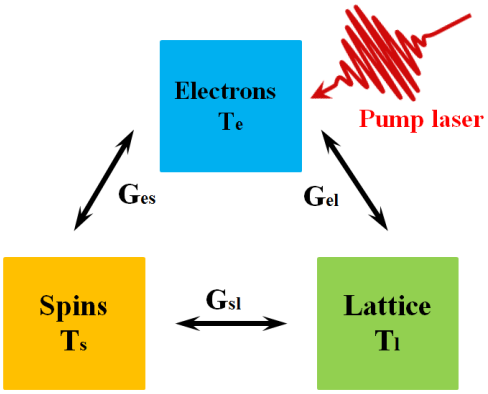

Figure 2.2: A schematic description of three temperature model. Three squares represent electron, spin, and lattice system. Black arrows mean the transfer from each system.

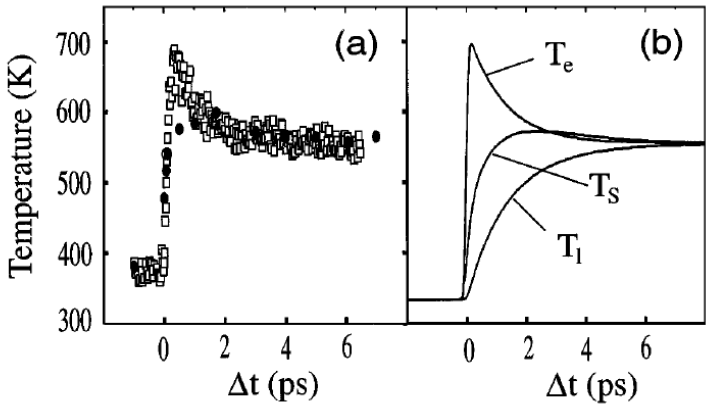

Figure 2.3: Experimental observation of spin (T_s), lattice (T_l), and electron (T_e) temperatures [1].

Figure 2.3 describes the experimental result according to three temperature model. Electron temperature goes up firstly, then following by spin temperature and lattice temperature. The coupling constants are defined as G_{es}, G_{sp} and G_{ep} reflecting the flow rate of exchanging energy between the participating three sub-systems. Therefore, the dynamics of systems is phenomenologically described by three coupled differential equations. (See equation 24-26)

$$C_e(T_e)\frac{dT_e}{dt} = -G_{el}(T_e - T_l) - G_{es}(T_e - T_s) + P(t) \tag{24}$$

$$C_s(T_s)\frac{dT_s}{dt} = -G_{es}(T_s - T_e) - G_{sl}(T_s - T_l) \tag{25}$$

$$C_l(T_l)\frac{dT_l}{dt} = -G_{el}(T_l - T_e) - G_{sl}(T_l - T_s) \tag{26}$$

Here, the heat capacity of electron is given by

$$C_e \approx \frac{\pi^2}{3} k_B^2 T D(E_F) \tag{27}$$

The spin heat capacity C_s in three temperature model represents the spin specific heat which reaches the maximum at the Curie temperature. it can be calculated by using the total heat capacity C in bulk materials to substrate the heat capacity of lattice and of electron after the laser induced excitation [1]:

$$C_s = C - C_e - C_l \tag{28}$$

2.2 Microscopic Models for Ultrafast Demagnetization

2.2.1 A challenge of modern physics to explain the Origin of Ultrafast Demagnetization

Although many recent phenomenological models are partially successful to describe ultrafast magnetization dynamics, the intrinsic quantum mechanical mechanisms responsible for ultrafast demagnetization are not clear at all. In a word, the main challenge of understanding the microscopic mechanism of the ultrafast demagnetization is to find the channel of dissipation of angular momentum in the femtosecond timescale. In the following chapter, I am going to discuss possible mechanisms to explain the ultrafast demagnetization phenomenon. The dynamics of collective excitations of electrons, phonons, and spins are of fundamental interest to develop a microscopic understanding of interactions among elementary excitations and of the respective relaxation mechanisms.

2.2.2 Elliott-Yafet Spin-flip events

In general, to flip a spin from excited electrons in ferromagnetic materials, there are three possible mechanisms: (1) an inelastic electron-spin-wave scattering event [39], It applies to the relatively low excitation photon energy (2) a Stoner excitation which is effective at relatively high energies [40]; (3) a single-particle-like spin-flip scattering with impurities or phonons, called the Elliott-Yafet mechanism [41]. In the ultrafast timescale region, the first possible candidate is the Elliott-Yafet mechanism of spin-orbit mediated spin-flip scattering of electrons with phonons. In fact, this mechanism was first proposed for paramagnetic metals before the discovery of ultrafast demagnetization.

Then, Koopmans *et al*. [2] first proposed the idea that spin angular momentum is transferred to the lattice by way of Elliot-Yafet type spin-flip scattering. To explain this observation of phenomena, they proposed the so-called microscopic three temperature model (M3TM), which couples a rate equation for the magnetization to a two-temperature model of phonons and electrons, and combining a theory of Elliot-Yafet scattering which predicts a spin-flip parameter to give a possibly quantitative explain for ultrafast magnetization loss.

$$C_e(T_e)\frac{dT_e}{dt} = -G_{el}(T_e - T_l) + P(t) + \nabla_Z(k_B \nabla_Z T_e) \tag{29}$$

$$C_l(T_l)\frac{dT_l}{dt} = -G_{el}(T_l - T_e) \tag{30}$$

$$\frac{dm}{dt} = \frac{8\alpha_{sf} g_{el} k_B T_C{}^2 V_{at}}{k_B T_C} m \frac{T_l}{T_C}(1 - m\coth(\frac{mT_C}{T_e})) \tag{31}$$

where V_{at} is the atomic volume; k_B is the Boltzmann constant; T_C is Curie's temperature, and α_{sf} determining the initial steepness of the demagnetization transient and g_{ep} determining the cooling down of the electron gas [37].

The process of this scattering is described by an event of probability. The damping parameter α, which is proportional to the probability of spin flip. According to the theory of Koopmans *et al*, we can present a formula to describe the demagnetization time τ_M in femtosecond time scale:

$$\tau_M \approx c_0 \frac{\hbar}{k_B T_C} \frac{1}{\alpha} \tag{32}$$

However, Cinchetti *et al*. [42] claimed to have found experimental evidence for the relevance of the Elliott-Yafet spin-flip processes for the ultrafast demagnetization on a time scale around 300 fs. Furthermore, the X-ray magnetic circular dichroism (XMCD) study can well definite the contribution from orbitals and spin by applying the sum rule [43], unambiguously it was shown that the electron orbitals were not responsible for this fast demagnetization. Therefore, the only possible reservoir should be the lattice. Because of the above-mentioned weak spin-lattice interaction, they argued that this can only be possible if some extra interaction, for example, via light-induced virtual states, enhances the spin-lattice interaction. This finding seems to favor the Elliot-Yafet scattering as the most likely interaction mechanism [30]. Consequently, if the electrons, heavily excited by the energy input of the intense femtosecond laser pulse, are scattered into these spin hot spots in the Fermi surface by defects, phonon-scattering events, etc., the final state has a certain probability to be of opposite spin [36].

In contrast, some evidences are pointed to illustrate that the Elliott-Yafet mechanism may not be the dominant process for ultrafast demagnetization. Here, according to the prediction of Koopmans *et al.* [37] (see equation 32), macroscopic Gilbert damping parameter α is inversely proportional to the ultrafast quenching time. The impurity inside the ferromagnetic thin film is more likely to modify the damping parameter, then after doping Ho, Dy, Tb, and Gd impurities, the Gilbert damping parameter is able to measure through the precession process of ferromagnet in a longer timescale. Then, Radu *et al.* [44] verified this

relation by doping impurities by the rare-earth elements: Ho, Dy, Tb, and Gd into Permalloy films. They investigated magnetization dynamics of Permalloy thin film samples by doping with different rare-earth elements. Unfortunately, the experimental observation is not agreed with the formula above. The dominant fast relaxation process is slowed down by adding slow relaxing impurities. The reason for this is that the model Koopmans *et al.* seem to be oversimplified for the case of 4f impurities [44].

Additionally, Carva *et al.* [45] claimed that the demagnetization rate in thermalized electron distributions as assumed by the M3TM were too small, with only a marginal increase for non-equilibrium distributions occurring in pump-probe experiments. Essert *et al.* [46] proposed that electron phonon spin-flip scattering is hardly to explain all the experimental observation behind the ultrafast demagnetization, furthermore, the dynamical modifications from the band structure near the Fermi level also play an important role, which is not considered in the M3TM.

2.2.3 Spin super-diffusive transport

Alternatively, another mechanism that tries to interpret the ultrafast behavior of the magnetization is named superdiffusive spin transport, firstly proposed by Battiato *et al.* [3]. In this work: they show that spin majority electrons will diffuse more out of the excited region, while spin minority will diffuse much less, leading to a preferential depletion of spin up carriers in the pumped region. The reduction of the number of spin majority electrons will consequently lead to a demagnetization of that region. It has to be noted that if we assume that the probability of spin flip upon scattering is negligible, there is no absolute reduction of the magnetic moment, but simply redistribution to regions far away from the pumped one [3].

From the work of Battiato *et al.* [3], they investigated the curve of a Ni/Al bilayer caused by laser excitation. The essential idea of this design is to allow pump laser to mainly excite electrons from Ni layer, An intuitive picture of the dynamics is that the laser excitation creates a flux of two types of spin polarized electrons with different velocity from Ni layer to Al layer (see figure 2.4). This model points that the spin superdiffusive transport can be a dominate reason for explaining the ultrafast demagnetization.

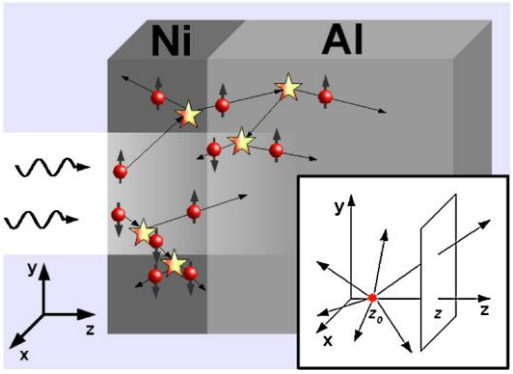

Figure 2.4: A simple sketch of the superdiffusive processes caused by laser excitation. Majority and minority spin carriers show different mean free paths and also a cascade of electrons is generated after an inelastic scattering. The inset shows the geometry for the calculation of the electron flux term in the continuity equation.[3]

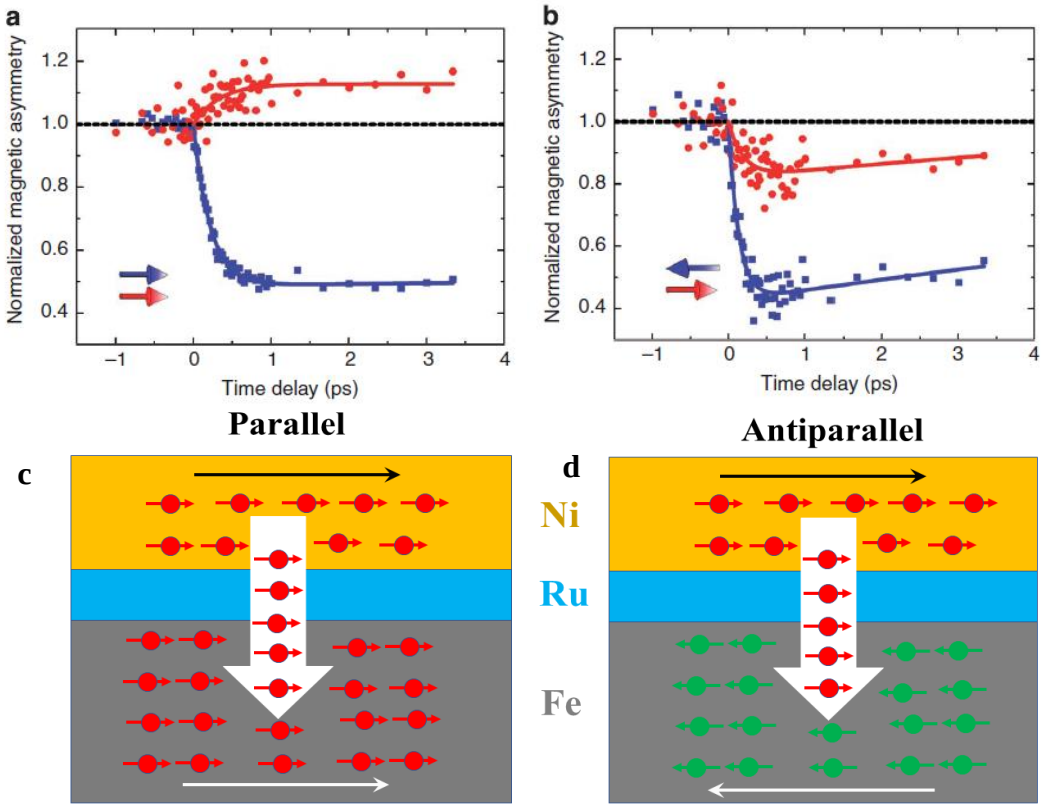

Figure 2.5: Experimentally measured time- and layer-resolved magnetization. The time-resolved magnetization of the Fe and Ni layers in the Ni(5 nm)/Ru(1.5 nm)/Fe(4 nm) trilayer for the parallel (a) and antiparallel (b) magnetization alignment and in the Ni(5 nm)/Ru(1 nm)/Fe(4 nm) trilayer. (c) and (d) illustrates schematically the relative magnetization of the Ni and Fe layers (thin black and white arrows), the majority spin alignment in the layers (red and green circles) and the flow of the spin current (large grey arrow) [47].

Additionally, a study on Fe/Ru/Ni multilayer (Dennis Rudolf *et al*. [47]) provides fundamental insight into spin dynamics between parallel Fe/Ni layer and antiparallel Fe/Ni layer, and a comparison between the amount of reduced and enhanced of magnetization on femtosecond time scale range could quantitatively determine the relevance/contribution of superdiffusive spin transport to the overall demagnetization dynamics, thereby being demonstrated clearly that optically induced demagnetization generates superdiffusive spin current between the layers of Ni and Fe. (see figure 2.5) From these points of view, superdiffusive transport model, to a large extent, obtained a great success to predict the large contribution of non-local majority and minority electrons.

On the other hand, Schellekens *et al.* [48] pointed out that spin transport plays no significant role in the demagnetization process of ferromagnetic thin films on insulating substrates by comparing front-pump with back-pump measurements of Ni/Al_2O_3 films. Even by adding a conductive layer did not enhance significantly the demagnetization rate that is contradicted to the prediction of superdiffusive spin transport model. They conclude that the presence of spin current perhaps is too week to detect, but it is hardly to the dominant effect for explaining the ultrafast demagnetization in Ni ferromagnetic films.

2.2.4 Other microscopic models

Apart from the two mainstream models to explain ultrafast demagnetization, other models have been proposal to explain the sudden loss of spin angular momentum. For example, Carpene *et al.* [49] proposed that an ultrafast reduction is mainly responsible for electron-phonon interactions and electron-magnon excitation. According the fundamental theory of scattering events, the event itself not only modifies the energy and momentum of the particles involved, but they can also induce spin-flips, affecting the net magnetization of the sample. Similar to Elliot-Yafet scattering, this model also considers that the spin-flip always occurs depending on certain probability rate, the difference is that the author added a new reservoir ‘magnon’ to the non-equilibrium system. In particular, the concept of a magnon, which is a quasi-particle, a collective excitation of the electrons’ spin structure in a crystal lattice, was first introduced in 1930 by Felix Bloch [50], in order to explain the reduction of the spontaneous magnetization in a ferromagnet.

Zhang *et al.* [51] proposed that a cooperative effect between the external laser field and the internal spin-orbit coupling leads to the phenomena of ultrafast demagnetization. Once the pump excitation causes the spin-orbit coupling smears out singlet and triplet states, it can statistically open a channel for optically induced spin flips events [51]. Controversially, in order to explain reduction of spin angular momentum, this optically induced channel has to compensate the total angular momentum unchanged [51]. Here, it is possible to estimate the number of photons absorbed in the magnetic material due to pump laser and the number of electrons participate the magnetic switching. While, whether these number of photons is large enough to provide the missing angular momentum of electron system is still an open question. In particular, if there exist the output of angular momentum from the laser, when the pump laser change from linearly or circularly polarized, the demagnetization process logically will be observed differently. Nonetheless, the experimental result proves that any magnetization dynamics measured by magneto-optical response is independent for any polarization changes of pump laser [52] (see figure 2.6).

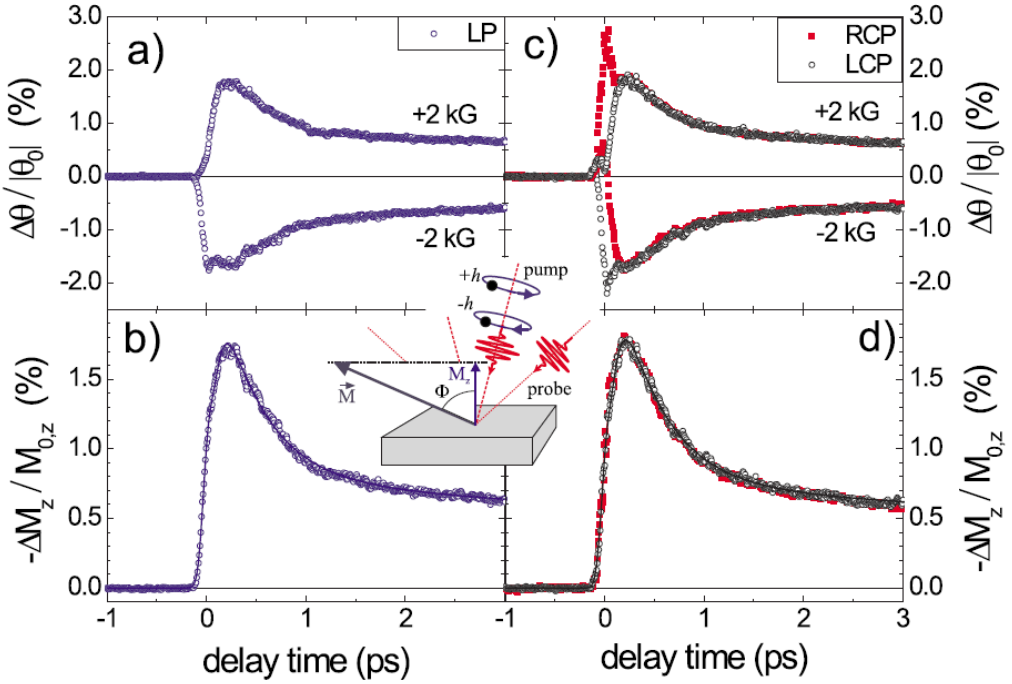

Figure 2.6: Typical TR-MOKE response to (a) linearly polarized and (b) right and left circularly polarized pumping.[52]

In the following chapter of my thesis, we only discuss and use the Elliot-Yafet electron-phonon scattering model and superdiffusive spin transport model, which are supported by most of research, although the underlying mechanism behind are still open questions.

3 Chapter 3: Probing Magnetization Dynamics with Free Electron Laser Sources

Femtosecond lasers are a type of laser that produces optical pulses in femtoseconds. Above all, we should obtain a basic idea of the principle of pump-probe technique, which is applied to resolve processes on ultrafast time-scales. In the following part, I will introduce the basic knowledge of pump-probe spectroscopy, and then it will be easy to understand that time resolution of the measurement is directly determined by pulse duration that makes femtosecond lasers are necessary in our cases. Furthermore, after that I am going to introduce a powerful femtosecond laser source, free electron laser (FEL), that I used during all my experiment.

3.1 Ultrafast pump and probe experiment

Pump and probe technique is the significant method to investigate ultrafast dynamics, which is excited or pumped by an ultrashort laser pulse, while a second laser pulse follows to probe the same sate. In our case, we are interested in the magnetic state of the sample so we are relying on magneto-optical effects to study the system. Through the analysis of the measured signals of the probe pulse after interaction with the studied medium for different time delays between pump and probe pulse, we can reconstruct the complete dynamics process. The time delay usually is controlled by optical mirrors that can modifier the path difference between the pump and probe beams, hence, changing the time delay between them (see figure 3.1). The time resolution is significantly determined by the duration of pump and probe pulses: shorter pulse better time resolution. Thus, in order to study faster process, the only way is to reduce the duration of the laser pulse.

The choice of the pump and probe characteristics goes beyond the pulse duration: energy and wavelength, for example, are important parameters to consider. Usually, in the past majority of studies of ultrafast dynamics, ultrafast Infrared lasers are used [1][52]. The wavelength of the laser is about 800 nm, corresponding to photon energy excitation of 1.6 eV. In the case of ferromagnetic materials like Fe, Ni, and Co, it can excite the electrons in the d band and s-p band up to the Fermi level.

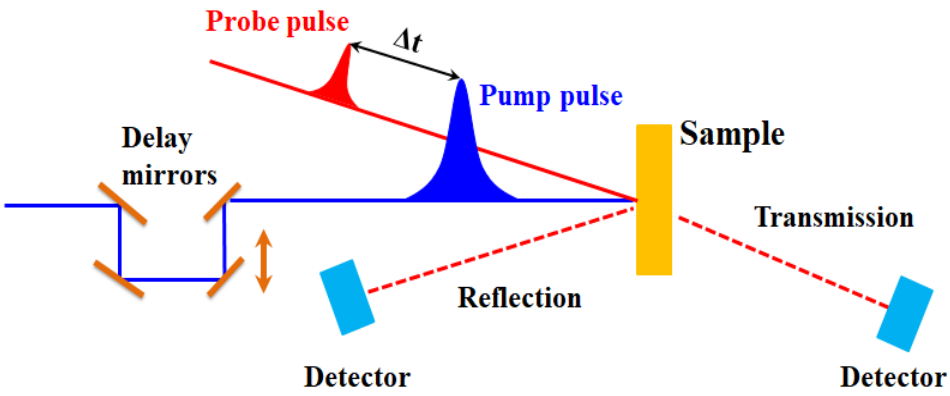

Figure 3.1: A schedule of the principle of pump and probe setup. Δt represents time delay between the pump and probe pulses. Two detectors can collect the information probe signal of transmission and reflection. Delay system is consisted by four mirrors moving with the horizontal steps.

However, it is very important to understand the fundamental mechanism underlying ultrafast dynamics to be able to use different wavelength. In this thesis, I will introduce my experiments using three different wavelengths to pump:

1. Pumped with XUV free electron laser
2. Pumped with Terahertz pulse
3. Pumped with Infrared laser

For the study of ultrafast magnetic dynamics probe beam usually is 800 nm [1] of frequency double 400 nm. Magnetic probe relies on magneto-optical effect such as Magneto-optic Kerr Effect (MOKE) or Faraday Effect. In our group, we probe with XUV Free electron laser with the following advantages:

- Short wavelength access to nano-scale: nanometer spatial resolution is allowed us to image the domain structure of sample.
- High photon number: it is allowed us to have enough photons to do the transmission measurement and acquire a good statistics
- Access to absorption edges of the 3d transition metals: element-specific information can be obtained by tuning the photon energy up to the specific absorption edges of materials like Co, Ni, and Fe
- Ultra-short pulse: it is allowed us to investigate the dynamics process with very good time resolution.

3.2 Femtosecond X-ray sources: Free electron laser

To perform ultrafast pump probe experiment with an x-ray probe, one needs a source of femtosecond x-ray pulses. This type of source has been developing rapidly in the recent years and I can mention the following which are used in my group: synchrotron femto-slicing [53], high harmonic generation (HHG) [54] and free electrons laser (FEL). In this thesis, I will concentrate on the latter.

3.2.1 Principle of a free electron laser

The idea of FEL first proposed in 1971 by Madey [55] and demonstrated experimentally a few years later [56][57]. FELs produce coherent radiation, like more common lasers. They use a beam of free-electrons as the gain medium. Like in a synchrotron, the radiation is produced in an undulator, which has a sinusoidal magnetic field of period (see figure 3.2 (a)). This assembly of permanent magnet submits the electron beam to a sigmoidal magnetic field of a period of the order of centimeters and amplitude of the order of 1 Tesla. The magnetic field forces the electrons to follow oscillating trajectory, which cause the electrons to emit an electromagnetic wave train [58]. The wavelength of the emitted radiation is proportional to the period of the undulator. If one wants to shorten the wavelength of the emitted radiation, one should decrease the size of undulator. X-ray pulses would require an undulator with a nanometer period which is impossible to fabricate so far. However, thanks to the relativistic effect at length contraction, the undulator period appears a lot smaller for electrons approaching to the speed of light [55][56][57]. To reach to the nanometer length scale, electrons have to be accelerated to the energy of the order of the GeV.

However, when the electrons go through the undulator, it is significant to adjust the phase of these no correlated electrons into almost the same. The process is presented in the Figure 3.2 (b), if it is the case of the spontaneous radiation (no correlated) the fields they created randomly and they will cancel the effect with each other. If all the electrons near to each other within a wavelength, and their electromagnetic fields superimpose in phase, the collective behavior of electrons force the amplitude of the electromagnetic field to grow exponentially [58].

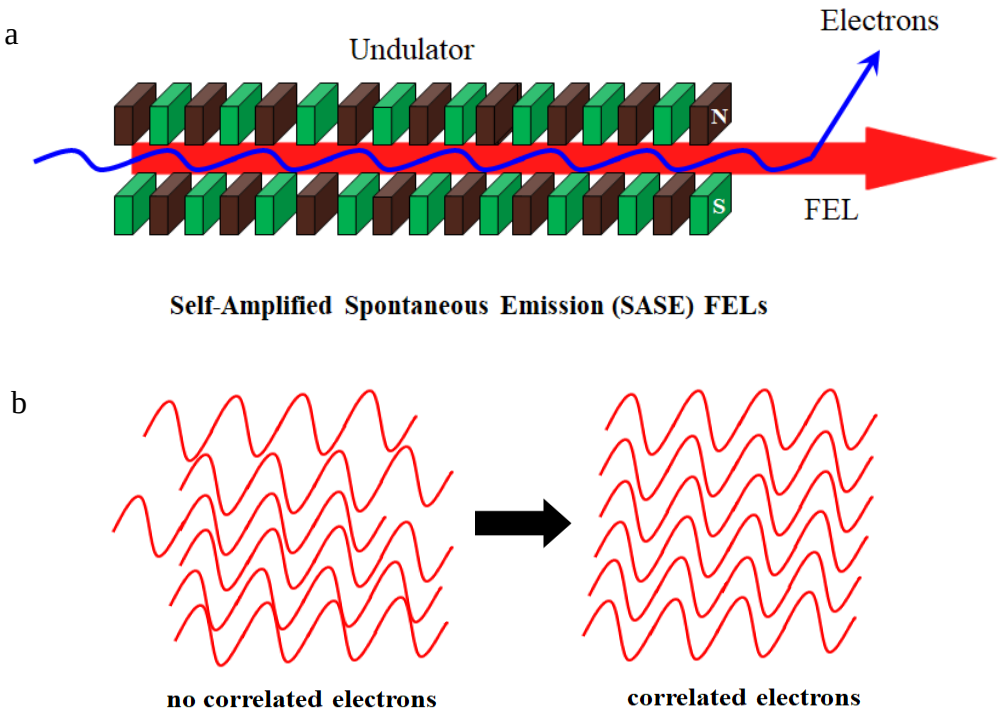

Figure 3.2: (a) The principle of X-ray light generation in an undulator of Self-Amplified Spontaneous Emission (SASE) FELs. The accelerated electrons are forced to follow a wavy path with the aid of magnets, and thereby radiate X-ray light that will be guided to the experiments. The electrons will then no longer be needed and will end up in a beam stop. (b) The superposition of the fields generated from many electrons: the spontaneous radiation case (left), the free-electron laser case (right) [58].

In the following, the oscillated electrons emit light characteristic of the undulator strength but within a certain energy bandwidth. The emitted photons travel slightly faster than the electrons and interact with them each undulator period. Depending on the phase to each other, electrons gain or lose energy (velocity), i.e. faster electrons catch up with slower ones.[59] Thereby called micro-bunching is formed by the different group of electron bunch density which is modulated by the radiation periodically. This is a process of Self-amplified spontaneous emission (SASE) FELs (see figure 3.2 (a)).

Although an excellent transverse coherence has been observed by the radiation from a SASE FELs, it typically has rather poor temporal and longitudinal coherence and relatively large statistical fluctuations. This is because the SASE FELs starts up from the random shot noise in the electron beam [59][60]. To improve the temporal coherence from the SASE FELs,

many efforts have been done. Many high-gain seeded FEL schemes including external seeding [61][62][63][64] or self-seeding [65][66][67] have been developed.

3.2.2 Generation of sub-ps X-ray Free electron lasers (FELs) from the FLASH 1 and FLASH 2 facilities

The soft X-ray SASE free electron-laser (FEL) FLASH [68] at DESY in Hamburg has been an FEL user facility since 2005 [69]. It delivers high brilliance XUV and soft X-ray FEL radiation for photon experiments [69]. The first undulator beamline was in operation since 2004, is referred to FLASH1 and FLASH2 is a new second beam line is built in 2012 and 2013 [70]. Figure 3.3 illustrates the layout of FEL facility, FLASH1 and FLASH2. A superconducting linac is driven by a conducting a photo cathode gun (RF-gun) which offers a train of electron bunches and it can be shared between the two undulator beamlines [68]. Details can be also found in Ref [68].

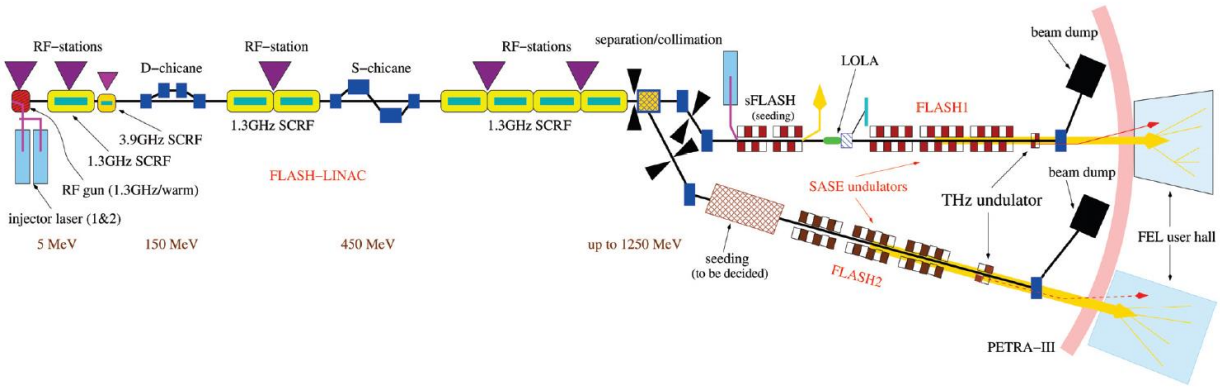

Figure 3.3: Schematic layout of FLASH. It with its two beamlines FLASH1 and FLASH2 on the right (not to scale) [71].

FLASH2 will offer up to six additional photon beamlines in the new experimental hall 'Kai Siegbahn'. Photon beam parameters can be chosen almost independently for FLASH1 and FLASH2 by the users [72]. The variable gap undulators is available at the FLASH2 and thus, the chosen wavelength of FLASH2 is also independent from FLASH1 [72]. Besides, fast tuning of the wavelength. In addition the wavelength scans are possible for users at FLASH2, which is very important for our experiment. Each undulator line has its own injector laser and thus bunch separation, number of bunches, and the bunch charge can be set independently for FLASH1 and FLASH2. Both undulator lines receive the full 10 Hz bunch train repetition rate, but each 800-microsecond long burst is split between FLASH1 and FLASH2 [73][74]. The

fraction of bunches delivered to each beamline can be chosen freely. A novel flexible RF-system allows different compressions for FLASH1 and FLASH2, and thus users can chose a different photon pulse length [73][74].

In order to characterize a coherent radiation source, we should define the peak brilliance by the equation below [75]:

$$\text{brilliance} = \frac{4N_{ph}}{\lambda^2 \sigma_t \sigma_\omega} \tag{33}$$

where λ is the wavelength of the radiation, and N_{ph} is the number of photons, σ_t represents the duration of the light pulse and σ_ω is the spectral width.

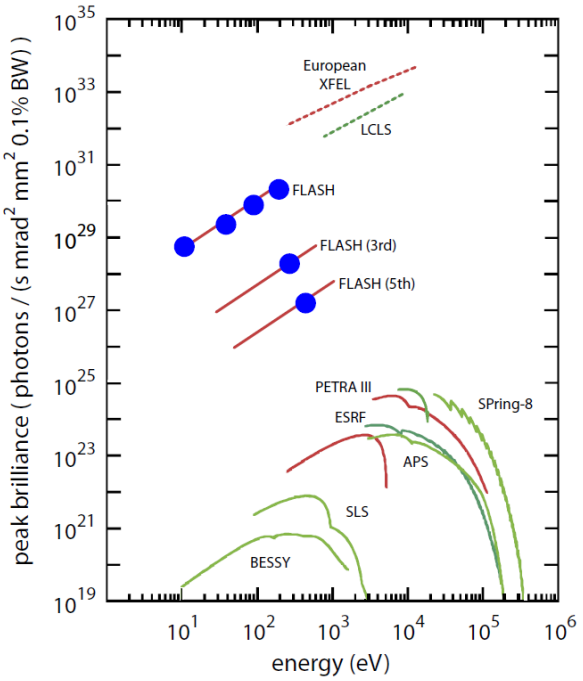

Figure 3.4: The peak brilliance of synchrotron radiation sources and existing free-electron lasers sources [75].

Figure 3.4 shows that FEL sources realized a great jump in terms of the peak brilliance and at the same time dramatically improved the temporal resolution well below 10 fs, that a record is unreached yet on synchrotron radiation sources. The great progress of source brilliance and resolution allow modern scientists to further investigate the ultrafast world.

3.3 Sample fabrication and characterization

3.3.1 Magnetron sputtering technology

Magnetron sputtering is thin film deposition technology that we use for the fabrication of the samples in our experiment (see figure 3.5). It is based on a plasma coating process whereby sputtering material is ejected due to bombardment of ions to the target surface. The vacuum chamber of the sputtering machine is filled with an inert gas, in this case: Argon. The background pressure was about 2×10^{-8} Torr and sputtering was performed in 3 mTorr Argon. By applying a high voltage, a glow discharge is created, resulting in the acceleration of Ar ions to the target surface between a substrate and the target. The Ar-ions will eject materials from the target surface, which will be deposited on the substrate. Several targets are available in the chamber to be able to deposit different materials on the same substrate. The samples are either grown on Si wafers or on Si_3N_4 membranes. The Si_3N_4 membranes allow for experiments in geometry of transmission.

The growth rates are measured by using a quartz balance. They are fairly sensitive to the chamber pressure and to the voltage. Hence, these two parameters are controlled precisely. The motor is fully computer-controlled.

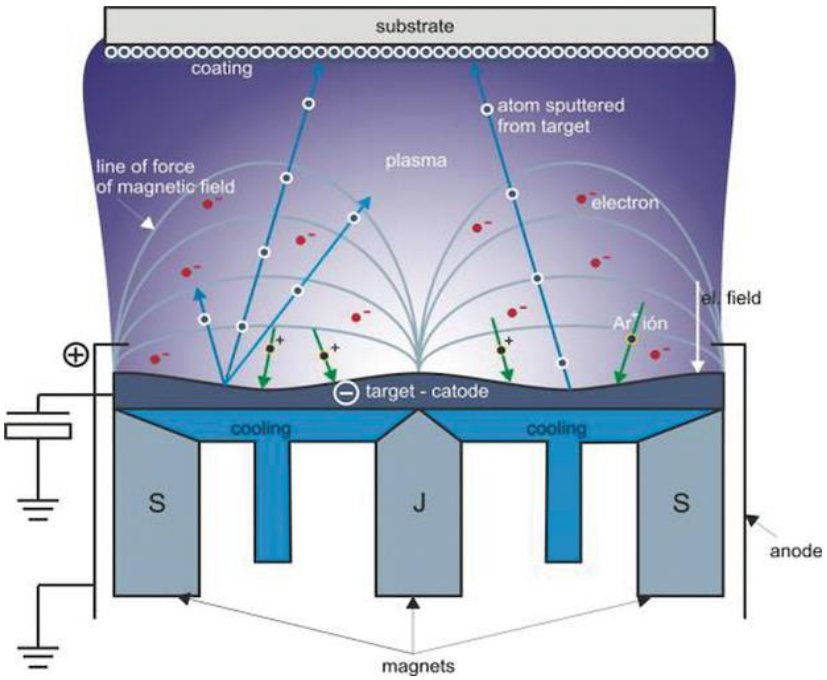

Figure 3.5: Principle of Magnetron sputtering (source: Slovak Academy of Science [70]). A substrate is placed in a chamber at a pressure around 10-8 mbar in front of a target made of the material we

want to deposit. A small flow of neutral gas is introduced in the chamber (typically Argon) and a high voltage is applied to the cathode (the target). The neutral gas atoms are ionized by the electric field and create plasma. The magnetic field generated by a permanent magnet situated under the target keeps the atomic species of the plasma along its field lines close to the target. Neutral atoms sputtered from the target escape from the plasma and deposit on the surface of the substrate.

3.3.2 Characterization of the magnetic properties of the sample

The magnetic characterization of the sample is a key prerequisite for the detection and control of the multilayer growth quality. All the fabricated samples are thus characterized using magneto-optical Kerr effect (MOKE).

Because of this effect, linearly polarized light reflected from a magnetized sample will become elliptically polarized and will undergo a rotation of polarization. By measuring this rotation or ellipticity, we can retrieve the magnetization of the sample. MOKE is a highly sensitive technique (single atomic layer can be detected) it can only probe the surface of the sample.

There are three main MOKE configurations depending on the direction of the magnetic field with respect of the sample surface and the plane of incidence (see figure 3.6 (a)): longitudinal, polar and transverse. With our equipment, we can measure longitudinal and polar MOKE corresponding to the in plane and out of plane magnetization. The most basic MOKE system consists of the following elements: a laser source, a polarizer, an electromagnet, an analyzer and a detector (see figure 3.6 (b)).

Our actual setup is a bit more complicated, but the idea remains to be able to measure the MOKE rotation and ellipticity.

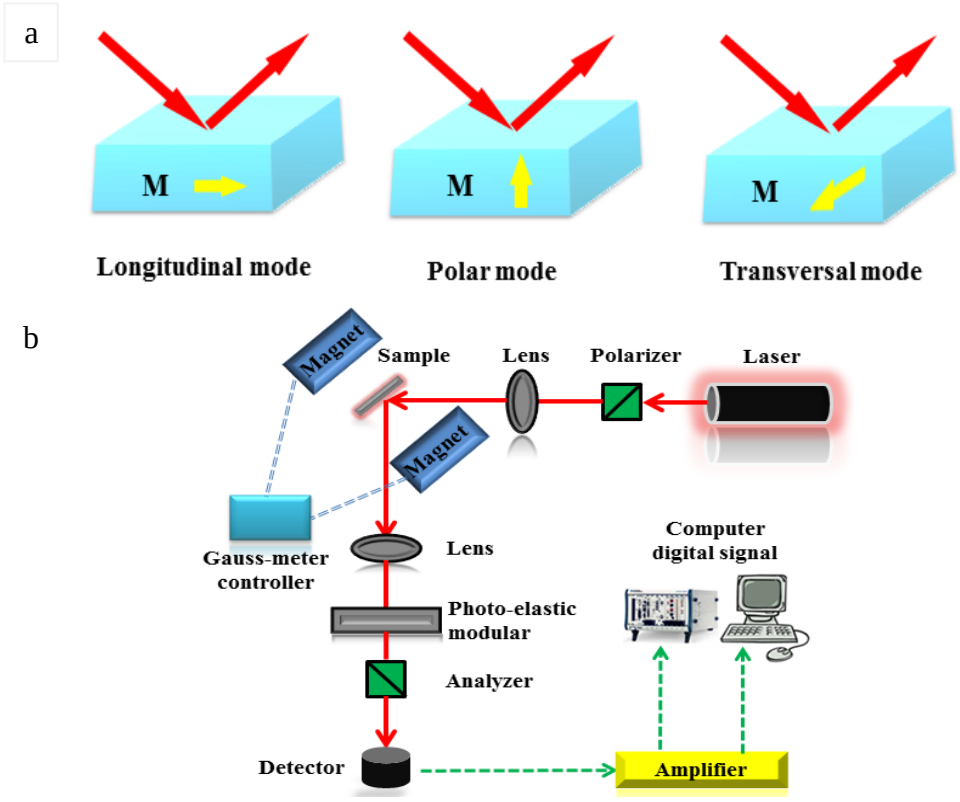

Figure 3.6: (a) MOKE geometries, the red arrows represent the incident and reflected light and the green arrows represent the direction of the magnetic field. In longitudinal mode, the field is in the plane of the sample and in the plane of incidence. In polar mode, the field is perpendicular to the sample surface and in the plane of incidence. In transverse mode, the field is in the plane of the sample and perpendicular to the plane of incidence. (b) The most basic MOKE configuration the light of a laser source is linearly polarized by a polarizer with a high extinction ratio. The light is then reflected by the sample which is magnetized by an electromagnet.

Figure 3.7 shows hysteresis loops of single layer Co, a $[Co_{0.6}/Pt_{0.8}]\times7$ multilayer and a $[Co_{0.6}/Pt_{0.8}]\times20$ multilayer. The single Co layer shows the typical behavior of a ferromagnetic thin films, i.e. in plane magnetic anisotropy, which is easy to magnetize in plane (square loop with low coercive field) and hard to magnetize out of plane. The $[Co_{0.6}/Pt_{0.8}]\times7$ multilayer exhibit the opposite behavior: easy to magnetize out of plane and hard to magnetize in plane. This out of plane anisotropy is due to the interaction between the Co and the Pt layers. When the number of repetition increases, the hysteresis loop of this type of multilayer evolves $[Co_{0.6}/Pt_{0.8}]\times20$. The loop is not a square anymore because it cost less energy to the system to break into small magnetic domains at zero fields than to form a single domain. This type of structure will be worked for the resonant scattering experiments [77].

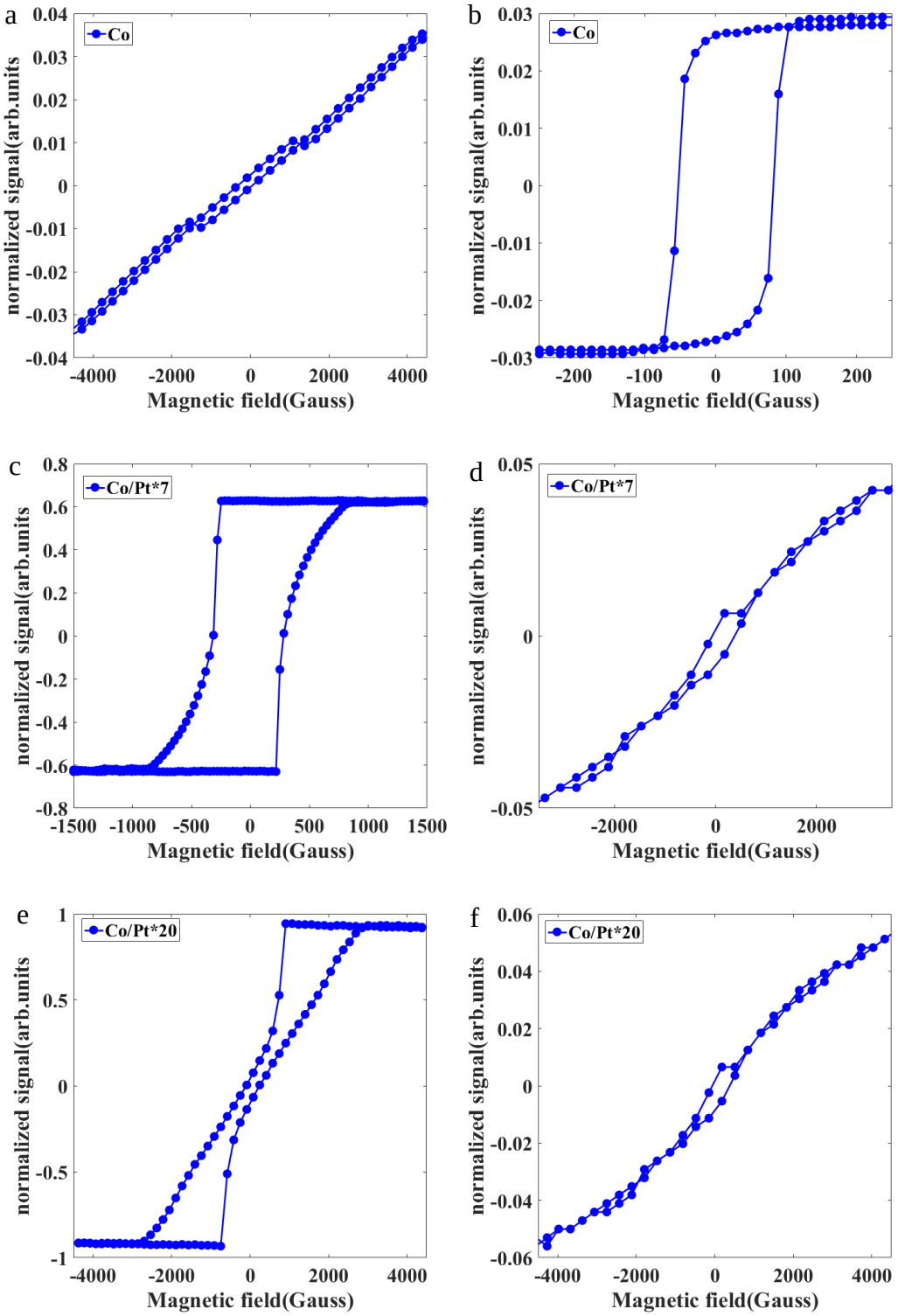

Figure 3.7: Static magnetic properties and geometry of the sample. Hysteresis loop of single Co(20nm) measured by (a) polar mode and (b) longitudinal mode; Hysteresis loop of 7 repeating of Co(0.4nm)/Pt(0.8nm) measured by (c) polar mode and (d) longitudinal mode; and hysteresis loop of 20 repeating Co(0.6nm)/Pt(0.8nm) layer measured by MOKE spectroscopy with the polar mode (e) and longitudinal mode (f).

3.4 Experimental Methods of Magnetization dynamics Measurements

In this chapter, I am going to discuss three methods of magneto-optic measurements in the range of XUV that I used for the next chapters:

- Resonant Transverse Magneto Optical Kerr Effect (T-MOKE)
- Resonant magnetic scattering
- Faraday Effect

3.4.1 Transverse Magneto Optical Kerr Effect (T-MOKE)

As mentioned earlier, in T-MOKE geometry, the sample is magnetized in plane but perpendicularly to the plane of incidence. In this configuration the reflectivity of p-polarized light (linearly polarized in the plane of incidence) will depend on the amplitude and the direction of the magnetization (see figure 3.8). We can this retrieve the magnetization of the sample by measuring its p-reflectivity [78].

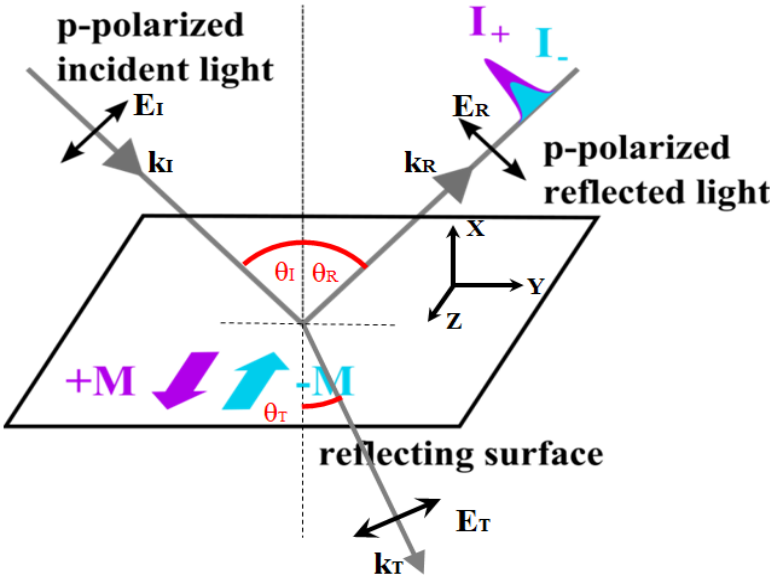

Figure 3.8: Geometry of T-MOKE. M+ and M- represents the two opposite external applied magnetic field, corresponding to I+ and I- signals that measured.

T-MOKE is usually very weak at visible wavelength but is becomes huge in the XUV at wavelength in resonance with absorption edges. For example, at the Co $M_{2,3}$ edge (about 60eV), the ratio between the reflectivity of a single 10 nm Co layer for opposite magnetization directions reaches the value of 4 (see figure 3.9). Moreover, for XUV wavelength, T-MOKE is easier to measure than polar or longitudinal MOKE, since it does not

necessitate a polarizer which is difficult to produce at these wavelengths. However, as a reflectivity technique, T-MOKE is mostly sensitive to the surface of the sample. More qualitatively, we can write the intensity of the reflected beam in T-MOKE geometry for two opposite direction of magnetization (+and -) as follows:

$$I_{\pm}^{P} = I_0 \left| \frac{n\cos\theta_I - \cos\theta_T}{n\cos\theta_I + \cos\theta_T} \pm \frac{2\sin\theta_I \cos\theta_I}{n^2(n\cos\theta_I + \cos\theta_T)} \varepsilon_{xy} \right|^2 \tag{34}$$

where I_0 is the intensity of incident beam, n is the refractive index, θ_I is the angle of incidence, θ_T is the angle of refractive, and ε_{xy} is the off diagonal element of dielectric tensor.

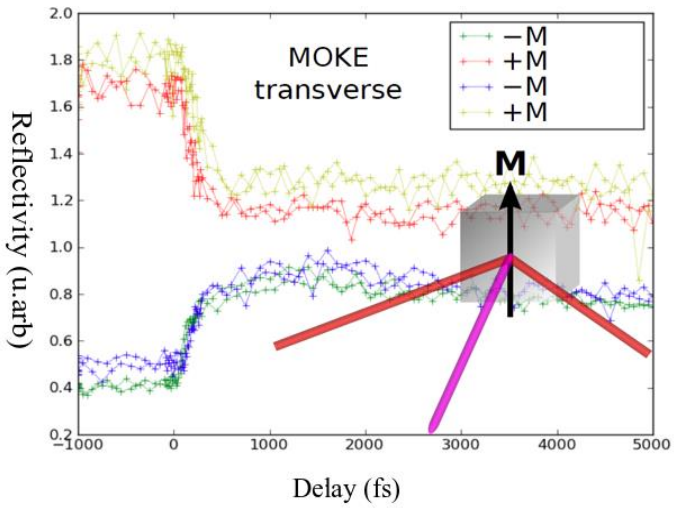

Figure 3.9: T-MOKE signal as the function of time delay. M+ and M- represent two opposite magnetic directions.

This expression is only valid for a single magnetic layer but it is interesting to understand the properties of T-MOKE. We can then write the asymmetry parameter which is defined as follows:

$$A = \frac{I_+^P - I_-^P}{I_+^P + I_-^P} \tag{35}$$

By assuming that the magnetic contribution is small compare to the Fresnel coefficient, we can then write:

$$A = 2\,\mathrm{Re}\left(\frac{\varepsilon_{xy} \sin 2\theta_I}{n^4 \cos^2\theta_I - n^2 + \sin^2\theta_I} \right) = 2\,\mathrm{Re}\left(\frac{\varepsilon_{xy} \sin 2\theta_I}{(n^2-1)n^2 - \sin^2\theta_I (n^2+1)} \right) \tag{36}$$

From this equation, we can deduce that the asymmetry is maximized at 45° of incidence and that it is linearly proportional to the magnetization since ε_{xy} is also linearly proportional to the magnetization.

3.4.2 Resonant Magnetic Scattering

As shown previously, depending on their domains, magnetic thin films with out of plane magnetic anisotropy can break down into magnetic domains at nanometer size. Their domains having opposite magnetization directions, their optical index for right circularly polarized can be written:

$$n = 1 - (\delta \pm \Delta\delta) + i(\beta \pm \Delta\beta) \quad (37)$$

where δ and β are the dispersive and absorption part of the optical index and $\Delta\delta$ and $\Delta\beta$ are magnetic contribution. $\Delta\delta$ and $\Delta\beta$ are usually extremely small except for photon energies in resonance with some absorption edges of the elements studied (see figure 3.10 (b)).

The magnetic domain structure with a succession of area with optical index M+ and optical index M- can then be viewed as a grating (see figure 3.10 (c)). This can be visualized when the domains are aligned. Domains alignment can be achieved by a specific demagnetization procedure. In that case, the magnetic domains structure acts as a square grating and the light is scattered into a plus and minus first diffraction orders (see figure 3.10 (a)). The same reason can be done for left circularly polarized light, resulting in the same scattering pattern. Since linearly polarized light can be decomposed in the sum of right and left circularly polarized field of equal intensity.

The scattering pattern can be observed for linearly polarized light. This is shown in (see figure 3.10 (d)). In a $[Co_{0.2\ nm}\,Pt_{0.4\ nm}]\times 30$ multilayer at absorption energy of about 60 eV (close to the $M_{2,3}$ edge of Co). The diffracted intensity in the peak is proportional to $\Delta\delta^2 + \Delta\beta^2$ and hence to M^2 ($\Delta\delta$ and $\Delta\beta$ being linearly proportional to M). We can then measure the magnetization of the dynamics by following the intensity of the scattering peaks.

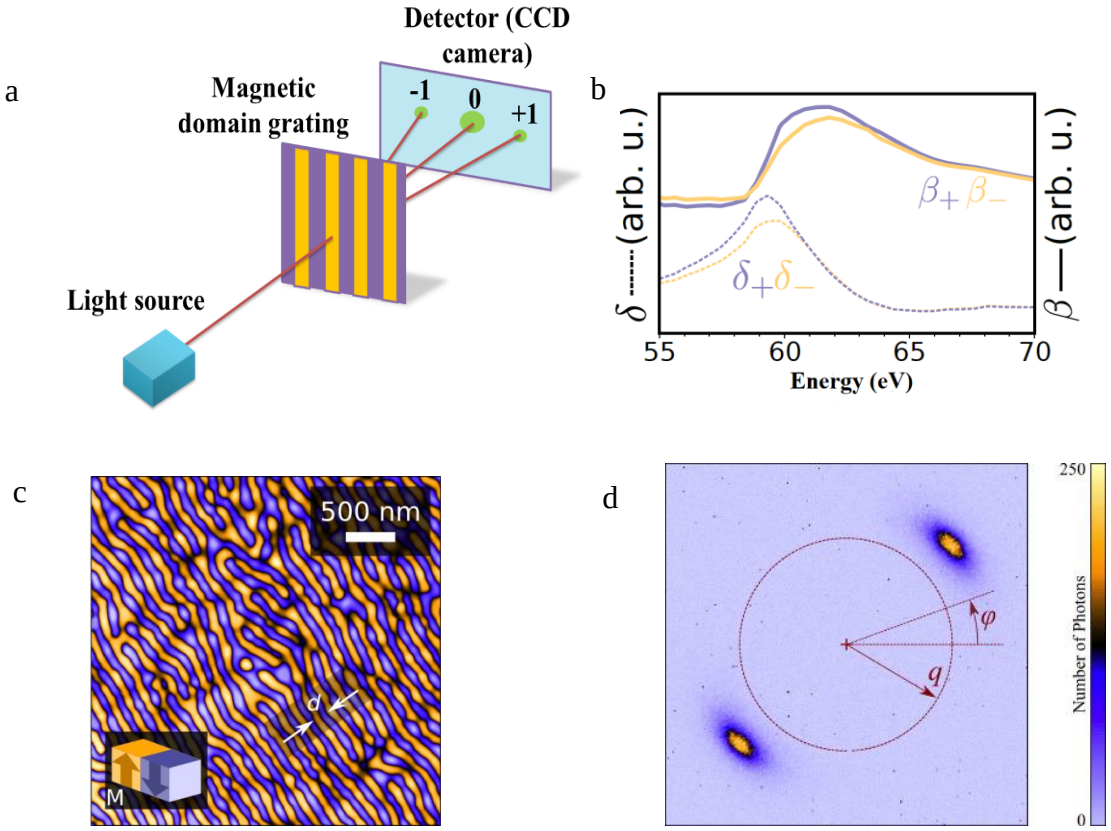

Figure 3.10: (a) Schematic representation of structure as a grating diffraction light into 2 symmetric diffraction orders; (b) δ and β as the function of photon energy; the + and – represents first negative and positive order of scattering pattern; (c) magnetic force microscopy image of aligned domain structure of $[Co_{0.2\ nm}\ Pt_{0.8\ nm}]\times 20$ multilayer; (d) scattering pattern obtained from the actual domain structure at photon energy of 60eV (in resonance with the Co $M_{2,3}$ absorption edge).

3.4.3 Magneto-optical Faraday Spectra

The Faraday Effect is very similar to the Kerr effect. It consists in a rotation of the plane of polarization light propagating in a magnetized medium [79] (see figure 3.11).

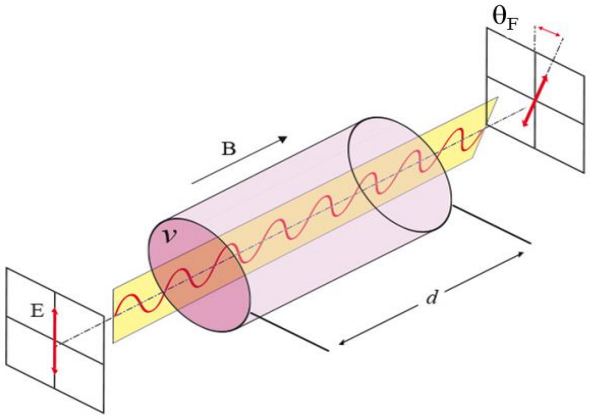

Figure 3.11: Faraday Effect or Faraday rotation. An interaction between light and a magnetic field in a medium [75].

The simplified relation form between the angle of rotation of the polarization β and the magnetic field B presents in Equation below, here the rotation angle is proportional to the strength of the magnetic field.

$$\beta = vBd \tag{38}$$

where d is the length of the path (in meters) where the light and magnetic field interact and ν is the Verdet constant for the material, which depends upon both the properties of the medium, the ambient temperature, and the wavelength, λ, of the incident light [75].

Since linearly polarized light can be decomposed into these two circularly polarized waves, having identical amplitude, but opposite helicity, the Faraday rotation can be explained as follows: when the right and left polarized components propagated through the media, they actually have different velocities that causing a phase shifts, and the Faraday rotation. In addition, the absorption coefficients of the two circularly polarized waves are different, therefore the amplitudes of their electric fields varies differently, which changes the initially linearly polarized light into elliptically polarized after transmission. The two circularly polarized eigenmodes can be described by the complex refractive indices n±:

$$n = 1 - (\delta \pm \Delta\delta) + i(\beta \pm \Delta\beta) \tag{39}$$

where the δ and β stands for the dispersive and absorptive component, then the Δβ can be considered the magnetic contribution, which related to the different absorption of left and right circularly polarized light components. And Δδ comes from the difference in the phase of

the two circularly polarized waves. One can obtain the relation from measuring the Faraday ellipticity ε_F as well as the Faraday rotation θ_F to the refractive indices n± for left- and right-circularly polarized light [80].

$$\left(\frac{1-\tan\varepsilon_F}{1+\tan\varepsilon_F}\right)e^{2i\theta_F} = e^{\frac{iwd\left(n_+ - n_-\right)}{c}} \tag{40}$$

From which we can obtain the relations below:

$$\theta_F = \frac{E_{photo}d}{\hbar c\tan\theta_t}\Delta\delta \tag{41}$$

$$\tan\varepsilon_F = \frac{E_{photo}d}{\hbar c\tan\theta_t}\Delta\beta \tag{42}$$

The above expressions illustrate that θ_F and $\tan\varepsilon_F$ are linearly proportional to the magnetization. To measure them, we will use an XUV polarizer which will be described later.

3.5 Magneto-optics measurement in ultrafast dynamics

During more than 50 years, time-resolved magneto-optics paves a way to measure magnetization dynamics in ferromagnetic metals on the sub-picosecond time scale [1]. Nearly all the experiment studying to ultrafast magnetization dynamics use magneto-optics effect as probe of the magnetization state. Although many static magneto-optics measurements by pioneering work have proved that magneto-optics truly reflect the magnetization state of ferromagnetic materials [81], recent experimental observations [82][83][84][85] raised a long-going debate on whether this remains true on the femtosecond timescale.

Koopmans *et al.* [83] first performed time resolved optical MOKE on Ni (111)/Cu/Ni epitaxial films, measuring Kerr rotation and ellipticity simultaneously, they found that a notable difference between the two signals in the time range of the first 400 femtoseconds. Over the following 1.5 picoseconds, this deviation becomes small, perhaps negligible. Then Kampfrath *et al.* [85] presented their result on the iron thin films that differences are found for the magneto-optic response when measured at different probe laser wavelengths (400 versus 800 nm). They concluded that nonmagnetic contributions prevent the determination of the magnetization dynamics.

However, the debate seems to end with Bigot *et al.* [84]. Their experimental observation shows that magneto-optical signals truly reflect the spin dynamics in a ferromagnet in the femtosecond time scale. Specifically, they probe the $CoPt_3$ thin films by the wavelength of 620 nm and 530 nm with the MOKE and Faraday geometries, the magneto-optical contrast is not highly affected by probing with different wavelength as well as configuration of magneto-optical method. Later, Carpene *et al.* [82] also support that MOKE in the femtosecond regime is a genuine that probes of magnetization. In this thesis, I assume that the magneto-optical effects I use truly reflect the magnetization state of the sample s also in the XUV wavelength range.

4 Chapter 4: Ultrafast Magnetic Dynamics in Permalloy Studied by X-ray Pump X-ray Probe Technique

4.1 X-ray pump and X-ray probe experiment for the study of sub 5-fs ultrafast magnetic dynamics in ferromagnetic alloy by time-resolved T-MOKE

4.1.1 Introduction

Recently, the question of the different Ni and Fe ultrafast magnetization dynamics in Permalloy (Py, $Ni_{80}Fe_{20}$ alloy) arise: should their spin dynamics be the same or different and should the dynamics of these elements be similar to that found in pure materials. Mathias *et al*. [86] and Jana *et al*. [87] claimed that they obtained quite similar demagnetization dynamics of Ni and Fe in Py by using a near infrared (NIR) pump and an element-specific HHG probe time-resolved T-MOKE measurement: they found that Fe is faster than Ni with a small delay (~10 fs) between their two dynamics. However, using a near infrared (NIR) pump and a X-ray magnetic circular dichroism (XMCD) probe measurement from femto-slicing facility, Radu *et al*. [88] observed that Ni and Fe have very different magnetization dynamics in a Py sample: and that Ni is faster than Fe.

To study the question above in more details, evidently a good time resolution and ultra-shot pulses are required (better than 10 fs). However, the traditional Infrared-pump and XFEL-probe technique is constraint by the pulse duration of the infrared laser (typically between 20 and 35 fs) and the x-ray arrival time jitter degrades the time resolution even further (for infrared pump – X-ray probe experiment). Recent developments at XFEL facilities allow now the generation of few femtosecond X-ray probe. Our goal is to exploit this recently developed short pulse mode in a split-and-delay experiment. Ideally, by splitting such an incident X-ray pulse to use it as pump and probe, the time resolution of the experiment is uniquely determined by the X-ray pulse length. This will enable us to study with an estimated sub 5 fs time resolution the onset of the magnetization dynamics to resolve the fine details of the Fe and Ni alloy system, which has not been possible so far.

In the following, I will describe the XFEL Split-and-delay device that we developed, built and installed at the FLASH 2 facility (DESY, Hamburg). The easily tunable wavelength of this source provides the possibility to probe element-specific magnetization dynamics for Ni and Fe. I will show the results obtain on the Py system in two different geometries: in reflection (T-MOKE) and transmission (Faraday Effect).

4.1.2 Instrument description

The device consists of one flat rectangular mirror (120×20 mm) and two spherical mirrors (focal length of about 1500 mm). The flat mirror (splitting mirror) is cutting into the incoming beam with a grating angle of 1.4 degree. The majority of the FEL passes directly and reaches the first spherical mirror (pump mirror) which focuses it onto the sample: this constitutes the pump beam. The reflected beam reaches the second spherical mirror (probe mirror) and is also focused onto the sample: this constitutes the probe beam. Both pump and probe mirrors are coated with a wide band (52 to 67eV) multilayer. The delay between pump and probe is given as follows:

$$\Delta t = \frac{\Delta d}{c} = \frac{AB + BD - (AE + ED)}{c} \tag{43}$$

where AB is the distance between the splitting mirror and the pump mirror, BD is the distance between the pump mirror and the sample, AE is the distance between the splitting mirror and the probe mirror, ED is the distance between the probe mirror and the sample and c is the speed of the light.

The distance AB is set to 1200 mm and the distance BD is chosen so that the pump beam is slightly out of focus on the sample (BD ~ 1510 mm). Since the focal length of the probe mirror is a bit longer than 1500 mm, the probe area is smaller than the pump area (see figure 4.2 (a) and (b)) and is homogeneously excited over the complete range of delays explored (about 10 ps). The pump mirror is fixed and the delay is changed by moving the probe mirror. The motorized stage used for this motion is set parallel to the (ED) direction in order to ensure that the probe beam is always focused along the (ED) direction. Due to the fact that φ is very small (almost normal incidence on the probe mirror), the usual relationship between the distance travels by the delay stage, 1, and the time delay, Δt, holds $\Delta t = 2l/c$.

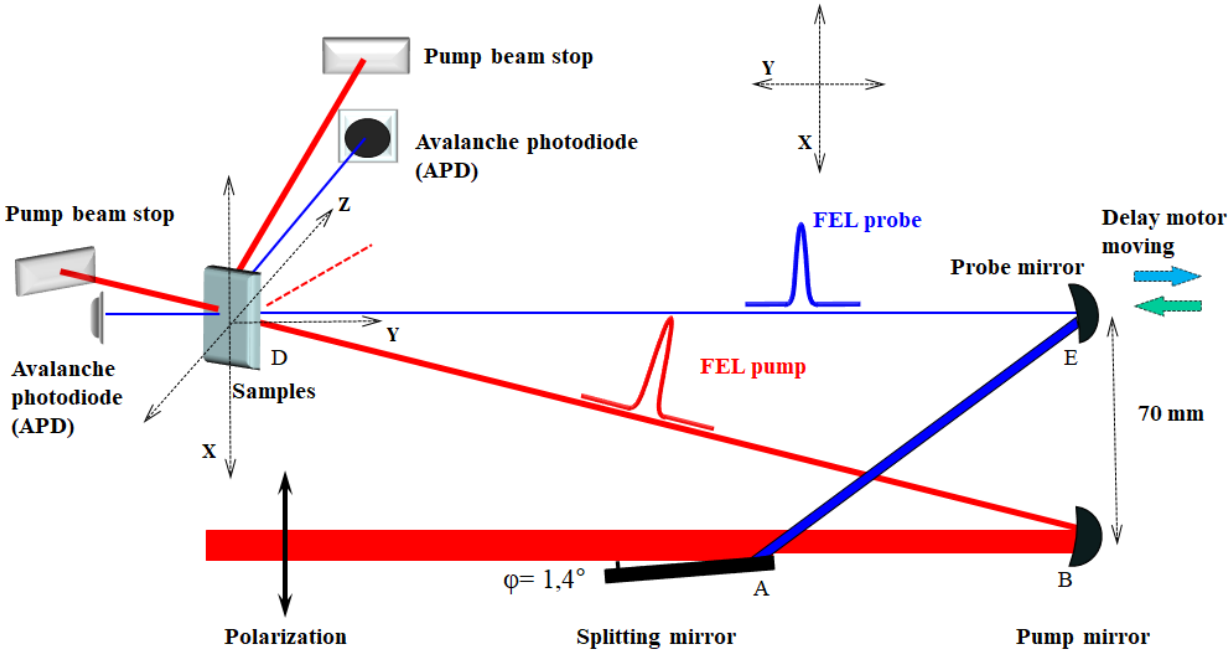

Figure 4.1: A schematic diagram of split and delay experimental setup. The splitting mirror separates the FEL beam into probe (blue line) and pump (red line) beams focused onto the sample by two spherical mirrors. The probe mirror is mounted on a delay stage. An avalanche photodiode (APD) records the reflected or transmitted signals.

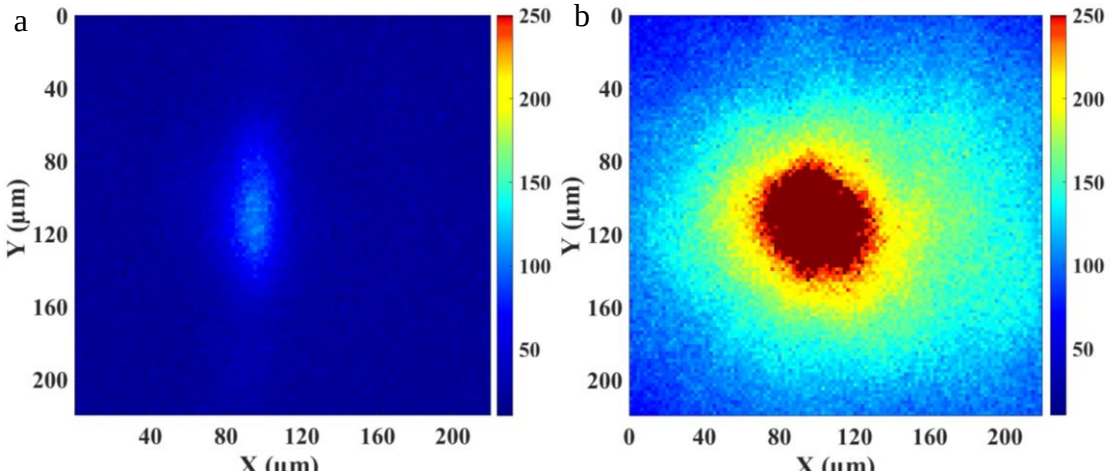

Figure 4.2: Probe (a) and pump (b) beam profile observed on an yttrium aluminum garnet (YAG) crystal situated at the sample position. Both images have the same color scales showing that the probe beam is smaller than the pump beam. The profile of the probe beam does not change much while changing the delay over a 10 ps range (1.5 mm) since the Rayleigh length is a few mm.

The pump mirror being fixed, the spatial overlap is obtained by rotating the probe mirror. The position of the two beams is observed by imaging a YAG screen with a camera.

To ensure that the two beams remain overlapped during the experiment vibration has to be kept at a minimum. Indeed, if we want to keep the positions of the two beams within 10 μm of their initial positions, the angle of incidence on each mirror has to be kept below 10 μ rad. This is achieved by using a low vibration design for the mirrors mounts and by isolated the vacuum chamber from any vibration source, especially the vacuum pumps.

The profile of the beam also allows us to estimate the pump fluence on the sample by taking into account the reflectivity of the different element in the system. From this calculation, we are confident that we can reach a pump fluence of at least a few mJ/cm² sufficient to demagnetize the different samples.

4.1.3 Reflection geometry

The first X-ray pump – X-ray probe experiments we realized were conducted in reflection geometry. We exploit the T-MOKE effect to probe the magnetization of the sample. In this geometry, the sample is magnetized in plane, perpendicularly to the plane of incidence by an electromagnet (see figure 4.3) delivering a maximum field of 200 Gauss. The samples are set at an incidence angle of 45° to maximize the T-MOKE signal (see chapter 3). After the sample, the probe beam intensity is detected with an avalanche photodiode (APD) while the pump beam (which is also partly reflected by the sample) is blocked by a beam stop.

We have studied two samples: a 10 nm thick Ni film and a 10 nm Py film. Both samples were grown on silicon substrates by magnetron sputtering. A 10 nm buffer layer was used to obtain good magnetic properties and the samples were capped by a 10 nm Al layer to prevent oxidation. Because of the shape anisotropy, the sample can be easily magnetized in plane (see figure 4.4) with a low magnetic field of less than 200 Gauss.

The FEL delivers a train of pulses (up to a few hundreds but we typically used 20) separated by a few microseconds (typically 10) at a 10 Hz repetition rate (thus every 100 ms): this corresponds to 200 pulses per second. Each of these pulses is split in two and constitutes one pump – probe event. For each time delay, we record several hundreds of this event for both direction of magnetization. The field is continuously applied to the sample so the magnetic state is reset after each event. We also record the unpumped signal (by blocking the pump beam) for both direction of magnetization. For this first experiment, duration of pulses is about 20 fs and the intensity is about 30 μJ.

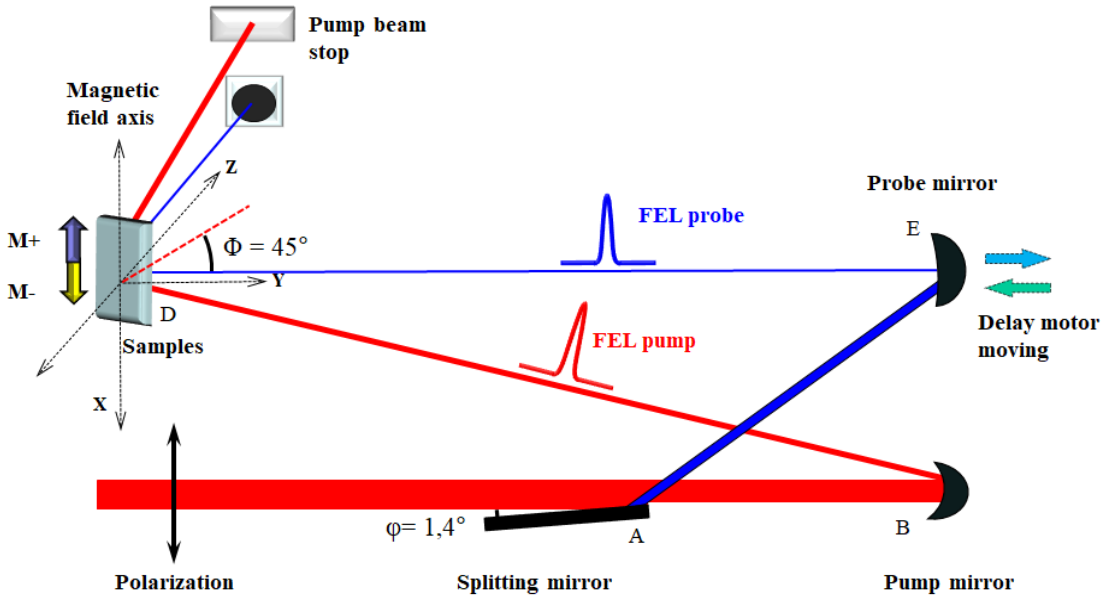

Figure 4.3: A schematic diagram of split and delay experimental setup in the reflection geometry.

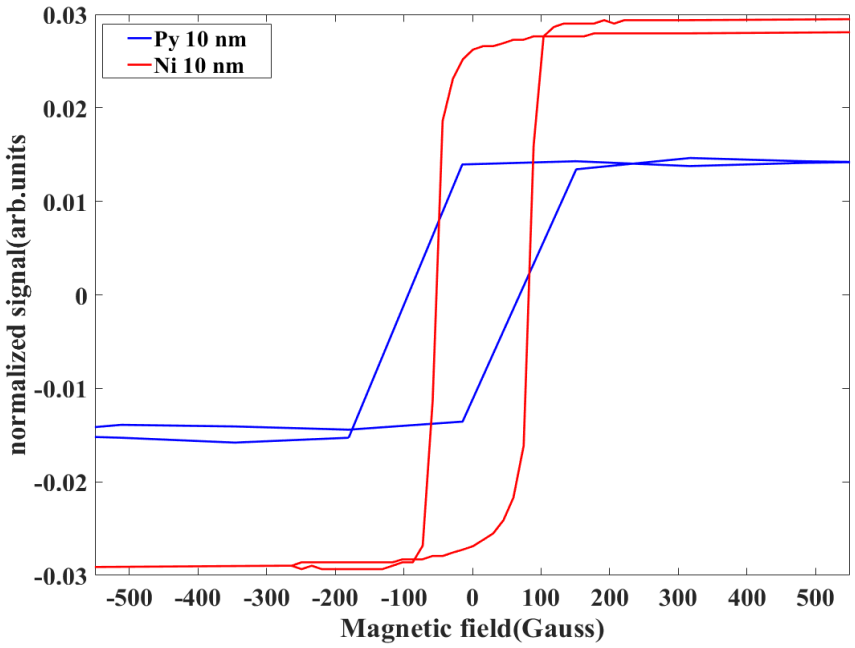

Figure 4.4: Two hysteresis loops of Py (10 nm) and Ni (10 nm) thin films measured by longitudinal MOKE.

Figure 4.5 (a) shows these four measurements as a function of delay recorded at a photon energy of 67.7 eV, in resonance with the Ni $M_{2,3}$ absorption edge, for the nickel sample. We can clearly observe the T-MOKE effect since there is a factor of two between the reflectivity of the sample for the two opposite directions of magnetic field. We can also see the demagnetization effect on the two pumped curves: the reflectivity of these two curves get

closer after time zero. As explain in chapter 3, to better quantify the demagnetization we will use the asymmetry parameter which is defined as follows:

$$A = \frac{I_+^P - I_-^P}{I_+^P + I_-^P} \tag{44}$$

The asymmetry obtains with the pumped curves clearly exhibit the classical behavior of ultrafast demagnetization with a reduction of the signal in the first few hundreds of femtosecond followed by a slow recovery (see figure 4.5 (b)). The unpumped asymmetry shows a gradual decrease which is due to the slow contamination of the surface sample during the experiment. To correct for this effect, in the following the pumped asymmetry will be divided by the unpumped asymmetry. This first measurement shows that the XUV pump triggers a similar magnetic dynamic in the sample than an IR pump and that our experimental setup works as expected.

We observe a slight decrease for no pump curve in figure 4.5 (b). The foregoing data analysis shows that the slope of the decline for no pump curve remains identical quantitatively. The possible reason for this unexpected uncertainty is from the fluctuation of the Ni sample surface or possibly the contamination from optics: the thermal expansion of pump and probe mirror and the weak diffracted light from the edge diffraction of splitting mirror. However, in the following step, the average value of no pump asymmetry is calculated and divided by pump asymmetry, in a large extent, to reduce this weak influence.

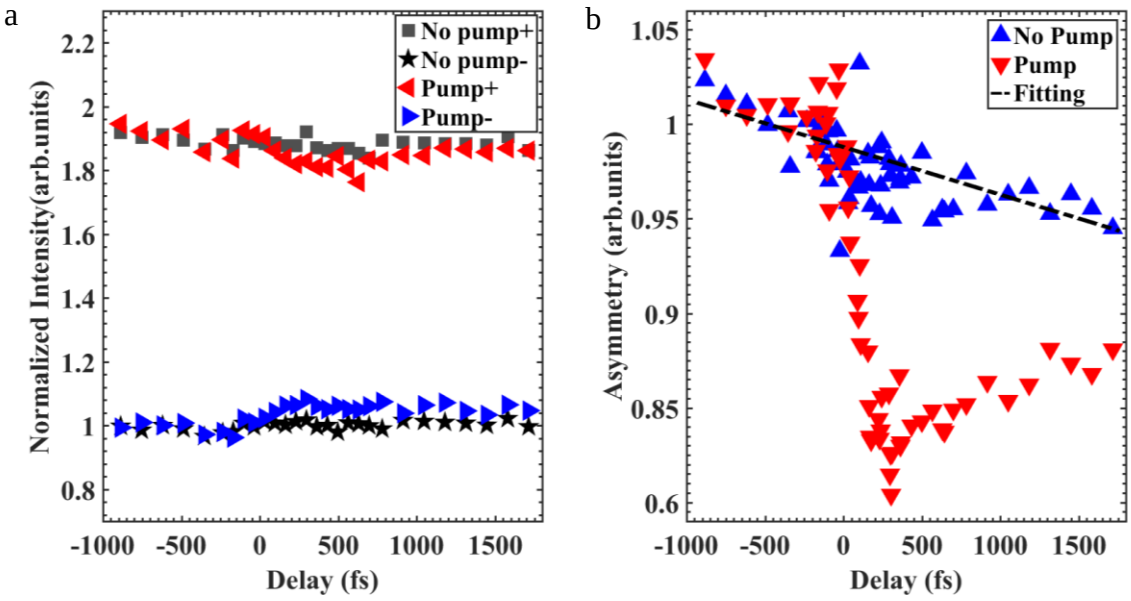

Figure 4.5: (a) Reflectivity of the 10 nm Ni sample measured a photon energy of 66.7 eV, in resonance with the $M_{2,3}$ absorption edges of Ni as the function of time delay (-500 to 1000fs) in four different configurations: positive (red, up triangles), and negative magnetic field (blue, down triangles)

with pump laser, positive (gray, square), and negative magnetic field (black, pentagram) no pump laser. (b) The asymmetry calculated from these four curves for pumped (red, hexagram) and unpumped (blue, circle) configurations.

4.1.4 Comparison between Ni and Py

We have performed the same measurements on the Ni and Py samples. Figure 4.6 shows the comparison between the magnetization dynamics of these two samples. For both samples we observe a demagnetization followed by a partial recovery. The Ni sample demagnetizes a bit more probably due to the combine effects (i) a higher absorption at this resonant photon energy due to a higher Ni content and (ii) a lower Curie temperature of pure Ni compared to the Py alloy (Fe Curie temperature being much higher than that of Ni). We also observe that Py demagnetizes somewhat faster than Ni.

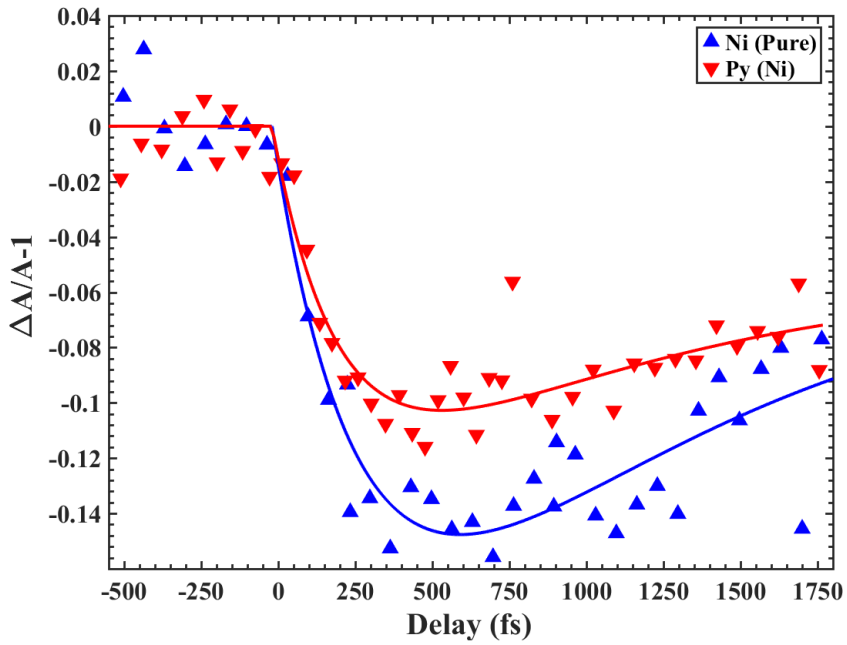

Figure 4.6: Time-dependent demagnetization dynamics curves for both Py and Ni samples. The normalize magnetic asymmetry (A) is both measured in the $M_{2,3}$ absorption edges of Ni ($h\upsilon$ = 66.7 ± 0.1 eV) as the function of time delay (red square Ni and blue square Py**.**

To shed further light on the experimental findings and to estimate the demagnetization time quantitatively, the experimental data was fitted to the data calculated using the three-temperature model, which expresses the magnetization change as [89]:

$$\frac{\Delta A}{A} = \left\{ A_1 - \frac{\left(A_2\tau_E - A_1\tau_M\right)\cdot e^{-\frac{t}{\tau_M}}}{\tau_E - \tau_M} - \frac{\tau_E(A_2 - A_1)\cdot e^{-\frac{t}{\tau_M}}}{\tau_E - \tau_M} \right\} H(t)\times\Gamma(t) \qquad (45)$$

where the H(t) is the Heaviside step function and τ_E and τ_M are, respectively, the electrons-phonons thermalization time and the relaxation time from spins. A_1 represents the equilibrium temperature parameter and A_2 represents the initial electron temperature rise and r(t) is the FEL pulse envelope determining the temporal resolution.

Elements	**(M-1) $_{min}$**	**τ_M (fs)**	**τ_E (fs)**	**A_1**	**A_2**
Py (Ni)	12.7%	180 ± 40	1100 ± 200	0.03 ± 0.005	0.12 ± 0.02
Ni	17.3%	140 ± 30	1100 ± 200	0.01 ± 0.005	0.20 ± 0.02

Table 4-1: Ultrafast demagnetization fitting parameter of Py (Ni) and Ni.

The fitting results of this semi-empirical model are present in the table 4-1. The demagnetization time found for Ni (140 ± 30 fs) is slightly shorter than that found for Py (180 ± 30 fs) but within the error bar of our measurement, this cannot be completely ascertained. Our results are in line with previous infrared pump study [37] and with the study by Radu [88], although in their case the sample demagnetize more.

4.1.5 Demagnetization time as function of pump fluence

FEL pump is questioned by its laser fluence distribution; nonetheless this unique property allows us to acquire more specific data from the variance of the pump fluence. The advantage of XFEL pump result is to unprecedentedly provide the ability to separate the pump-dependent curves with different pump fluence, which is difficult to be realized by using infrared pump.

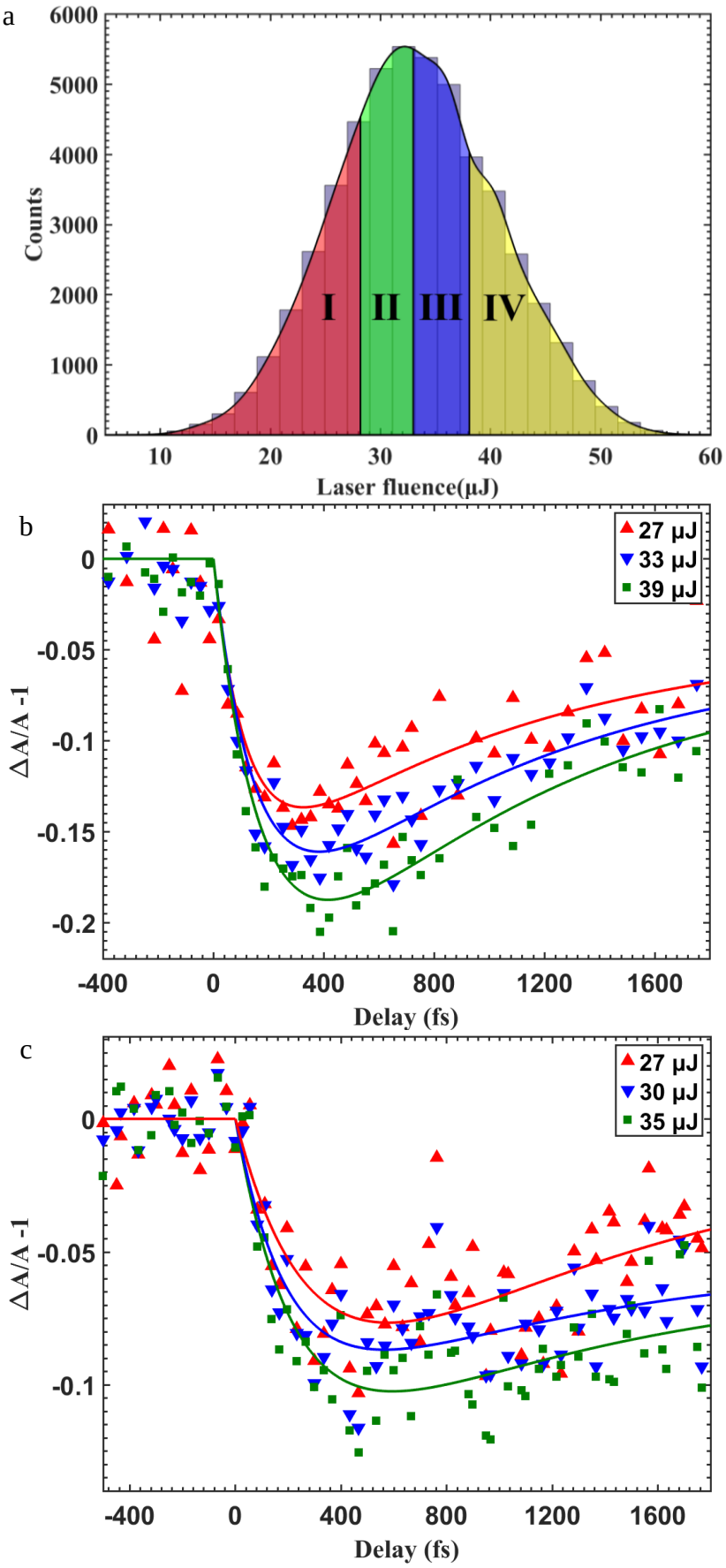

Figure 4.7: (a) Pulse intensity distribution of all the pump – probe events recorded to plot the Ni

demagnetization curve.(b) Ni and (c) Py demagnetization curves for three different pump fluence obtained by sorting the pump – probe events by intensity.

In more details, in each delay scans we have 56 delays for which we record 900 shots each. After sorting the pulse fluence from the low to high value for each delay scan, we divided them into three groups (see figure 4.7 (a)): (i) low fluence, region I+II; (ii) average fluence, region II+III; (iii) high fluence, region III+IV. The purpose of the overlap is to obtain as many events in each group to have the same statistic. The results are plotted in figure 4.7 (b) and (c), respectively for Ni and Py. As expected, we now obtain three distinct demagnetization curves with increasing magnetization loss. Interestingly, the statistics remains very good and the curves are of fairly good quality. The curves have been fitted by the same expression than before and we have extracted the maximum magnetization loss and demagnetization time τ_M. The demagnetization times obtained have been compared to previous work in figure 4.5 (a). Within, the error margin of our measurement the demagnetization time does not increase significantly with the maximum loss of magnetization. It would be interesting to see if this holds for higher fluence since there seem to be a contradiction on this point between IR and XUV probe: with the IR probe an increase demagnetization time is observed while with the XUV probe the demagnetization time remains constant with pump fluence [90]. Unfortunately, it was not possible to increase the pulse intensity over about 50 μJ for this experiment and hence the demagnetization range was limited. Figure 4.7 (b) shows that the number of intensity groups can be increased to eight while conserving a statistic good enough to fit the data and extract information. For example, we see that in the fluence range explore the maximum magnetization loss is proportional to the pump fluence.

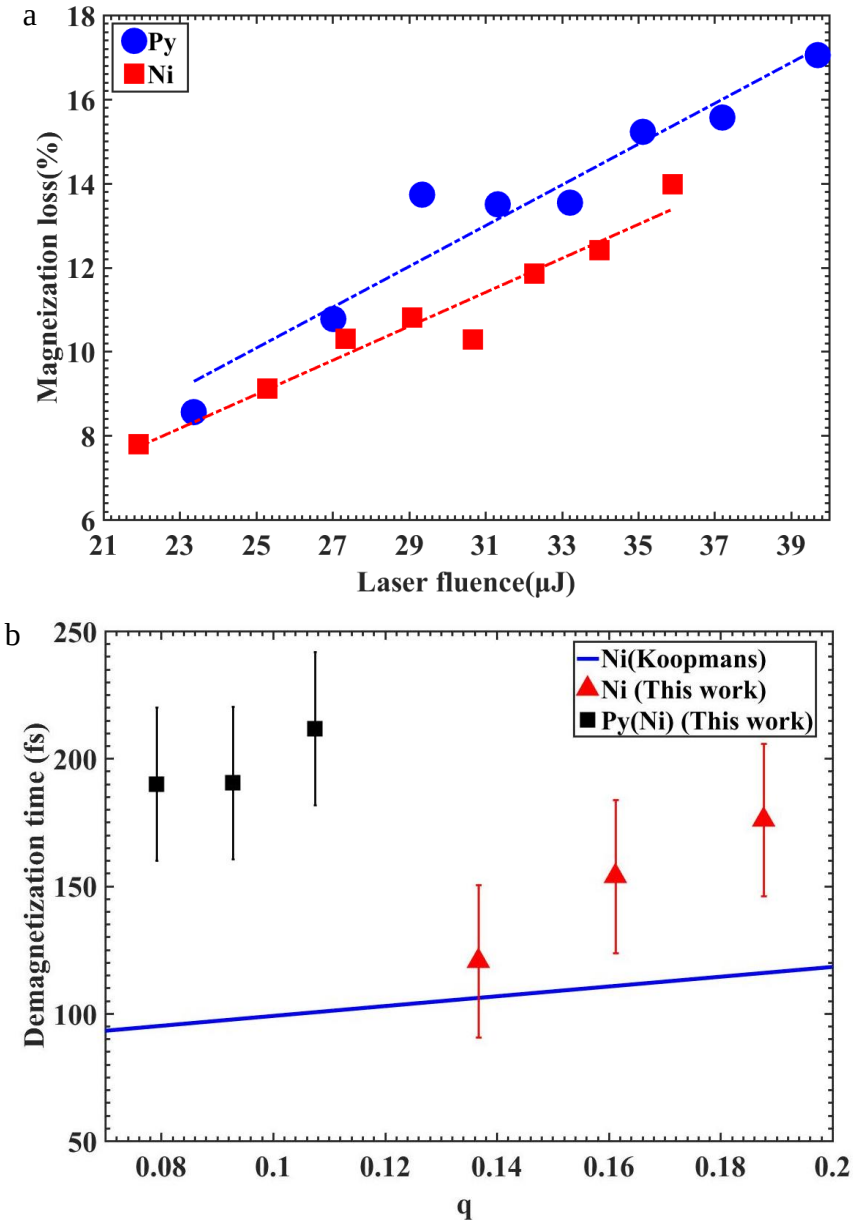

Figure 4.8: (a) Demagnetization times, τ_M, as function of magnetization loss for Ni (red triangles) and Py (black squares). (b) Evolution of the magnetization loss (q) as function of pulse intensity obtained by grouping the pulse intensity in three bins. We can see that for the intensity explored we remain in the linear regime. The blue line is taken from Koopmans *et al.* [37].

4.2 Transmission geometry

4.2.1 Introduction

The first experiments in reflection, we conducted experiments in transmission geometry. Since the XUV pulses at FLASH 2 are linearly polarized, we cannot use the x-ray magnetic circular dichroism which is the preferred technique to probe magnetization in transmission [91][92]. We have then used the Faraday Effect. How this effect can be used to probe magnetization was explained in chapter 3. The configuration of the experiment is similar to that of the reflection geometry up to the sample. In this experiment, we have studied 30 nm thick Py and Ni samples. Both films were sputter deposited on chips consisting of a nine by nine grid of 50 nm thick Si_3N_4 windows. The windows are squares of 200 µm, 100 µm or 50 µm. The samples have been capped by a 5 nm Al layer to prevent them to be oxidized.

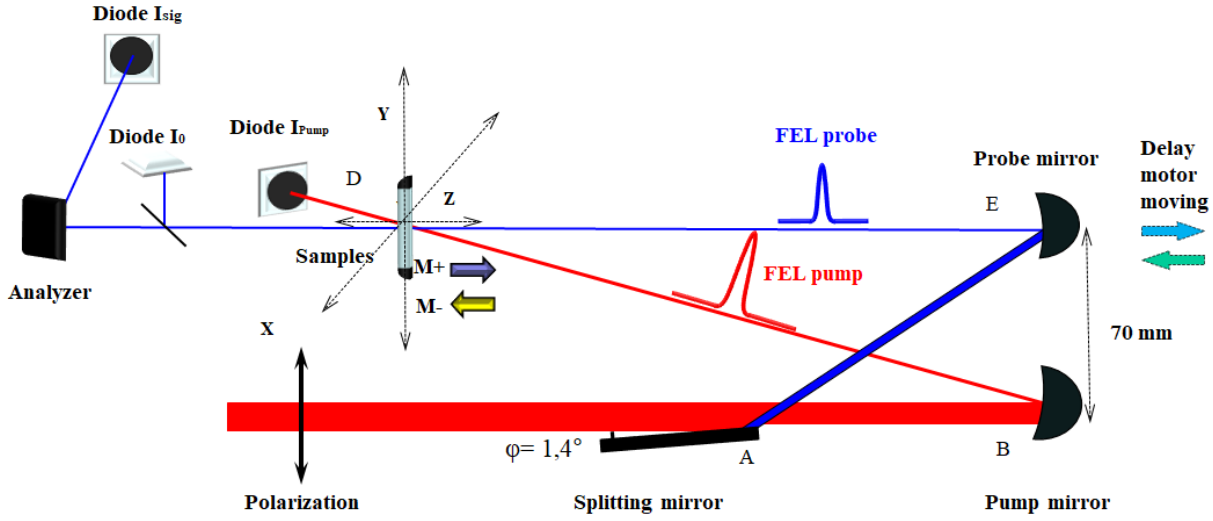

Figure 4.9: Schematic diagram of the transmission setup showing, in addition to the split and delay unit, the out of plane magnetization of the sample (purple and yellow arrow), the intensity monitor for pump (diode 2) and for probe (diode 3), the analyzer (wide band multilayer) and the signal detector (diode 1).

Indeed, in transmission geometry (see figure 4.9), the sample is set at a near normal incidence and magnetized out of plane by permanent ring magnets (maximum field of 3500 Gauss) in order to maximize the Faraday Effect. To reverse the direction of the magnetic field, we use two sets of magnets mounted in opposite direction on a motorized stage. After the sample, the pump and probe beam diverge. The pump beam intensity is recorded on an XUV

photodiode. Part of the probe beam is reflected up (s-geometry) by a Si_3N_4 window and recorded by an APD. This allows us to record the probe beam intensity: indeed, being placed in s-geometry, this reflection is mostly unaffected by the magnetic state of the sample. The fact that the I0 monitors for pump and probe are placed after the sample give a higher precision since only the intensity going through the sample is measured.

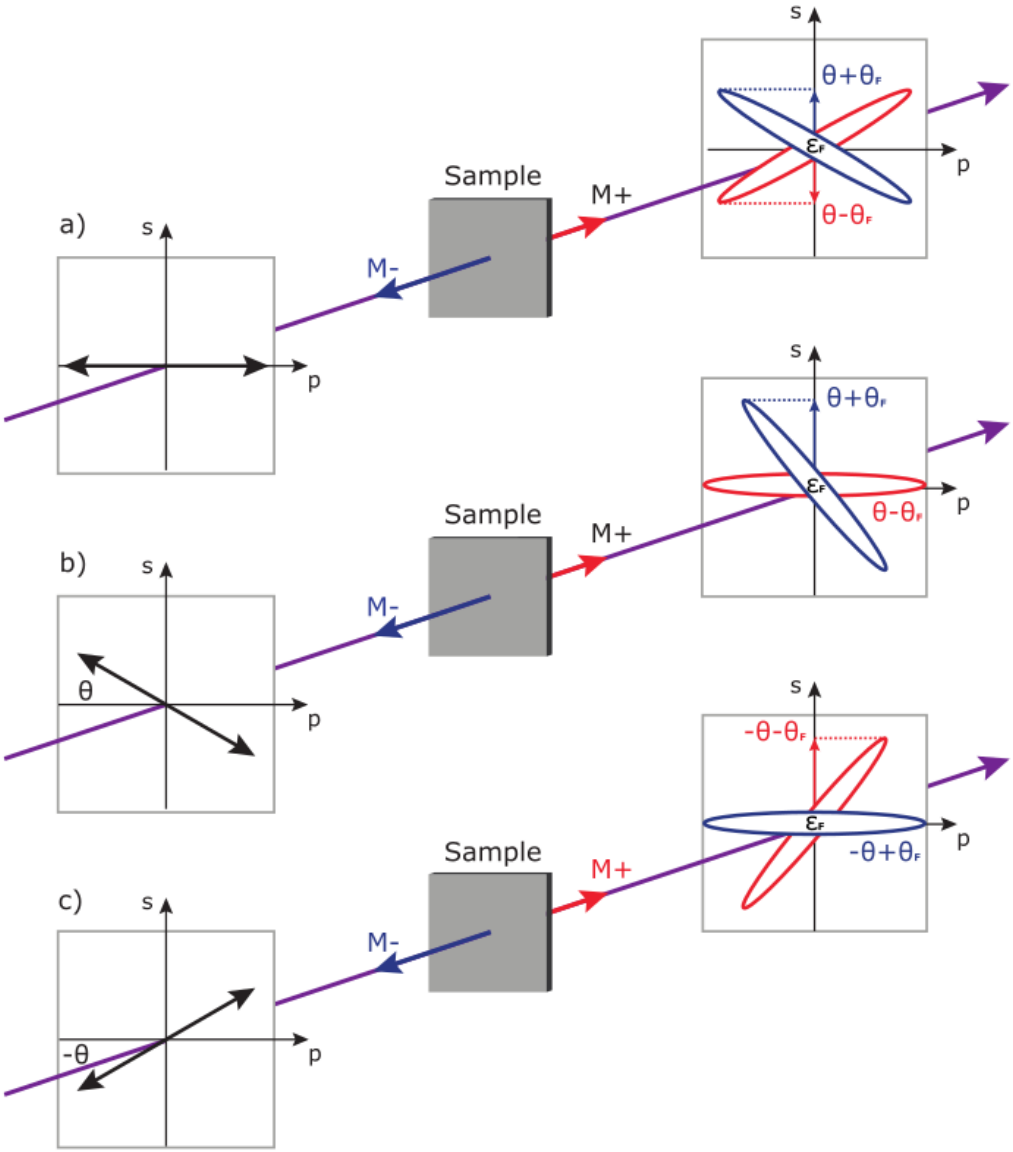

Figure 4.10: Illustration of the faraday effect. Faraday rotation angle (θ_F) and ellipticity (ε_F) introduced in the incident polarization passing through a magnetized sample for two opposite magnetization directions, with the polarization angle of the incident light: (a) parallel to the p direction, (b) equal to θ, and (c) equal to – θ.

After the normalization window, the probe beam is reflected by the analyzer, a multilayer mirror which mostly reflects the s-component of the FEL pulses, and its intensity is

measured by an APD. The angle of incidence on the analyzer can be adjusted to optimize the amplitude of the Faraday Effect. The analyzer can also be rotated around the probe beam axis in order to move the reflection out of the horizontal plane. This allows us to work slightly out of the p-geometry which is essential to be able to see a difference between the two direction of magnetization (see figure 4.10). Indeed, since the analyzer and detector are only sensitive to the magnitude of s-component of the beam, both direction of magnetization give the same signal in pure p-geometry. Working slightly out of the horizontal plane results in different signal for the two different magnetization direction (see figure 4.10).

Depending on the photon energy used, we can conduct two different time resolved Faraday measurements. When the Faraday Effect is dominated by the rotation, $\Delta\delta$ high (see figure 4.11, taken from [93] for $\Delta\delta$ and $\Delta\beta$ values around the Fe and Ni M edges), the asymmetry (same definition as in T-MOKE) is somewhat proportional to the magnetization. However, when the Faraday Effect is dominated by the ellipticity, $\Delta\delta$ close to zero (see figure 4.11), the asymmetry vanishes. In that case, the magnetization can be retrieved by divided the pump signal by the unpumped signal for any of the two magnetization directions. By plotting the static signal obtained for the two opposite magnetization directions (see figure 4.12), we have chosen the following energies to conduct our experiments: 64.7 eV and 66.9 eV for Ni which respectively maximize the rotation and ellipticity, and 53.6 eV which maximized the rotation for Fe. We did not have time to measure at the photon energy for Fe.

In addition to the present of pump diode, it allows us counting pump pulse for each shot. In this case, we can extract fluence dependent demagnetization curves by sorting and choosing different pump pulse intensity. However, from the result fitting, we found there are slightly variations of demagnetization time for Ni and Py samples with different pump fluence. In particular, by using an XUV probe with energy of 64.7 eV and 66.9 eV, we observed completely different demagnetization behavior for both of Ni and Py samples, which has been never observed and reported before. Furthermore, our measurements conclusively show that when we using 64.7 eV respectively to probe pure Ni sample and Py sample, a 60 fs onset is appeared perhaps due to the strong exchange coupling between Ni and Fe. Then if probing Py with 53.6 eV, the result shows that demagnetization of Fe reacts faster than that of Ni in alloy (using 64.7 eV). Finally, by comparing the result of pure Ni and Py samples from spilt and delay T-MOKE with spilt and delay Faraday Effect with the almost same photon energy (around 66.8 eV), we show identical process for the demagnetized to the maximum. Thus, in this experiment, probing photon energy is sensitive to or even able to influence the demagnetization time in Ni and Py.

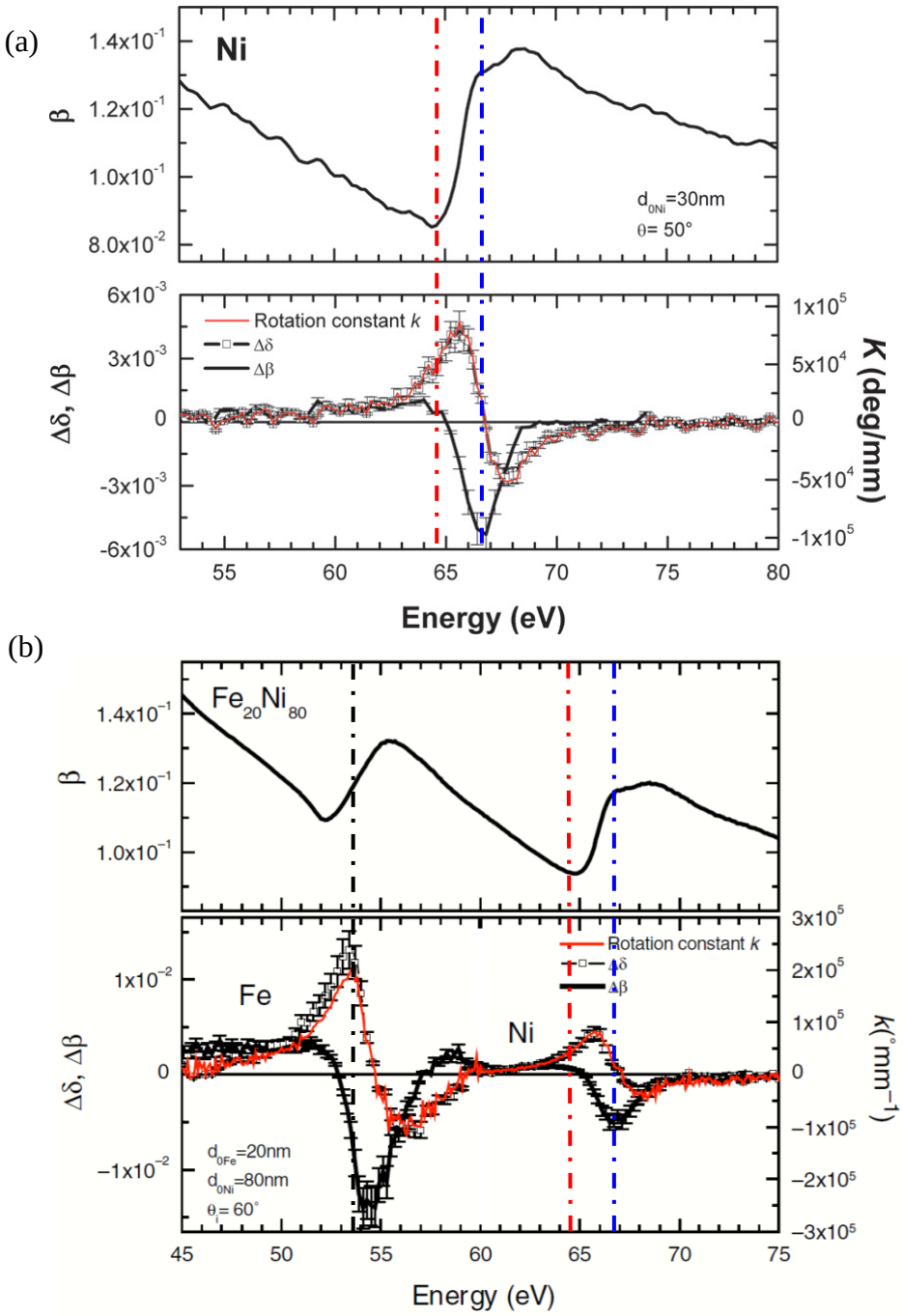

Figure 4.11: Magneto optical constant as function of photon energy for (a) Ni and (b) Py measured around the Ni and Fe M edges [93]. The red dash line is 64.7eV and the blue dash line is 66.9 eV and the black dash is 53.7eV.Pure Ni (a) and Py (b).

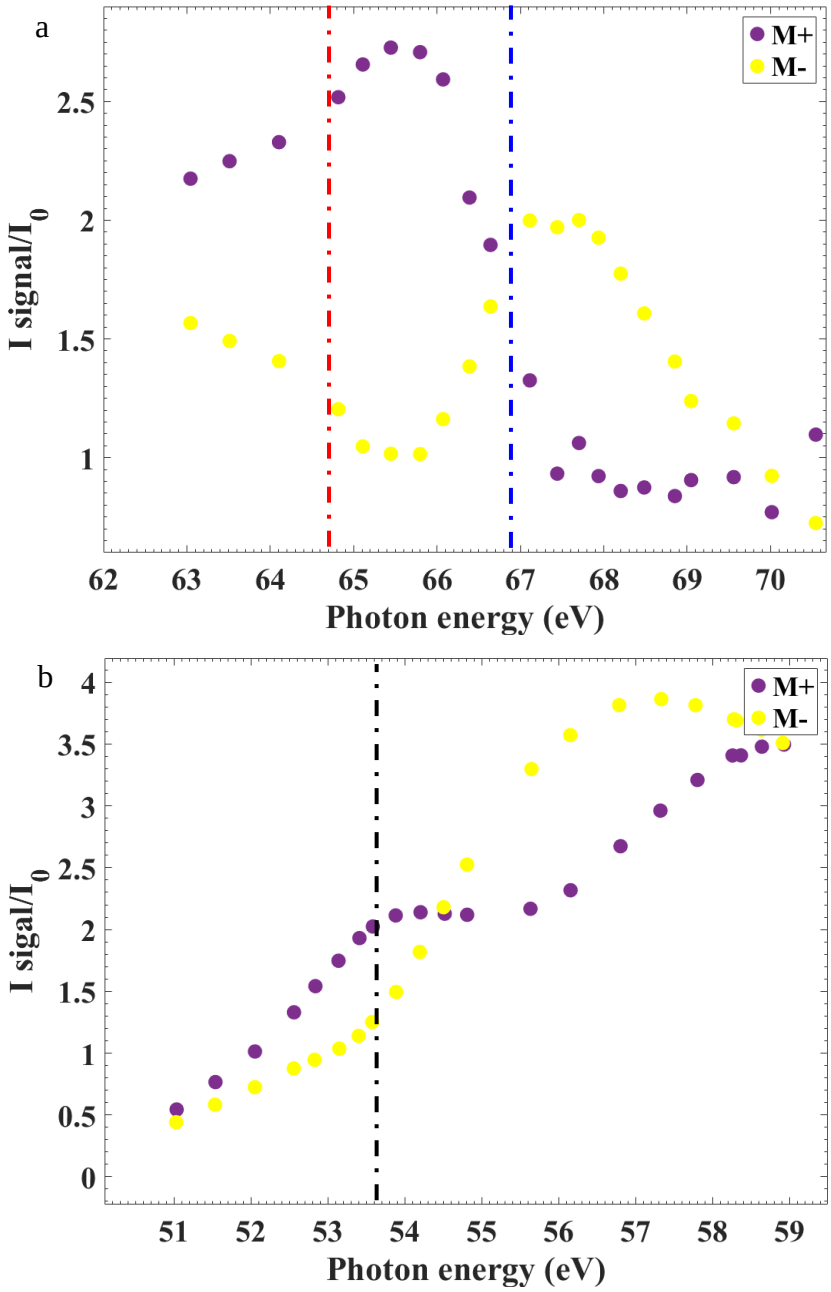

Figure 4.12: Normalized signal after our analyzer as a function of photon energy recorded for (a) the Ni sample at the Ni M edges and for (b) the Py sample at the Fe M edges. The signal for positive (violet) and negative (yellow) magnetization have been recorded. When the curves for opposite direction crossed the Faraday rotation, Δδ, vanishes (66.9 eV for Ni, blue dashed line). On the contrary the rotation, Δδ, is maximized when the ratio of the two curves reach maximum (64.7 eV for Ni, red dashed line, and 53.6 eV for Fe, black dashed line).

Finally, it has to be noted that the quality of all optics was increased for the transmission experiment. In particular, we used higher reflectivity multilayer coatings. This allowed us to use very short pulses (below 10 fs), which come with a reduced intensity (lower

than 10 μJ), while still being able to pump the samples. We can then estimate a total time resolution of about 10 fs for this experiment, probably one of the best ever for magnetization dynamics experiment.

4.2.2 Measurements and interpretation

First, we measured the Ni and Py sample at photon energy of 64.7 eV (see figure 4.13 and 4.14). At this energy, we are mostly sensitive to the phase shift, Δδ. As described earlier, we sorted the pulses by intensity to be able to plot demagnetization curves for different pump fluence. We suffer from some FEL instabilities which gave rise to a two lobes intensity distribution (most probably due to an oscillatory motion of the beam).

The data are sorted by low (green), average (blue) and high (red) pump fluence. In both cases, Ni and Py, the maximum demagnetization scales linearly with the pump fluence. The signal to noise ratio, especially for the Ni curves, is very high, even after having sorted and grouped the events, i.e. after reducing the number of events by three. This demonstrates the very high potential of this technique.

The data have been fitted by equation 45. Since the range of delays that we could explore was limited (due to time constraints), the fit parameters are not very accurate even though curves we obtained are in very good agreement with the data points. To extract meaningful data from these fitted curves, we then calculated the time for which the demagnetization reaches 63% ($1 - e^{-1}$) of its maximum. These values are reported in Table 4-2. The demagnetization time for Ni ranges from 142 to 166 fs and from 186 to 199 fs for Py.

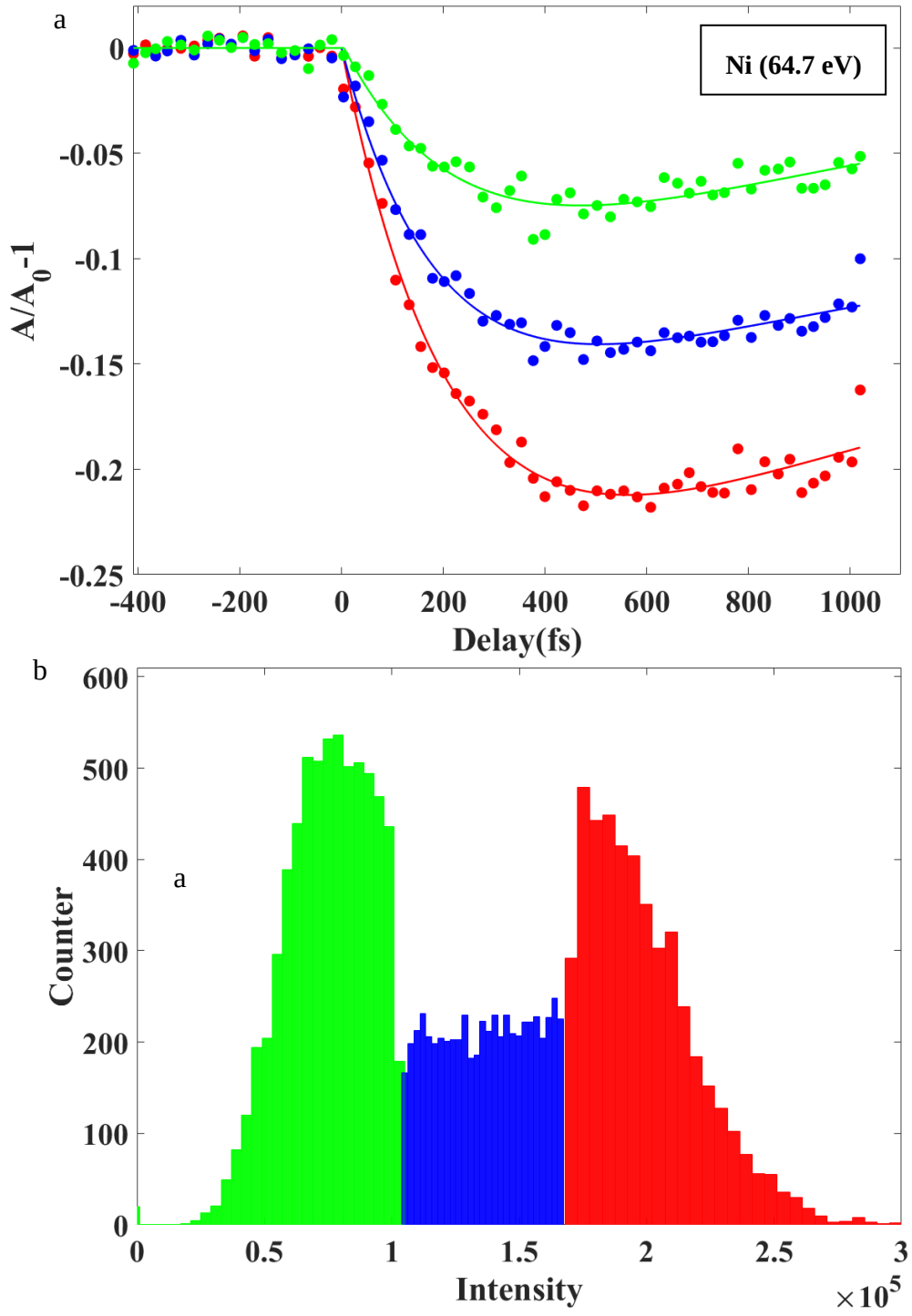

Figure 4.13: (a) Pulse intensity distribution obtained during a delay scan on Ni sample. The intensity have been sorted and grouped in low (green), average (blue) and high (red) pump fluence. (b) Demagnetization curves of Ni sample obtained for this three pump fluences.

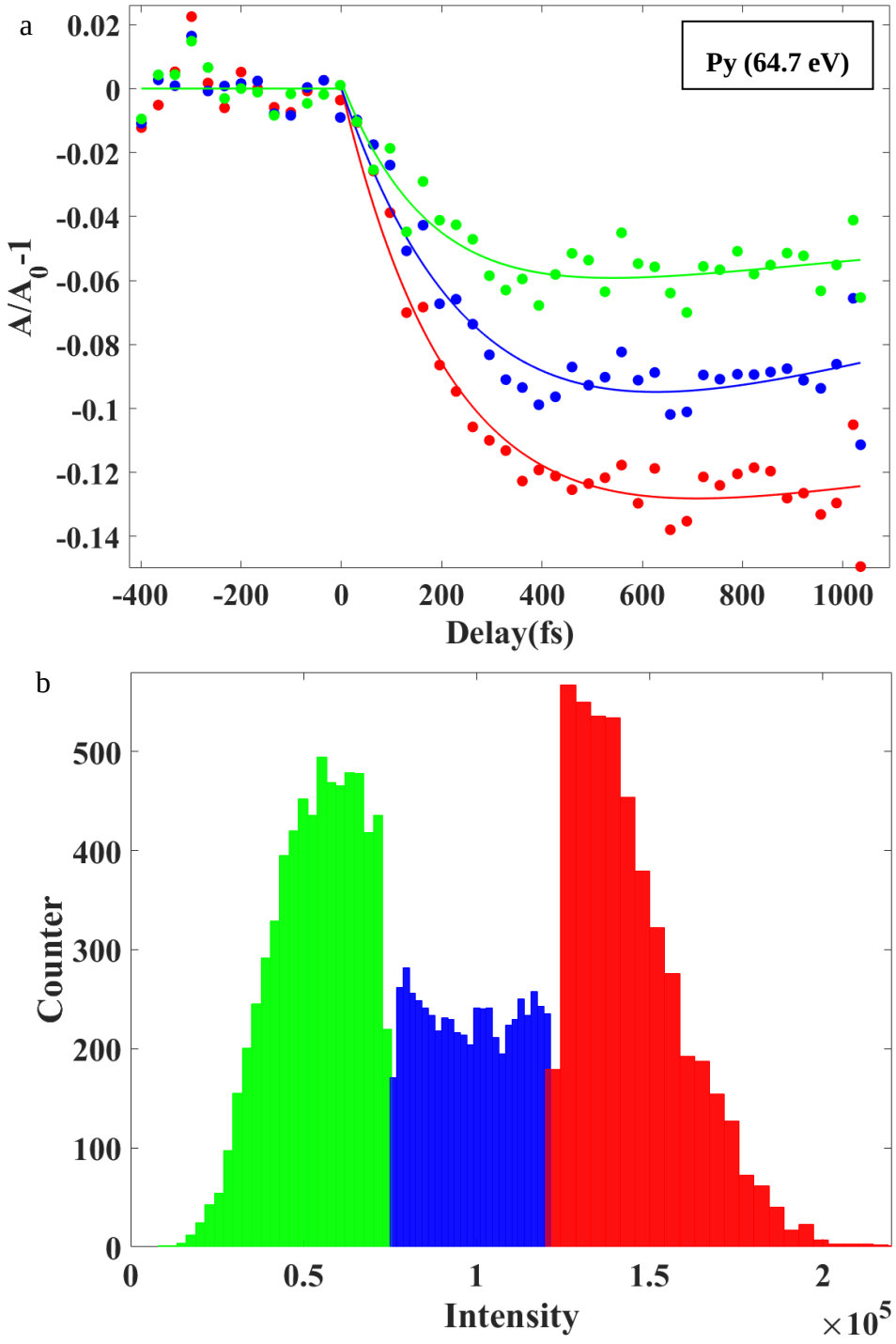

Figure 4.14: (a) Pulse intensity distribution obtained during a delay scan on Py sample. The intensity have been sorted and grouped in low (green), average (blue) and high (red) pump fluence. (b) Demagnetization curves of Py sample obtained for this three pump fluences.

Sample (64.7 eV)	**$(M-1)_{min}$**	**τ_M (fs)**
Ni (Green)	7.3%	142 ± 10
Ni (Blue)	14.1%	160 ± 10
Ni (Red)	21.1%	166 ± 10
Py (Green)	5.3%	186 ± 20
Py (Blue)	9.0%	199 ± 30
Py (Red)	12.4%	188 ± 20

Table 4-2: Fitting result of 30 nm Ni and 30 nm Py by probing with the photon energy of 64.7eV, $(M-1)_{min}$ represents the maximum demagnetization.

The demagnetization time of Ni is then slightly lower than that of Py and this can be confirmed by plotting simultaneously demagnetization curves from the two samples on the same graph (see figure 4.15 (a)). We sorted the pump – probe events in order to obtain the same degree of demagnetization (~9%) for the two samples. The Py sample clearly appears to lag behind the Ni sample.

Furthermore, one of the goals of our experiment was to compare the dynamics of Ni and Fe in Py. We then also measured the magnetization dynamics of the Py sample at photon energy of 53.6 eV corresponding to the maximum Faraday rotation before the Fe M edges (see figure 4.11 (b)).

Figure 4.15 (b) shows the comparison between the curves obtained at 53.6 and 64.7 eV on the Py sample. The pump – probe events have been sorted in order to obtain a similar degree of demagnetization. This is particularly important in that case since the absorption of the Py is not the same at these two energies (although the variation remains limited to less than 10%). One can observed that the dynamics appears clearly faster at the Ni edge than at the Fe edge. Although the delay range does not really permit to see the lower point of demagnetization at 53.6 eV, we have estimated a demagnetization of at least 230 ± 15 fs compared to 180 ± 10 fs at 64.7 eV. However, within the accuracy of our measurements, there is no delay between the dynamics at the two energies. Our results are more in line with the report by Radu *et al.* [88].

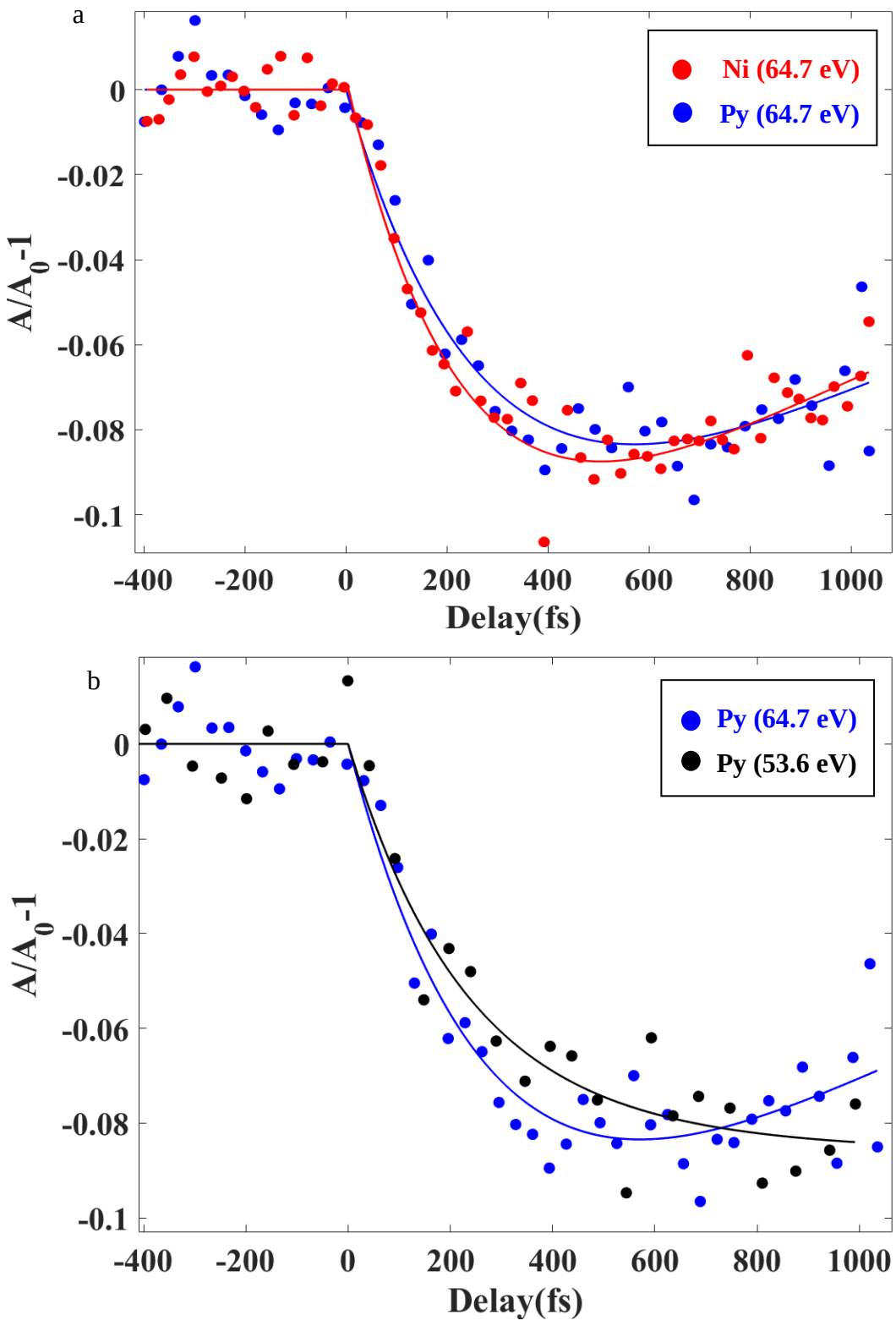

Figure 4.15: Element-specific demagnetization dynamics of the constituent magnetic moments in Py ($Ni_{80}Fe_{20}$) and pure Ni measured by Faraday Effect (a) and Py (b) the comparison of similar degree of demagnetization by choosing certain range of pump intensity.

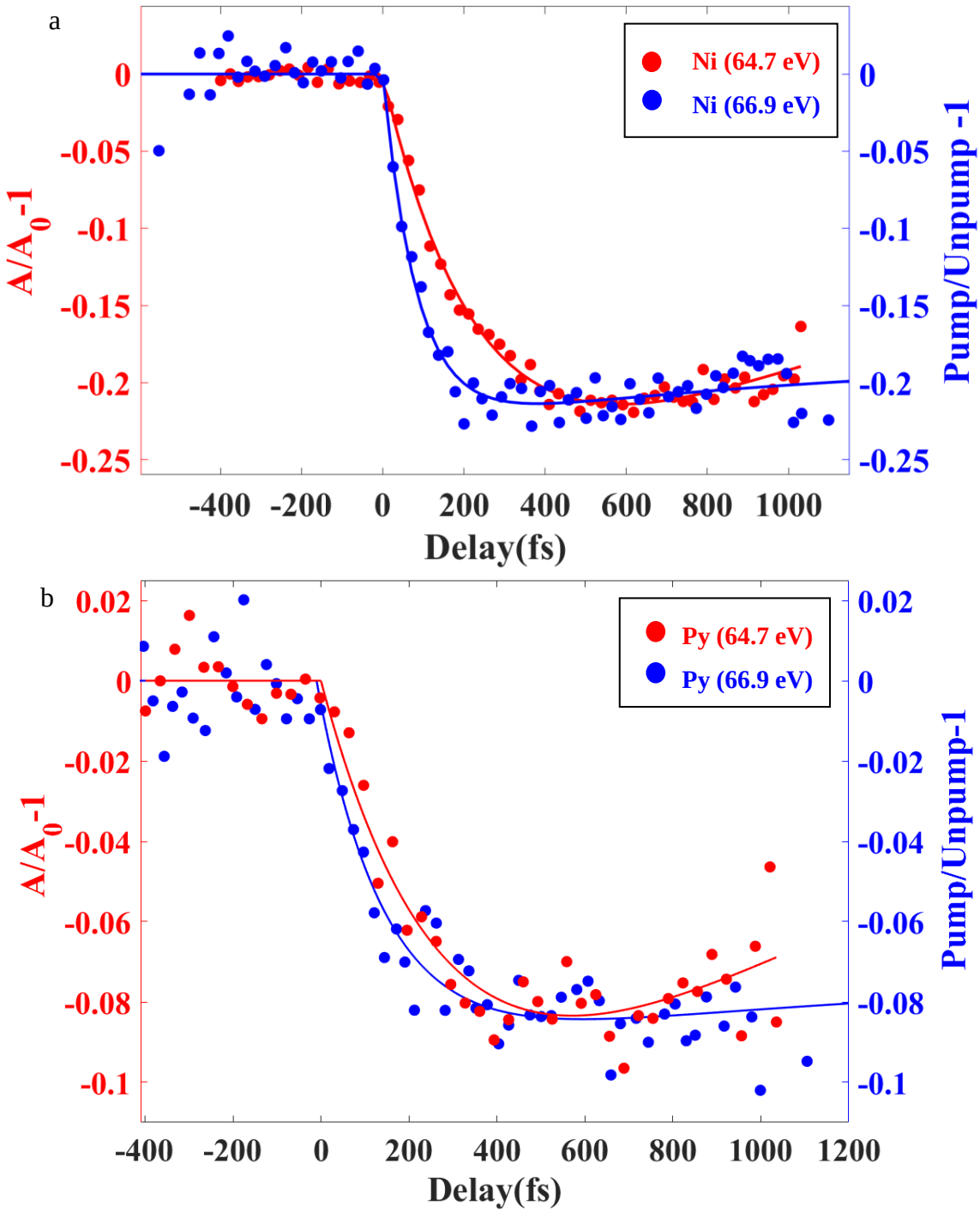

Figure 4.16: Comparison of the magnetization dynamics curves obtained for two different photon energy 64.7 eV and 66.9 eV around the Ni M edges for (a) Ni and (b) Py samples.

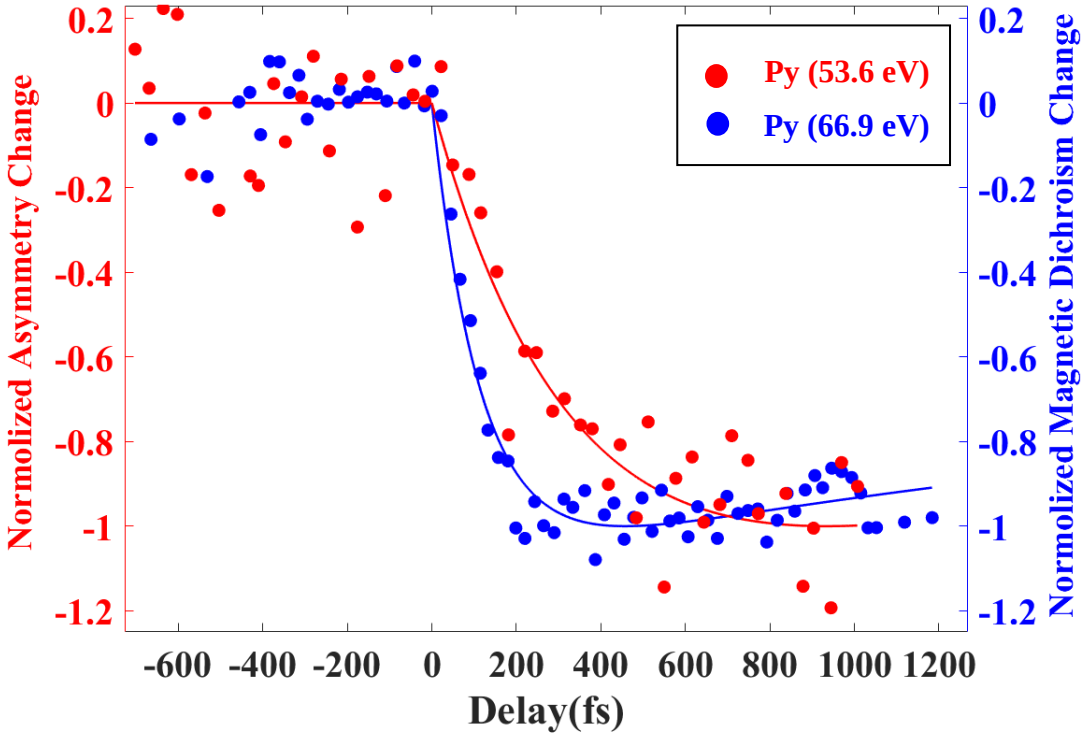

Figure 4.17: Comparison of the magnetization dynamics curves obtained for two different photon energy 53.6 eV (Fe edge) and 66.9 eV (Ni edge) for Py sample.

To ascertain the fact that the different behavior observed at 53.6 eV and 64.7 are due to different behavior of the Fe and Ni sub-lattices, we measured the magnetization dynamic of the Py sample at 66.9 eV. This energy is in resonance with the Ni M edges but maximizes the Faraday ellipticity instead of the rotation. Mostly, we are then only sensitive to Δβ and are very close to a classical XMCD measurement where only Δβ is measured.

Figure 4.16 shows the comparison between 64.7 and 66.9 eV for both Ni and Py samples. The dynamics measured at the 66.9 eV are clearly faster than the on measured at 64.7 eV: demagnetization time of 124 ± 10 fs compared to 179 ± 10 fs for Ni and 96 ± 10 fs compared to 168 ± 10 fs for Py. This effect has not been reported so far and shows that the probe energy is of very high importance. It could explain the discrepancies between Mathias *et al* [94] and Radu *et al* [88] measurements but also between XUV and visible probe. In this regard, it is interesting to note that comparing 53.6 eV to 66.9 eV yields very important difference in the dynamics (see figure 4.17). Unfortunately we did not have time to measure at ellipticity dominated energy around the Fe M edges (54.5 eV) to confirm the existence of this effect for another absorption edge. We have no clear indication yet to explain the origin of this effect. In any case, a complete study of these two absorption edges (several photon energy around each edges), and maybe that of cobalt (around 60 eV), will be necessary to

obtain a complete view of this phenomenon. It could help us to revisit earlier work discussing the relevance of magneto-optic on the ultrafast timescale [83] or the potential influence of electronic structure dynamics on magnetic dynamics [95].

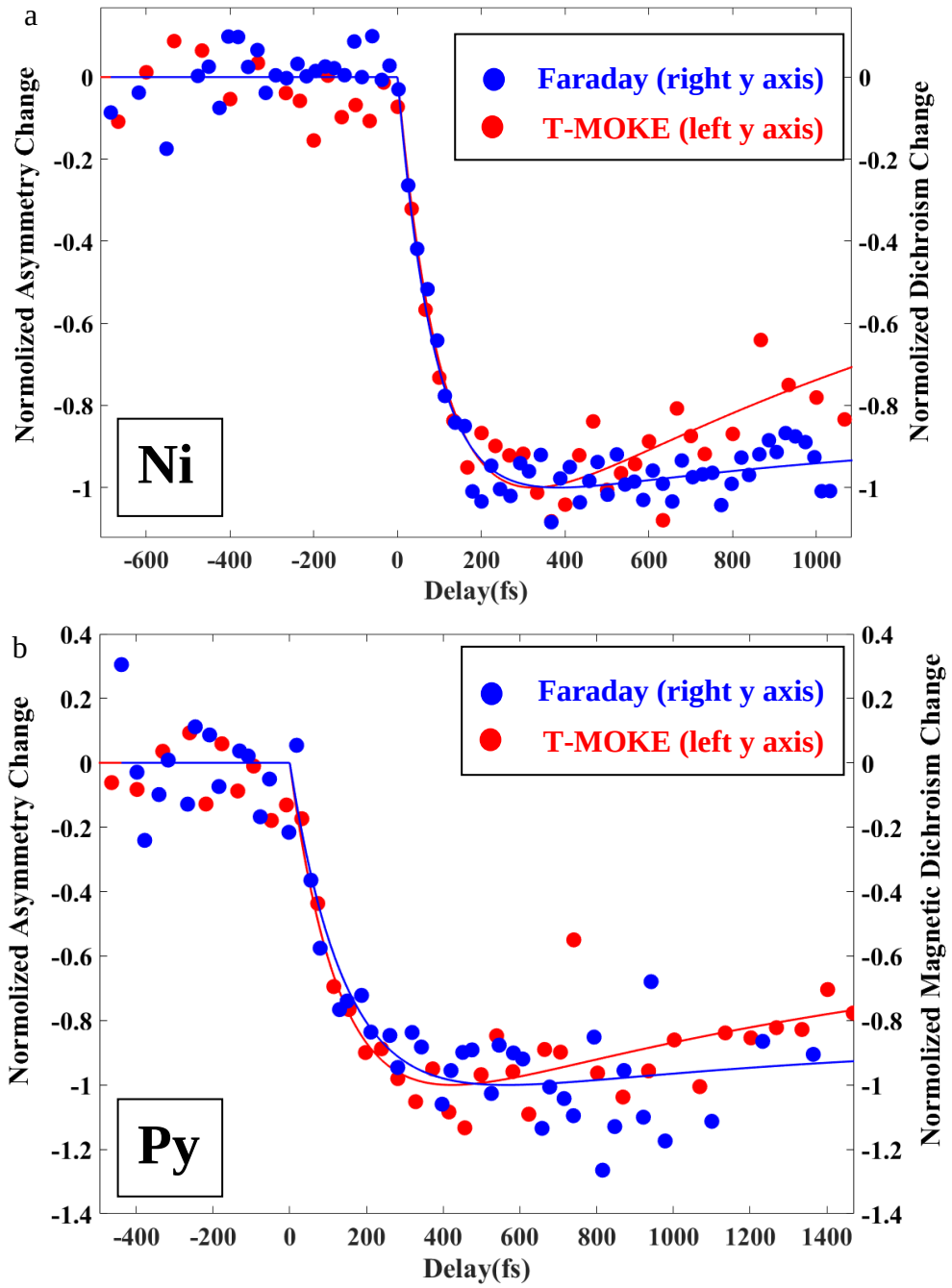

Figure 4.18: comparison of ultrafast MO response measured by the geometry of reflectivity (T-MOKE) and of transmission (Faraday Effect) for Ni (a) and Py (b)

Finally, we compared the measurements done in transmission at 66.9 eV to the one done at 66.7 eV in reflection for Ni and Py (see figure 4.18). Considering that the samples studied were not the same (in particular the thickness are 30 and 10 nm), the curves obtained are remarkably similar once scale to the same degree of demagnetization. The shorter recovery time for the reflection geometry could be explained by the fact that the reflection samples are grown directly on highly electronic and heat conductive silicon rather than poorly conductive Si_3N_4.

4.2.3 Conclusion and perspectives

In summary, we have shown that laser-induced ultrafast demagnetization of Ni and Py thin films realized on the new built split and delay device with transmission geometry. We also have showed that our setup has an excellent performance with time resolution around 10 fs. By using three different probing energy 64.7 eV, 66.9 eV, and 53.7 eV, it is the first time that we observed the different demagnetization curves that obtained at the energy a little before (64.7 eV) and a little after (66.9 eV) M absorption edge of Nickel for pure Ni and Py samples. Then we have compared the dynamics of the demagnetization of Fe (53.7 eV) and of Ni (64.7 eV) in Py sample, the results show that Fe demagnetizes slower that Ni and at 64.7eV, Ni in Py demagnetizes slower than Ni in Pure Ni. At last, at the 66.9 eV, we have compared the results of T-MOKE and Faraday Effect; we observed similar curves both for Ni and Py in the period of demagnetization.

The next step, we will continue to investigate the ultrafast demagnetization of Fe and we will also compare the curves at 53.7 eV and 54.6 eV for Py. In addition, we will investigate the different component of Fe and Ni alloy, for example: $Fe_{80}Ni_{20}$ and $Fe_{50}Ni_{50}$, the different ratio of Ni and Fe allows us to study how strong the exchange coupling can influence the behavior of demagnetization.

5 Chapter 5: Terahertz Pump and Ultrafast Coherent Magnetization Control

5.1 Introduction

One of the main drives for ultrafast magnetization dynamics studies is applications in magnetic storage technology and logic operations with spintronic devices [96]. For example, it would be very appealing to break the nanosecond limit for magnetization manipulation to create ultrafast magnetic device for Big Data or Artificial Intelligence. To achieve this goal, it is not sufficient to only demagnetize a system; we need to completely control its magnetization. In that regard, the experiment realized by Vicario *et al.* [97] is very interesting. By using a THz pump, they were able to initiate non resonant precession of the magnetization in a thin cobalt film (see figure 5.1). This observation opens up the way to the deterministic control of magnetization with ultrashort pulses.

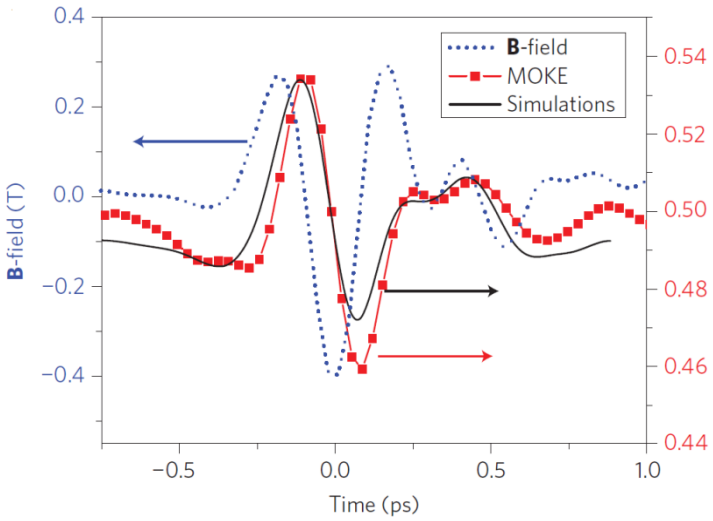

Figure 5.1: Experimental observation of an ultrafast coherent magnetization control by THz pump. The measurement was performed with Time-resolved magneto-optical Kerr effect (MOKE) geometry, the red curve is the response from MOKE signal, and the blue curve is the magnetic field from THz radiation. The MOKE signal exhibits a variation that is close to identical to the driving terahertz magnetic field. The black curve is the simulation which is based on the LLG equation, which fits well with the magneto-optical response [97].

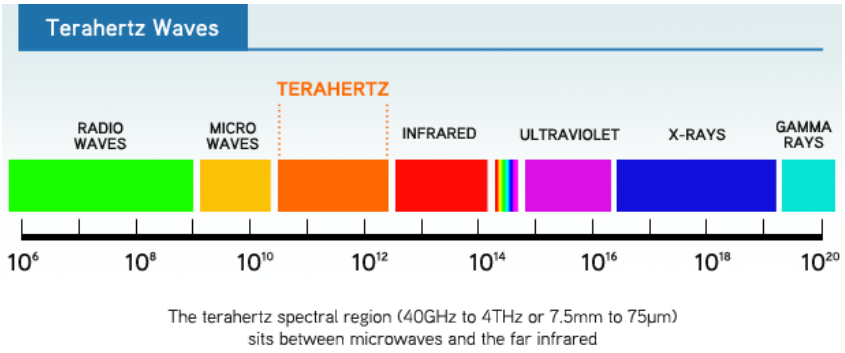

Figure 5.2: The frequency of Terahertz waves [98].

Terahertz pulses have a longer wavelength than IR pulses, hence a lower frequency (see figure 5.2). Consequently, the terahertz photon energy is lower (by almost three orders of magnitude) than that of a near-infrared photon which is generally used as pump in ultrafast magnetization experiments (0.004 eV versus 1.6 eV). Therefore, Terahertz pump excites electrons very close to the Fermi level into lower energy levels IR pump (see Figure 5.3). In this case, the dynamics is dominated by the interaction between the sample and the strong magnetic field of the THz pulse rather than by absorption and heating. It remains to be determining at which wavelength, or over which wavelengths range, we can observe the transition between the two. This knowledge will be fundamental to tailor ultrafast magnetic devices. Our goal is then to study the transition from such a coherent coupling to the non-coherently excited ultrafast demagnetization phenomenon.

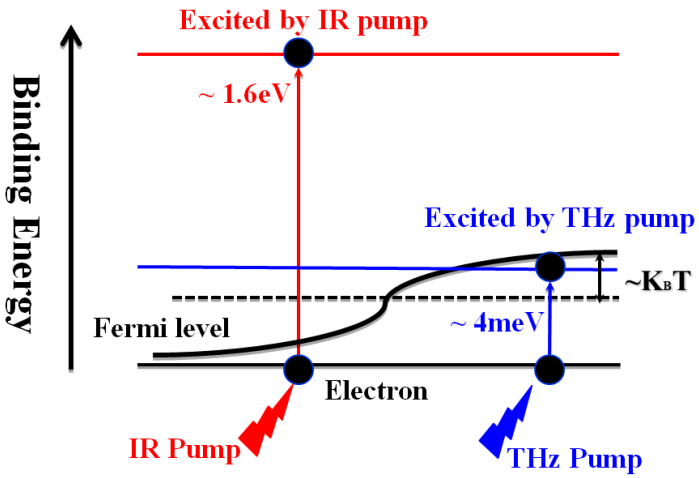

Figure 5.3: The comparison of IR pump and THz pump in terms of energy excitation.

The measurement was performed with Time-resolved magneto-optical Kerr effect (MOKE) geometry, the red curve is the response from MOKE signal, and the blue curve is the magnetic field from THz radiation. The MOKE signal exhibits a variation that is close to identical to the driving terahertz magnetic field. The black curve is the simulation which is based on the LLG equation, which fits well with the magneto-optical response. Comparing with typical ultrafast demagnetization curves by IR pump, terahertz result shows that LLG equation is again available on the ultrafast time scale. A strong motivation turns out that is there a boundary between two totally different phenomena. However, by increasing gradually the wavelength of pump pulse from Terahertz to Infrared range, the boundary is likely to be found. Once we identify the exact excited pump energy, it is possible to calculate the thermal effect triggered by pump pulses and it will be new opportunities for better understanding the ultrafast magnetization dynamics.

However, more recently, the generation of THz pulses with much higher field amplitudes has become possible, which permitted a conceptually new approach for investigating low energy degrees of freedom in matter [99]. Additionally, recent advancements of accelerator technology at FLASH BL3 beamline is enable to produce the carrier-envelope phase stable THz pulses with high fields at adjustable high repetition rates [100]. The appropriate parameters setting from the THz undulator allows generation of tunable THz frequency of narrow-banded and intense pulses, which can be used to excite the magnetic materials with very low energy. THz pulses with pulse energies up to the few 100 μJ regime[101][102]. In present work, we use synchronized THz-pump and with a FEL radiation source to investigate the magnetization dynamics. Tunable THz-undulator allows us to change the pulse duration and the wavelength. Besides, a filter can be added to remove higher order of radiation frequency generated by the undulator. The x-ray free electron laser (XFEL), as a powerful tool for investigating (probing) magnetic phenomena at the nanometer and picosecond scales, is used to study the resonant element-selective magnet-optic response in dynamics at the Ni $M_{2,3}$ absorption edge (66.7eV). Unfortunately, the observed experiment result of did not reveal any ultrafast coherent magnetization control by THz pump. However, after the removal of the filter for the pump laser, its frequency now is composed by mixed wavelength from THz to IR, while an ultrafast demagnetization behavior was appeared. In this case, it allows us to reconstruct the shape of induced electric field of pump pulse as the function of time. This method also provide a new and fast way to identify the electric filed as well as the magnetic field of THz pulse, which will be benefited for THz beamline diagnostics.

5.2 Experimental setup

THz radiation is produced by turning the FIR undulator, which is an especially designed planar electromagnetic undulator with 9 full periods and a period length of 40 cm [103]. It can generate radiation in a very board spectral range from the mid infrared (MIR) to the far infrared (FIR) spectral regions corresponding to wavelengths between 1 μm and 200 μm (respectively 300 THz to 1.5 THz). The pulse duration and intensity depends on the wavelength chosen (see figure 5.4).

Interestingly, the FIR undulator can be operated simultaneously with the XUV undulator for THz pump – XUV probe experiments (see figure 5.5 (a)). To do so, an electrons bunch is accelerated in the tunnel, passes into the first XUV undulator and generates an XUV pulse. The electrons bunch then passes through the FIR undulator and generates a THz pulse. Those two pulses are separated by a holey mirror and then recombine onto the sample. Thanks to a series of mirrors. Since both THz and XUV pulses are emitted from the same electron bunch, they are naturally synchronized [104].

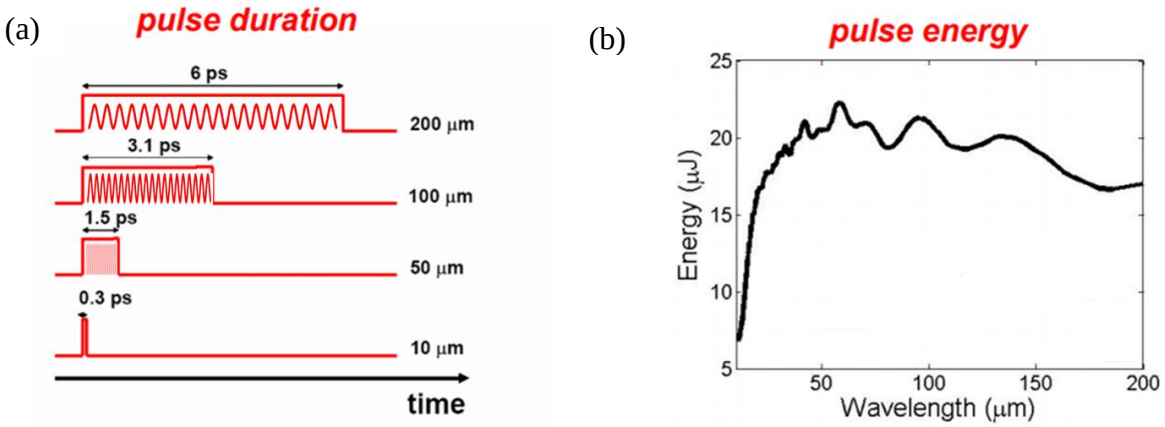

Figure 5.4: Relation between (a) pulse duration and (b) intensity of THz radiation emitted from the FIR undulator [104].

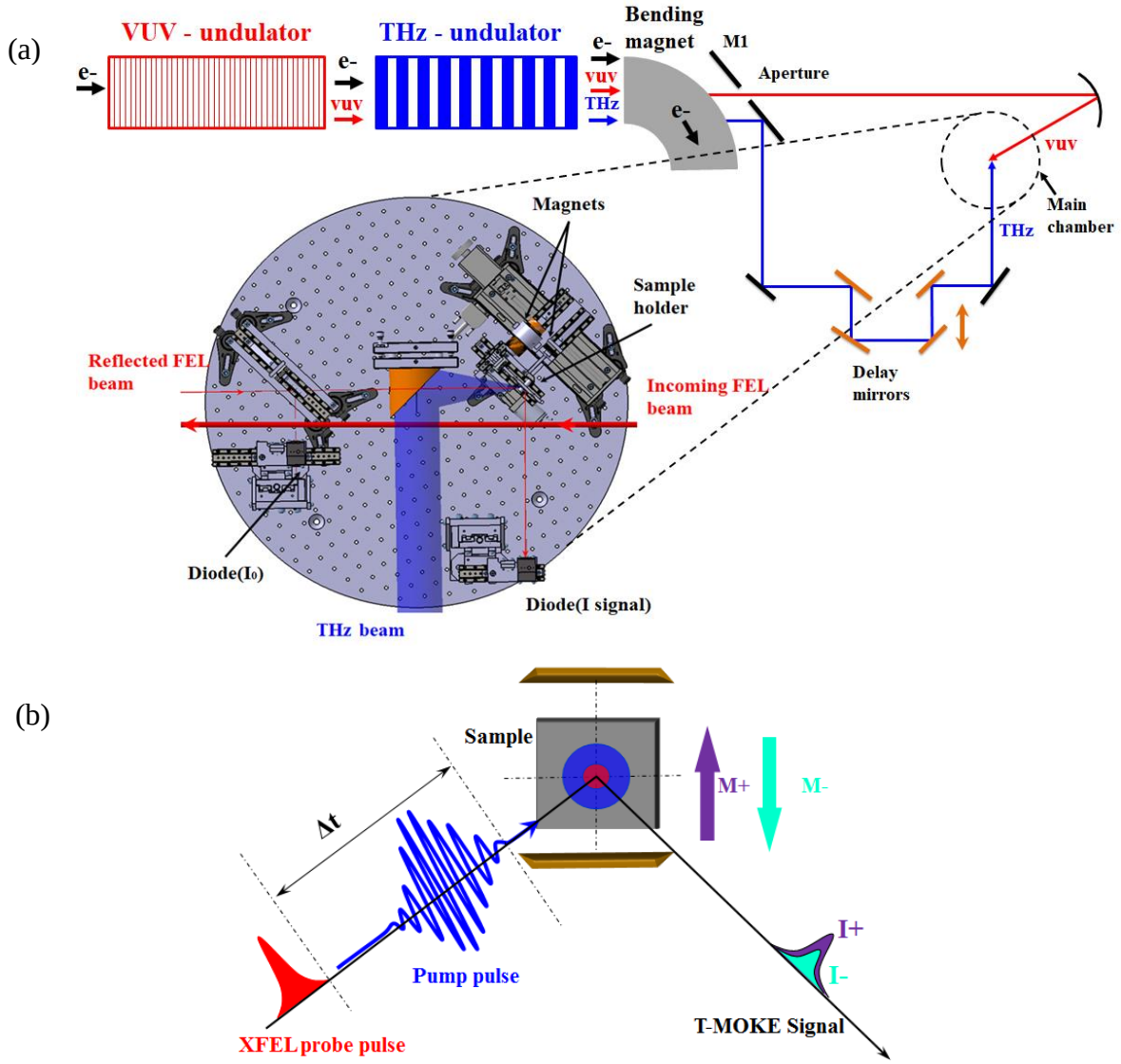

Figure 5.5: (a) Layout of the experimental setup: XUV probe pulse (red) and THz pump pulse (blue) are produced by an XUV undulator and the FIR undulator respectively. The zoom on the main chamber shows the THz beam focused onto the sample by a parabola and the probe beam going through the chamber before coming back focused onto the sample by a spherical mirror (not shown). Two APDs are used to measure the intensity of the probe beam (measuring the reflection on a Si_3N_4 window) and the signal reflected by the sample. (b) Time resolved T-MOKE configuration.

In more details, the experimental setup is constituted by two vacuum chambers. The incoming XUV beam (red) passes through the first chamber and is reflected back and focused by a spherical mirror in the second chamber (not show in the figure 5.5 (a)). The tilts of this back mirror are motorized in order change the position of the beam on the sample to find the spatial overlap with the THz beam. The reflected and focused XUV beam comes back to the main chamber passes through a center aperture in the THz parabola (orange) and eventually

arrives on the sample. In the meantime, a THz pulse arrives in the main chamber perpendicularly to the XUV beam and is focused onto the sample by the off-axis parabola.

To probe the dynamics of magnetization, we used the time-resolved T-MOKE (see figure 5.5 (b)), the basic principle of which has been introduced above. The incident angle on the sample is then chosen to be close to 45° to maximize the T-MOKE asymmetry. Two APDs measure the XUV beam intensity, $I_{0,}$ and the reflected signal, I_{signal}, from the sample. An electromagnet is used to magnetize the sample in plane in two opposite directions: M+ and M- (violet and green) giving rise to two different signals $I_{\pm}^{P}$.

We have studied a 10 nm thin Py sample sputtered on silicon substrate and capped with aluminum to prevent oxidation. For each time delay we measured $I_{\pm}^{P}$. The photon energy was tuned at 66.6 eV, at the resonant absorption $M_{2,3}$ edge for Ni.

5.3 Results and discussion

A. Results of pump with only THz and with mixed from THz to IR

Figure 5.6 shows the sample reflectivity as function of time delay for the two opposite magnetization direction of the sample in two different situations: pump with THz only (a filter is used to suppress additional radiation produced by the FIR undulator) and pump with all the radiation from the undulator (spanning a wavelength range from THz to IR). It is important to note that these measurements were performed using the same conditions except for the filter when we compare those two situations. When pumped only with THz (filter in), nothing happens (the curves are completely flat). It turned out that B-field from THz radiation is not sufficient to drive any magnetization change in the Py film in ultrafast time range (the focusing of the parabola being probably too large). However, when we took the filter out, a clear signal could be seen: the reflectivity changed as a function of delay. It has to be noted that the dynamics appears to be slower than with the usual IR pump. This is best seen in figure 5.6 (b) where we plotted the asymmetry for two different wavelength settings of the FIR undulator: 45 μm and 100 μm.

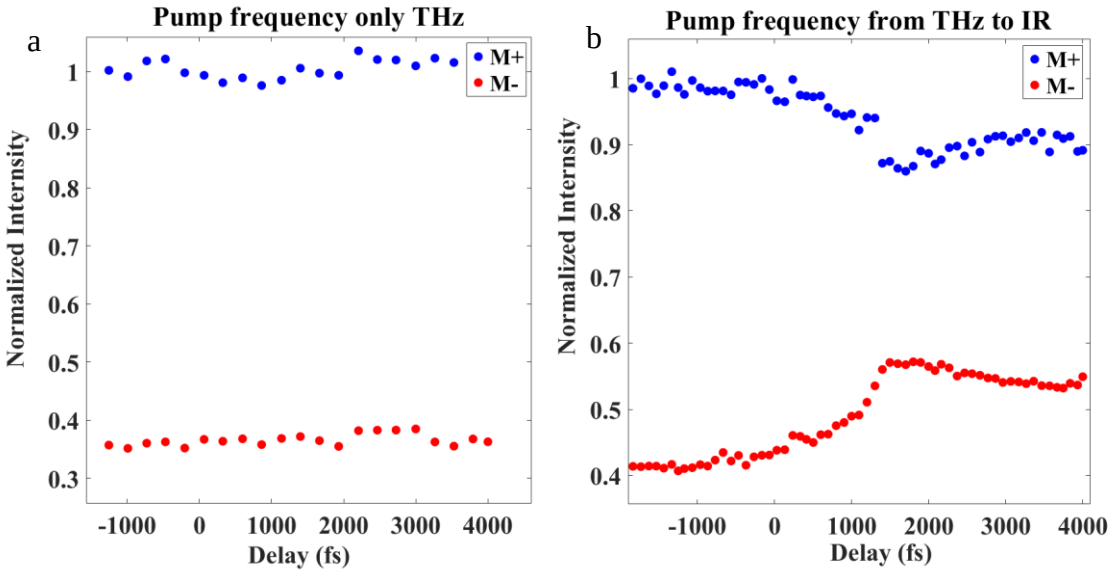

Figure 5.6: The normalized T-MOKE intensity I_+^P and I_-^P for two opposite applied magnetic field M+ and M- respectively as the function of time. (a) Only THz pump and (b) mixed frequency pump.

The magnetic dynamic at the shorter wavelength (45 μm) is slower than that at the longer wavelength (100 μm). This can be qualitatively understood by looking at figure 5.4 (a)

where we can see those shorter wavelengths are associated to shorter pulses. We can also see that due to the nine periods of the FIR undulator, the output pulse has ten periods of single waves. However, the exact shape of the pulse is not known (the intensity of each period can vary). Using the demagnetization curves, we can reconstruct the structure of the pulse. Indeed, as shown earlier, the analytical expression we use to fit the data depends on the demagnetization parameters but also on the shape of the pump beam, r(t):

$$\frac{\Delta A}{A} = \left\{ A_1 - \frac{\left(A_2\tau_E - A_1\tau_M\right)\cdot e^{-\frac{t}{\tau_M}}}{\tau_E - \tau_M} - \frac{\tau_E(A_2 - A_1)\cdot e^{-\frac{t}{\tau_M}}}{\tau_E - \tau_M} \right\} H(t) \times \Gamma(t) \qquad (46)$$

This expression is then the convolution between what we could call the impulse demagnetization (the demagnetization induced by an infinitely short pump pulse) and the pump pulse shape. Knowing the impulse response (in our case an IR femtosecond pump pulse is sufficiently shorter than the THz pulse to play this role), we can get a good estimation of the shape of the THz (mixed frequency in that case) pumped by fitting the data to our expression. It has to be noted that due to the properties of the undulator, the THz part of the pulse behave similarly than the shorter wavelength. Retrieving the pulse shape with the complete spectrum delivered by the undulator is equivalent to measure the pulse shape of the THz part only.

The results are shown in figure 5.7 (b). As expected the 45 μm pulse is shorter than the 100 μm pulse. Interestingly, for both pulses the first few oscillations are very weak and the energy of the pulse is mostly concentrated in two oscillations (about half the energy). This is particularly interesting to know for pump – probe experiments since although the THz is a few picoseconds long the energy is mostly concentrated in a few hundreds of femtoseconds. We will have to take into account this point to design our next THz pump – XUV probe experiment.

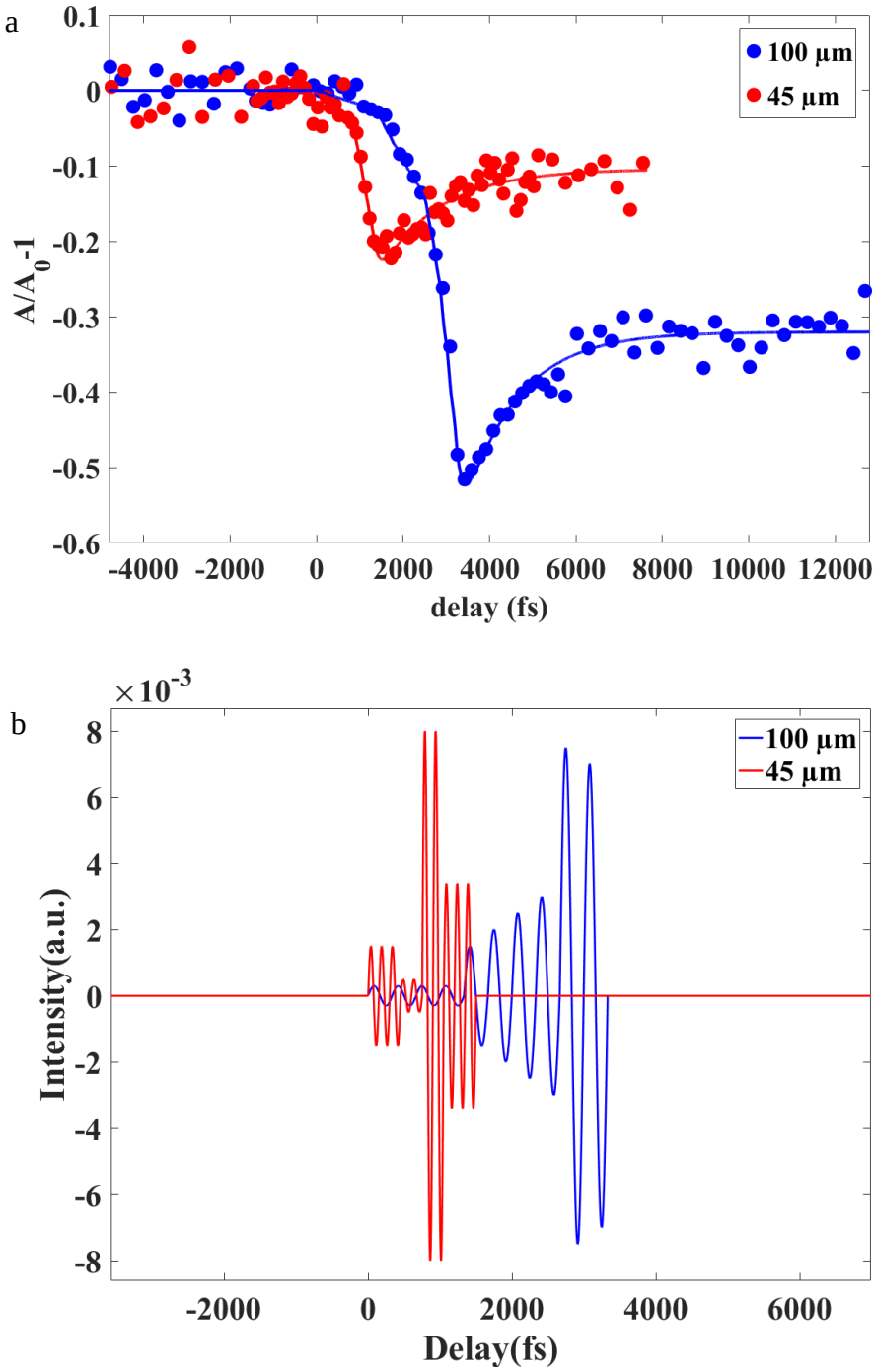

Figure 5.7: (a) Normalized T-MOKE asymmetry, A/A_0, as a function of time for fundamental pump wavelengths of 45 µm and 100 µm. The points represent the experimental data and the lines represent the fit. (b) Reconstructed shape of the electric field of the THz pulses. Wavelengths: 45 µm and 100 µm.

6 Chapter 6: Superdiffusive Spin Transport from Co/Pd Multilayer to Pt Cap and Buffer Layer

6.1 Introduction

The emission of spin current is one of the fundamentals of spintronics, the discipline that promises more efficient electronic devices. Recently, much attention has been paid to the realization and understanding of spin current generated by the excitation of an ultrashort laser pulse. In addition, as proposed by Battiato *et al.* [3] with the super-diffuse spin transport mechanism, this type of current could have explained part of the ultrafast demagnetization phenomenon. Despite many experimental observations that could indicate the existence of superdiffusive transport. Its importance for explaining the ultra-fast demagnetization is still determining [105][106].

Part of the difficulty to quantify the importance of superdiffusive spin transport comes from the fact that one must measure the magnetization transfer to the metallic layer from the magnetic layer. Measuring the magnetization of the metallic layer is at best tricky at worst impossible. For example, in the initial system studied by Battiato, a nickel film on aluminum, there is no easy way to quantify the magnetization of the Al layer.

To circumvent this difficulty, we chose to study a carefully design sample: a Co magnetic layer surrounded by Pt buffer and cap layers grown on an insulating substrates. The magnetization of the Co and Pt layers can be probed selectively by using photons in resonance with the Co $M_{2,3}$ (60 eV) and Pt N_7 (71 eV) absorption edges to investigate the ultrafast demagnetization process of these two elements. According to the model of superdiffusive spin transport, spin-polarized electrons will be generated by the pump pulse and then partly transport from the Co layer to the Pt layers. Consequently, the magnetization of the Pt layer should be enhanced a few hundreds of femtoseconds after excitation.

6.2 Experimental setup

In our experiment, FEL source is applied to probe element-specific magnetization dynamics in multispecies magnetic systems[89][107][108] Here, resonant magnetic scattering technique [109] was used. This nondestructive technique at FLASH has been proved that it is an ideal tool to record a magnetic diffraction pattern within several tens of fs without destroying the sample [110][111]. Due to the magnetic circular dichroism (MCD) of the transition metals' M-edges, the optical index depends on the sample's magnetization. More precisely, the amplitude of the MCD effect depends on the projection of the magnetic moment on the propagation direction of the incident radiation. We note that the integrated scattering intensity is related to the magnetization itself. Hence, by following the time evolution of the integrated scattering intensity, one can also study demagnetization dynamics in the experiment [112].

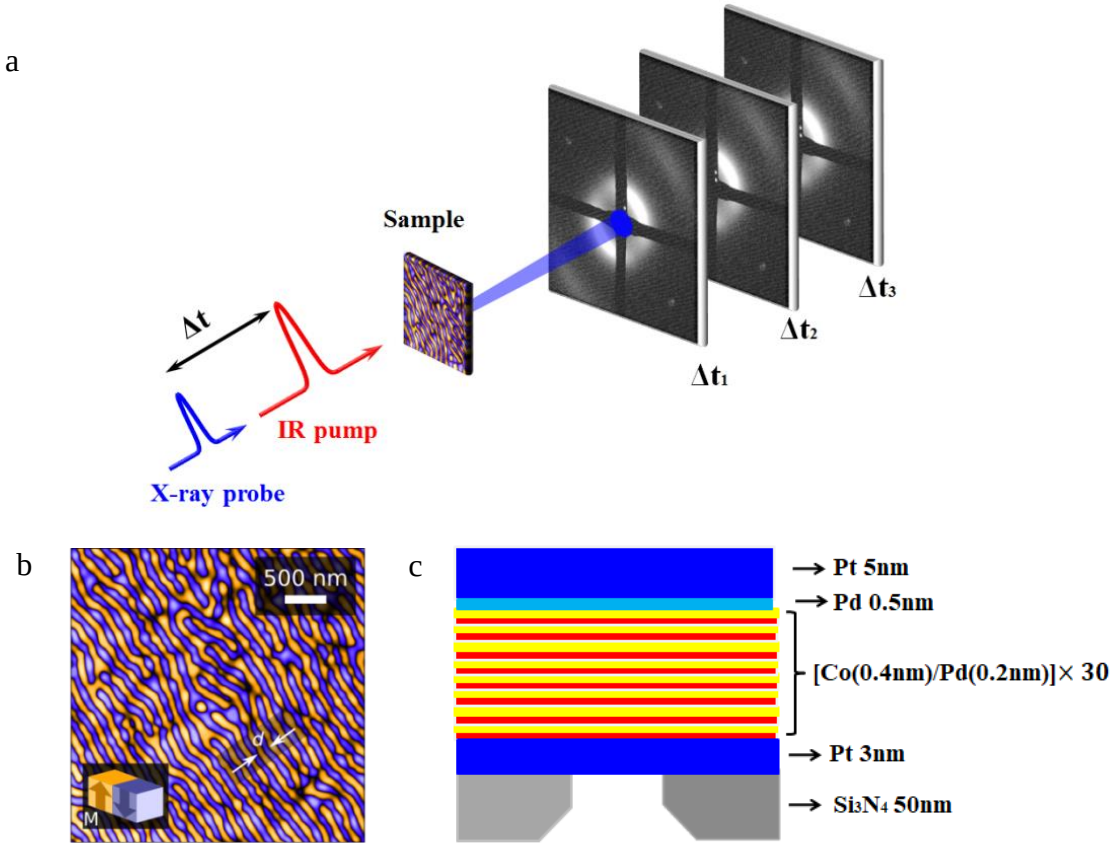

Figure 6.1: Description of the sample (a) layered structure deposited by magnetron sputtering and (b) magnetic structure measured by Magnetic force microscopy showing the up (yellow) and down (violet) magnetic domains. (c) Layout of the experimental setup. The IR (red) and XUV (blue) pulses are focused and overlapped onto the sample. The IR laser is filtered out and the XUV scattering pattern is recorded on a CCD camera.

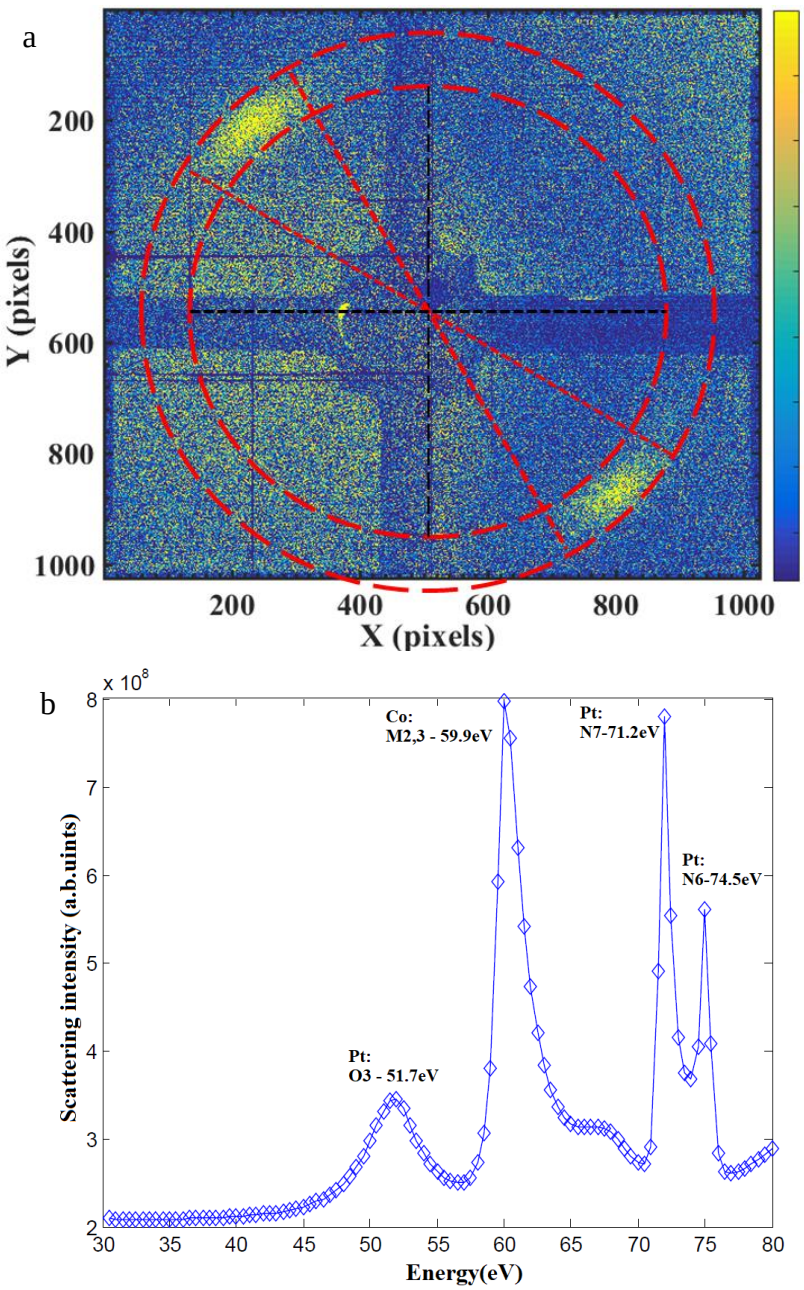

Figure 6.2: (a) Resonant magnetic scattering pattern recorded on the CCD camera with probing with Co $M_{2,3}$ edge. (b) Scattering intensity as the function of photon energy recorded on a Co/Pt multilayer showing 4 peaks corresponding to the following absorption edges: Pt O_3, Co $M_{2,3}$, Pt N_7, and Pt N_6.

More specifically, the sample employed for this demonstration consists of 30 repetitions of Co (0.4 nm)/Pd (0.2 nm) sputtered on a 50 nm thick Si_3N_4 square window of 100 × 100 μm^2 (see figure 6.1 (c)). This magnetic layer is grown on a 5 nm Pt layer and capped with another 5 nm Pt layer. This buffer and cap layers are isolated from the Co by 0.5 nm thick Pd layers. Hence the magnetization of Pt cannot come from direct exchange

interaction with the Co layers as in Co/Pt multilayers. With this design, any sizable magnetization transfer from the Co/Pd magnetic layer should show up in the Pt layer. We chose a Co/Pd multilayer instead pure Co in order to obtain a sample with out of plane magnetic anisotropy and small magnetic domains (see figure 6.1 (b)). We can then employ the technique of resonant magnetic scattering to probe the magnetization of the sample with the advantage of being able to probe completely our sample in transmission [112]. The schematic description of the experimental setup is presented in figure 6.1 (a): the sample is excited by an IR femtosecond pulse and its magnetic state is probed by an XUV femtosecond pulse which is scattered by the magnetic domain structure. The scattering pattern is then recorded by a CCD camera (pn-CCD).

As I discussed in the chapter 3, the integrated scattered intensity is proportional to the magnetization square. By calculated this intensity for each delay, we can plot the magnetization dynamics. Figure 6.2 (a) illustrates the scattering pattern recorded on the CCD camera by averaging the accumulation of 10 shots. Here, this pattern consists of two spots since the magnetic domains were aligned prior to the experiment. Figure 6.2 (b) shows that scattering intensity as the function of photon energy showing that one can probe the magnetization of Co at 60 eV (Co $M_{2,3}$ edges) and of Pt at 71 eV (Pt N_7 edge) Note that both peaks are very well separated and only weekly overlap with other edges.

6.3 Results and Discussion

The demagnetization curves are presented in the figure 6.3, and it shows the magnetization (M normalized to the unpumped magnetization, M_0) as a function of time delay. The solid lines are fits by a double exponential expression (see chapter 4). The maximum demagnetization (M-1) min, the thermalization time (τ_E) and the demagnetization time (τ_M) are reported in the Table 6-1.

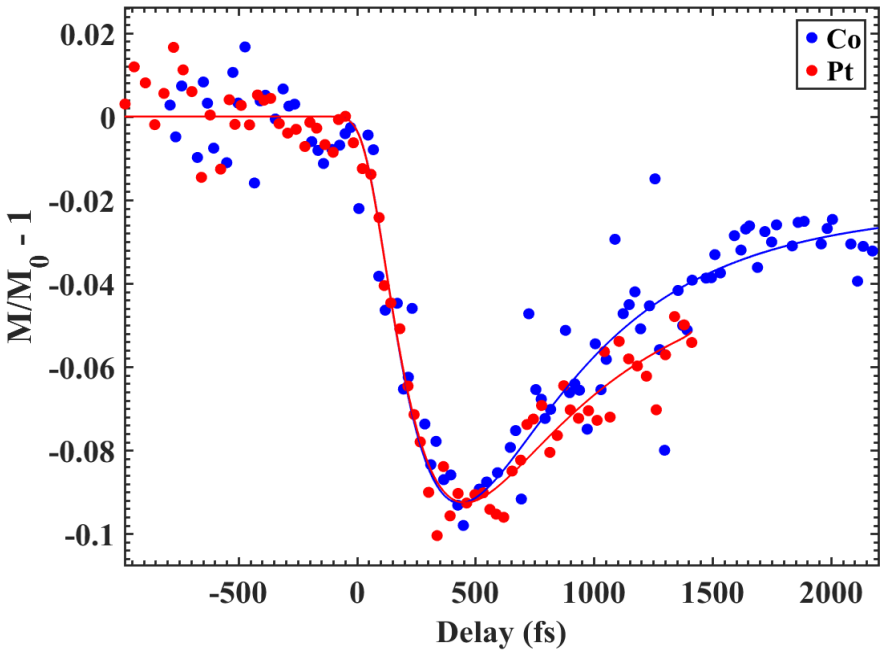

Figure 6.3: Demagnetization curves of a Pt/{Co/Pd}×30/Pt sample recorded at the Co $M_{2,3}$ absorption edges (blue) and Pt N_7 absorption edge (red) .

Sample	$(M-1)_{min}$	τ_M (fs)
Co (59.9 eV)	9.3%	187 ± 6
Pt (71.2 eV)	9.2%	186 ± 8

Table 6-1: Fitting parameters of demagnetization curves of Co and Pt.

From the figure 6.3 (and from the fit parameters), it is clear that the demagnetization is very similar for both energies. It could indicate that both Co and Pt were magnetized at first and undergo the exact same demagnetization. It is however unlikely that the Pt layer had any magnetization at the beginning of the experiment (because of the design of the sample). The

signal measured at 71 eV is the most probably the far edge of the Co $M_{2,3}$ resonance. The point is reinforcing by the fact that the scattering at 71 eV is much weaker than at 60 eV. Our observation then shows that any magnetization transfer to the Pt layer must be very small since it cannot even make a difference between the two curves. Contrary to previous report on Fe Ni bilayers [106], our work seems to demonstrate that the superdiffusive spin transport contribution to ultrafast demagnetization is weak.

7 Chapter 7: Conclusion and Perspectives

The main conclusion of this thesis is the realization of the split and delay setup and its application to the study magnetization dynamics in the nickel and permalloy systems. We have described our setup and shown that it was working in reflection as well as in transmission geometry. An unprecedented time resolution for an ultrafast magnetization experiment of below 10 fs could be achieved. The first results show that the magnetic dynamics after femtosecond excitation of Ni is slower in permalloy than in pure nickel. The dynamics of Fe in permalloy also appear to be slower than Ni. But the main observation is the difference in "magnetic" response at different energies around the same absorption edges. This point is of great importance for the community studying ultrafast magnetization with X-rays and it could lead to the reinterpretation of several previous reports.

In the THz part, unfortunately we did not observed any ultrafast coherent magnetization control by the THz pump. The magnetic field of the THz pump obtained was too weak to significantly manipulate the magnetization of the film. We could, however, detect at least the non-coherent excitation of the demagnetization process by the shorter wavelength components of the THz pulse. From this observation, we were able to reconstruct the shape of the electric field of the THz pump pulse as a function of time. This method also helps to quantify the magnetic field of the THz pulse, which will be beneficial for future THz experiments.

Finally, we showed that superdiffusive spin transport does not play a significant role for ultrafast demagnetization. For that we have studied the possible spin transport from a Co/Pd multilayer to Pt buffer and cap layers. This system is ideal to observe such spin transport since the resonant magnetic response of Pt is very high and since the magnetization is bound to be either in the Co/Pd or Pt layers because of the growth on insulating substrate.

In the future, we want to exploit the split and delay setup. One of the first follow up experiment will be to carefully study the wavelength dependence of the magnetization dynamics around an absorption edge, Ni $M_{2,3}$ for example. This study could be essential for our understanding of magnetization dynamics or at least magneto-optics dynamics. We could also revisit previous experiment on Fe Ni bilayers with the advantages to be in transmission geometry, to have a more homogeneous excitation profile and to have an improve time resolution. We will of course try to conduct another THz pump experiment with an improve

fluence excitation to be able to observe the coherent control of the magnetization and its wavelength dependence.

Bibliography

[1] E. Beaurepaire, J.-C. Merle, A. Daunois, and J.-Y. Bigot, 'Ultrafast spin dynamics in ferromagnetic nickel', *Physical review letters*, vol. 76, no. 22, p. 4250, 1996.

[2] B. Koopmans, H. H. J. E. Kicken, M. van Kampen, and W. J. M. de Jonge, 'Microscopic model for femtosecond magnetization dynamics', *Journal of Magnetism and Magnetic Materials*, vol. 286, pp. 271–275, Feb. 2005.

[3] M. Battiato, K. Carva, and P. M. Oppeneer, 'Superdiffusive Spin Transport as a Mechanism of Ultrafast Demagnetization', *Physical Review Letters*, vol. 105, no. 2, Jul. 2010.

[4] M. N. Baibich *et al.*, 'Giant magnetoresistance of (001) Fe/(001) Cr magnetic superlattices', *Physical review letters*, vol. 61, no. 21, p. 2472, 1988.

[5] G. Binasch, P. Grünberg, F. Saurenbach, and W. Zinn, 'Enhanced magnetoresistance in layered magnetic structures with antiferromagnetic interlayer exchange', *Physical review B*, vol. 39, no. 7, p. 4828, 1989.

[6] E. Pavarini and Institute for Advanced Simulation, Eds., *Emergent phenomena in correlated matter: lecture notes of the Autumn School Correlated Electrons 2013 at Forschungszentrum Jülich, 23 – 27 September 2013*. Jülich: Forschungszentrum Jülich, 2013.

[7] E. G. Batyev, 'Pauli paramagnetism and Landau diamagnetism', *Physics-Uspekhi*, vol. 52, no. 12, pp. 1245–1246, Dec. 2009.

[8] M. Faraday, *TheCorrespondence of Michael Faraday: 1849-1855*. IET, 1991.

[9] C. A. Russell, *Michael Faraday: Physics and Faith*. Oxford University Press, USA, 2000.

[10] R. Fitzpatrick, 'Thermodynamics and Statistical Mechanics', p. 286.

[11] H. Gould and J. Tobochnik, *Statistical and Thermal Physics: With Computer Applications*. Princeton University Press, 2010.

[12] D. L. Goodstein, *States of Matter*. Courier Corporation, 1985.

[13] K. Maki, 'Effect of Pauli Paramagnetism on Magnetic Properties of High-Field Superconductors', *Physical Review*, vol. 148, no. 1, pp. 362–369, Aug. 1966.

[14] S. Foner, ‘Pauli paramagnetism in metals with high densities of states’, *Journal of Research of the National Bureau of Standards Section A: Physics and Chemistry*, vol. 74A, no. 4, p. 567, Jul. 1970.

[15] N. Bohr, *Studier over metallernes elektrontheori*. Thaning et Appel in Komm., 1911.

[16] ‘Zur Theorie des Ferromagnetismus’, p. 14.

[17] P. Weiss, ‘L’hypothèse du champ moléculaire et la propriété ferromagnétique’, *Journal de Physique Théorique et Appliquée*, vol. 6, no. 1, pp. 661–690, 1907.

[18] R. Kaul and E. D. Thompson, ‘Temperature Dependence of the Magnetic Moment and Hyperfine Constant of Nickel’, *Journal of Applied Physics*, vol. 40, no. 3, pp. 1383–1384, Mar. 1969.

[19] C. A. Fowler and E. M. Fryer, ‘Magnetic Domains by the Longitudinal Kerr Effect’, *Physical Review*, vol. 94, no. 1, pp. 52–56, Apr. 1954.

[20] A. P. Guimarães, *From Lodestone to Supermagnets: Understanding Magnetic Phenomena*. Wiley-VCH, 2005.

[21] C. Kittel and J. K. Galt, ‘Ferromagnetic Domain Theory’, in *Solid State Physics*, vol. 3, Elsevier, 1956, pp. 437–564.

[22] D. D. Tang and Y.-J. Lee, *Magnetic Memory: Fundamentals and Technology*. Cambridge University Press, 2010.

[23] Z. Frait and R. Gemperle, ‘THE g-FACTOR AND SURFACE MAGNETIZATION OF PURE IRON ALONG [100] AND [111] DIRECTIONS’, *Le Journal de Physique Colloques*, vol. 32, no. C1, pp. C1-541-C1-542, Feb. 1971.

[24] P. A. M. Dirac, ‘On the Theory of Quantum Mechanics’.

[25] *Concept of Spin Hamiltonian, Forms of Zero Field Splitting and Electronic Zeeman Hamiltonians and Relations Between Parameters Used in EPR: A Critical Review*. 1987.

[26] M. A. Ruderman and C. Kittel, ‘Indirect Exchange Coupling of Nuclear Magnetic Moments by Conduction Electrons’, *Physical Review*, vol. 96, no. 1, pp. 99–102, Oct. 1954.

[27] Y. Yafet, ‘Ruderman-Kittel-Kasuya-Yosida range function of a one-dimensional free-electron gas’, *Physical Review B*, vol. 36, no. 7, pp. 3948–3949, Sep. 1987.

[28] L. H. Thomas, ‘The Motion of the Spinning Electron’, *Nature*, vol. 117, no. 2945, p. 514, Apr. 1926.

[29] L. H. Thomas, ‘The calculation of atomic fields’, *Mathematical Proceedings of the Cambridge Philosophical Society*, vol. 23, no. 5, pp. 542–548, Jan. 1927.

[30] A. Kirilyuk, A. V. Kimel, and T. Rasing, ‘Ultrafast optical manipulation of magnetic order’, *Reviews of Modern Physics*, vol. 82, no. 3, pp. 2731–2784, Sep. 2010.

[31] H. yon, ‘Dr. Arnold Berliner u~a Prof. Dr. August PBtter’, p. 2.

[32] L. LANDAU and E. LIFSHITS, ‘ON THE THEORY OF THE DISPERSION OF MAGNETIC PERMEABILITY IN FERROMAGNETIC BODIES’, vol. 53, p. 9.

[33] ‘CiNii Articles - A Lagrangian Formulation of the Gyromagnetic Equation of the Magnetization Field’. [Online]. Available: https://ci.nii.ac.jp/naid/10013560509/en/. [Accessed: 30-Jul-2018].

[34] U. Atxitia and O. Chubykalo-Fesenko, ‘Ultrafast magnetization dynamics rates within the Landau-Lifshitz-Bloch model’, *Physical Review B*, vol. 84, no. 14, Oct. 2011.

[35] F. Bloch, ‘Nuclear induction’, *Physical review*, vol. 70, no. 7–8, p. 460, 1946.

[36] U. Atxitia, O. Chubykalo-Fesenko, J. Walowski, A. Mann, and M. Münzenberg, ‘Evidence for thermal mechanisms in laser-induced femtosecond spin dynamics’, *Physical Review B*, vol. 81, no. 17, May 2010.

[37] B. Koopmans *et al.*, ‘Explaining the paradoxical diversity of ultrafast laser-induced demagnetization’, *Nature Materials*, Dec. 2009.

[38] S. I. Anisimov, ‘Electron emission from metal surfaces exposed to ultrashort laser pulses’, p. 3.

[39] D. M. Edwards and J. A. Hertz, ‘Electron-magnon interactions in itinerant ferromagnetism. II. Strong ferromagnetism’, *Journal of Physics F: Metal Physics*, vol. 3, no. 12, p. 2191, 1973.

[40] J. Stöhr and H. C. Siegmann, *Magnetism: From Fundamentals to Nanoscale Dynamics*. Berlin Heidelberg: Springer-Verlag, 2006.

[41] R. _ J. Elliott, ‘Theory of the effect of spin-orbit coupling on magnetic resonance in some semiconductors’, *Physical Review*, vol. 96, no. 2, p. 266, 1954.

[42] M. Cinchetti *et al.*, ‘Spin-Flip Processes and Ultrafast Magnetization Dynamics in Co: Unifying the Microscopic and Macroscopic View of Femtosecond Magnetism’, *Physical Review Letters*, vol. 97, no. 17, Oct. 2006.

[43] W. L. O’Brien and B. P. Tonner, ‘Orbital and spin sum rules in x-ray magnetic circular dichroism’, *Physical Review B*, vol. 50, no. 17, pp. 12672–12681, Nov. 1994.

[44] I. Radu *et al.*, ‘Laser-Induced Magnetization Dynamics of Lanthanide-Doped Permalloy Thin Films’, *Physical Review Letters*, vol. 102, no. 11, Mar. 2009.

[45] K. Carva, M. Battiato, and P. M. Oppeneer, '*Ab Initio* Investigation of the Elliott-Yafet Electron-Phonon Mechanism in Laser-Induced Ultrafast Demagnetization', *Physical Review Letters*, vol. 107, no. 20, Nov. 2011.

[46] S. Essert and H. C. Schneider, 'Electron-phonon scattering dynamics in ferromagnetic metals and their influence on ultrafast demagnetization processes', *Physical Review B*, vol. 84, no. 22, Dec. 2011.

[47] D. Rudolf *et al.*, 'Ultrafast magnetization enhancement in metallic multilayers driven by superdiffusive spin current', *Nature Communications*, vol. 3, p. 1037, Sep. 2012.

[48] A. J. Schellekens, W. Verhoeven, T. N. Vader, and B. Koopmans, 'Investigating the contribution of superdiffusive transport to ultrafast demagnetization of ferromagnetic thin films', *Applied Physics Letters*, vol. 102, no. 25, p. 252408, Jun. 2013.

[49] E. Carpene, E. Mancini, C. Dallera, D. Schwen, C. Ronning, and S. De Silvestri, 'Ultrafast carrier dynamics in tetrahedral amorphous carbon: carrier trapping versus electron–hole recombination', *New Journal of Physics*, vol. 9, no. 11, pp. 404–404, Nov. 2007.

[50] F. Bloch, 'Zur Theorie des Ferromagnetismus', *Z. Physik*, vol. 61, no. 3–4, pp. 206–219, Mar. 1930.

[51] G. P. Zhang and W. Hübner, 'Laser-Induced Ultrafast Demagnetization in Ferromagnetic Metals', *Physical Review Letters*, vol. 85, no. 14, pp. 3025–3028, Oct. 2000.

[52] F. Dalla Longa, J. T. Kohlhepp, W. J. M. de Jonge, and B. Koopmans, 'Influence of photon angular momentum on ultrafast demagnetization in nickel', *Physical Review B*, vol. 75, no. 22, Jun. 2007.

[53] P. Prigent *et al.*, 'Progress on the Femto-Slicing Project at the Synchrotron SOLEIL', *Journal of Physics: Conference Series*, vol. 425, no. 7, p. 072022, Mar. 2013.

[54] M. Lewenstein, P. Balcou, M. Y. Ivanov, A. L'huillier, and P. B. Corkum, 'Theory of high-harmonic generation by low-frequency laser fields', *Physical Review A*, vol. 49, no. 3, p. 2117, 1994.

[55] J. M. J. Madey, 'Stimulated Emission of Bremsstrahlung in a Periodic Magnetic Field', *Journal of Applied Physics*, vol. 42, no. 5, pp. 1906–1913, Apr. 1971.

[56] L. R. Elias, W. M. Fairbank, J. M. J. Madey, H. A. Schwettman, and T. I. Smith, 'Observation of Stimulated Emission of Radiation by Relativistic Electrons in a Spatially Periodic Transverse Magnetic Field', *Physical Review Letters*, vol. 36, no. 13, pp. 717–720, Mar. 1976.

[57] D. A. G. Deacon, L. R. Elias, J. M. J. Madey, G. J. Ramian, H. A. Schwettman, and T. I. Smith, ‘First Operation of a Free-Electron Laser’, *PHYSICAL REVIEW LETTERS*, p. 3, 1977.

[58] C. Pellegrini and J. Stöhr, ‘X-ray free-electron lasers—principles, properties and applications’, *Nuclear Instruments and Methods in Physics Research Section A: Accelerators, Spectrometers, Detectors and Associated Equipment*, vol. 500, no. 1–3, pp. 33–40, Mar. 2003.

[59] Z. Huang and K.-J. Kim, ‘Review of x-ray free-electron laser theory’, *Physical Review Special Topics - Accelerators and Beams*, vol. 10, no. 3, Mar. 2007.

[60] E. Allaria *et al.*, ‘Highly coherent and stable pulses from the FERMI seeded free-electron laser in the extreme ultraviolet’, *Nature Photonics*, vol. 6, no. 10, pp. 699–704, Oct. 2012.

[61] R. Bonifacio, C. Pellegrini, and L. M. Narducci, ‘Collective instabilities and high-gain regime in a free electron laser’, *Optics Communications*, vol. 50, no. 6, pp. 373–378, Jul. 1984.

[62] M. J. Hogan *et al.*, ‘Measurements of Gain Larger than 105 at 12 mm in a Self-Amplified Spontaneous-Emission Free-Electron Laser’, *PHYSICAL REVIEW LETTERS*, vol. 81, no. 22, p. 4, 1998.

[63] S. V. Milton, ‘Exponential Gain and Saturation of a Self-Amplified Spontaneous Emission Free-Electron Laser’, *Science*, vol. 292, no. 5524, pp. 2037–2041, Jun. 2001.

[64] W. Ackermann *et al.*, ‘Operation of a free-electron laser from the extreme ultraviolet to the water window’, *Nature Photonics*, vol. 1, no. 6, pp. 336–342, Jun. 2007.

[65] M. Labat *et al.*, ‘High-Gain Harmonic-Generation Free-Electron Laser Seeded by Harmonics Generated in Gas’, *Physical Review Letters*, vol. 107, no. 22, Nov. 2011.

[66] G. De Ninno *et al.*, ‘Generation of Ultrashort Coherent Vacuum Ultraviolet Pulses Using Electron Storage Rings: A New Bright Light Source for Experiments’, *Physical Review Letters*, vol. 101, no. 5, Jul. 2008.

[67] M. Labat *et al.*, ‘Coherent harmonic generation on UVSOR-II storage ring’, *The European Physical Journal D*, vol. 44, no. 1, pp. 187–200, Jul. 2007.

[68] M. Vogt, B. Faatz, J. Feldhaus, K. Honkavaara, S. Schreiber, and R. Treusch, ‘STATUS OF THE SOFT X-RAY FREE ELECTRON LASER FLASH’, p. 3.

[69] K. Honkavaara, B. Faatz, J. Feldhaus, S. Schreiber, R. Treusch, and M. Vogt, ‘FLASH: First Soft X-ray FEL Operating Two Undulator Beamlines Simultaneously’, p. 5, 2014.

[70] K. Honkavaara *et al.*, ‘Status of the FLASH II Project’, p. 4, 2012.

[71] M. Vogt, B. Faatz, J. Feldhaus, K. Honkavaara, S. Schreiber, and R. Treusch, 'Status of the Free Electron Laser User Facility FLASH', *Free Electron Lasers*, p. 3, 2014.

[72] 'FL Beamlines (FLASH2)'. [Online]. Available: http://photon-science.desy.de/facilities/flash/beamlines/fl_beamlines_flash2/index_eng.html. [Accessed: 10-Aug-2018].

[73] B. Faatz *et al.*, 'Simultaneous operation of two soft x-ray free-electron lasers driven by one linear accelerator', *New Journal of Physics*, vol. 18, no. 6, p. 062002, Jun. 2016.

[74] E. Plönjes, B. Faatz, M. Kuhlmann, and R. Treusch, 'FLASH2: Operation, beamlines, and photon diagnostics', 2016, p. 020008.

[75] P. Schmüser, M. Dohlus, and J. Rossbach, *Ultraviolet and Soft X-Ray Free-Electron Lasers*, vol. 229. Berlin, Heidelberg: Springer Berlin Heidelberg, 2009.

[76] 'SAS - Research - Projects -'. [Online]. Available: https://www.sav.sk/?lang=en&doc=activity-proj-int. [Accessed: 31-Jul-2018].

[77] O. Hellwig, A. Berger, J. B. Kortright, and E. E. Fullerton, 'Domain structure and magnetization reversal of antiferromagnetically coupled perpendicular anisotropy films', *Journal of Magnetism and Magnetic Materials*, vol. 319, no. 1–2, pp. 13–55, Dec. 2007.

[78] J. Kerr, 'XLIII. On rotation of the plane of polarization by reflection from the pole of a magnet', *The London, Edinburgh, and Dublin Philosophical Magazine and Journal of Science*, vol. 3, no. 19, pp. 321–343, May 1877.

[79] 'Michael Faraday (1791-1867) - Faradays Diaries, being the various philosophical noted of experimental investigation made by Michael Faraday... ed. by Thomas Martin..., vol. 4 Nov. 12 1839-June 26 1847'. [Online]. Available: https://www.royalcollection.org.uk/collection/1092398/faradays-diaries-being-the-various-philosophical-noted-of-experimental. [Accessed: 30-Jul-2018].

[80] J. Kuneš *et al.*, 'X-ray Faraday effect at the L 2 , 3 edges of Fe, Co, and Ni: Theory and experiment', *Physical Review B*, vol. 64, no. 17, Oct. 2001.

[81] W. S. Kim, M. Aderholz, and W. Kleemann, 'Calibration of polar Kerr rotation and ellipticity measurements', *Measurement Science and Technology*, vol. 4, no. 11, pp. 1275–1280, Nov. 1993.

[82] E. Carpene, E. Mancini, C. Dallera, M. Brenna, E. Puppin, and S. De Silvestri, 'Dynamics of electron-magnon interaction and ultrafast demagnetization in thin iron films', *Physical Review B*, vol. 78, no. 17, Nov. 2008.

[83] B. Koopmans, M. Van Kampen, J. T. Kohlhepp, and W. J. M. De Jonge, 'Ultrafast magneto-optics in nickel: magnetism or optics?', *Physical Review Letters*, vol. 85, no. 4, p. 844, 2000.

[84] J.-Y. Bigot, L. Guidoni, E. Beaurepaire, and P. N. Saeta, 'Femtosecond Spectrotemporal Magneto-optics', *Physical Review Letters*, vol. 93, no. 7, Aug. 2004.

[85] T. Kampfrath, R. G. Ulbrich, F. Leuenberger, M. Münzenberg, B. Sass, and W. Felsch, 'Ultrafast magneto-optical response of iron thin films', *Physical Review B*, vol. 65, no. 10, Feb. 2002.

[86] S. Mathias *et al.*, 'Probing the timescale of the exchange interaction in a ferromagnetic alloy', *Proceedings of the National Academy of Sciences*, vol. 109, no. 13, pp. 4792–4797, Mar. 2012.

[87] S. Jana *et al.*, 'A setup for element specific magnetization dynamics using the transverse magneto-optic Kerr effect in the energy range of 30-72 eV', *Review of Scientific Instruments*, vol. 88, no. 3, p. 033113, Mar. 2017.

[88] I. Radu *et al.*, 'Ultrafast and Distinct Spin Dynamics in Magnetic Alloys', *SPIN*, vol. 05, no. 03, p. 1550004, Sep. 2015.

[89] C. La-O-Vorakiat *et al.*, 'Ultrafast Demagnetization Dynamics at the M Edges of Magnetic Elements Observed Using a Tabletop High-Harmonic Soft X-Ray Source', *Physical Review Letters*, vol. 103, no. 25, Dec. 2009.

[90] B. Vodungbo *et al.*, 'Laser-induced ultrafast demagnetization in the presence of a nanoscale magnetic domain network', *Nature Communications*, vol. 3, p. 999, Aug. 2012.

[91] T. Kataoka *et al.*, 'Electronic structure and magnetism of the diluted magnetic semiconductor Fe-doped ZnO nanoparticles', *Journal of Applied Physics*, vol. 107, no. 3, p. 033718, Feb. 2010.

[92] J. B. Kortright and S.-K. Kim, 'Resonant magneto-optical properties of Fe near its 2 p levels: Measurement and applications', *Physical Review B*, vol. 62, no. 18, pp. 12216–12228, Nov. 2000.

[93] S. Valencia *et al.*, 'Faraday rotation spectra at shallow core levels: 3 *p* edges of Fe, Co, and Ni', *New Journal of Physics*, vol. 8, no. 10, pp. 254–254, Oct. 2006.

[94] S. Mathias *et al.*, 'Probing the timescale of the exchange interaction in a ferromagnetic alloy', *Proceedings of the National Academy of Sciences*, vol. 109, no. 13, pp. 4792–4797, 2012.

[95] B. Pfau *et al.*, ‘Ultrafast optical demagnetization manipulates nanoscale spin structure in domain walls’, *Nature Communications*, vol. 3, p. 1100, Oct. 2012.

[96] S. D. Bader and S. S. P. Parkin, ‘Spintronics’, *Annual Review of Condensed Matter Physics*, vol. 1, no. 1, pp. 71–88, Aug. 2010.

[97] C. Vicario *et al.*, ‘Off-resonant magnetization dynamics phase-locked to an intense phase-stable terahertz transient’, *Nature Photonics*, vol. 7, no. 9, pp. 720–723, Aug. 2013.

[98] ‘New Device Converts DC Electric Field to Terahertz Radiation’, *Innovation Toronto*, 08-Aug-2015. .

[99] T. Kampfrath, K. Tanaka, and K. A. Nelson, ‘Resonant and nonresonant control over matter and light by intense terahertz transients’, *Nature Photonics*, vol. 7, no. 9, pp. 680–690, Aug. 2013.

[100] S. Kovalev *et al.*, ‘Selective THz control of magnetic order: new opportunities from superradiant undulator sources’, *Journal of Physics D: Applied Physics*, vol. 51, no. 11, p. 114007, Mar. 2018.

[101] N. Stojanovic and M. Drescher, ‘Accelerator- and laser-based sources of high-field terahertz pulses’, *Journal of Physics B: Atomic, Molecular and Optical Physics*, vol. 46, no. 19, p. 192001, Oct. 2013.

[102] B. Green *et al.*, ‘High-Field High-Repetition-Rate Sources for the Coherent THz Control of Matter’, *Scientific Reports*, vol. 6, no. 1, Apr. 2016.

[103] M. Gensch, L. Bittner, M. Roehling, U. Fruehling, M. Hesse, and U. Hahn, ‘Status of the infrared undulator beamline at FLASH’, p. 7.

[104] M. Gensch *et al.*, ‘New infrared undulator beamline at FLASH’, *Infrared Physics & Technology*, vol. 51, no. 5, pp. 423–425, May 2008.

[105] G.-M. Choi, B.-C. Min, K.-J. Lee, and D. G. Cahill, ‘Spin current generated by thermally driven ultrafast demagnetization’, *Nature Communications*, vol. 5, Jul. 2014.

[106] E. Turgut *et al.*, ‘Controlling the Competition between Optically Induced Ultrafast Spin-Flip Scattering and Spin Transport in Magnetic Multilayers’, *Physical Review Letters*, vol. 110, no. 19, May 2013.

[107] I. Radu *et al.*, ‘Transient ferromagnetic-like state mediating ultrafast reversal of antiferromagnetically coupled spins’, *Nature*, vol. 472, no. 7342, pp. 205–208, Apr. 2011.

[108] C. La-O-Vorakiat *et al.*, 'Ultrafast Demagnetization Measurements Using Extreme Ultraviolet Light: Comparison of Electronic and Magnetic Contributions', *Physical Review X*, vol. 2, no. 1, Jan. 2012.

[109] T. Brückel, 'B 5 Scattering Techniques II: Magnetic X-Ray Scattering', p. 35.

[110] C. Gutt *et al.*, 'Resonant magnetic scattering with soft x-ray pulses from a free-electron laser operating at 1.59 nm', *Physical Review B*, vol. 79, no. 21, Jun. 2009.

[111] C. Gutt *et al.*, 'Single-pulse resonant magnetic scattering using a soft x-ray free-electron laser', *Physical Review B*, vol. 81, no. 10, Mar. 2010.

[112] B. Vodungbo *et al.*, 'Table-top resonant magnetic scattering with extreme ultraviolet light from high-order harmonic generation', *EPL (Europhysics Letters)*, vol. 94, no. 5, p. 54003, Jun. 2011.

List of Figures

List of Tables